Automated inclusion of QED corrections in Monte Carlo event generators

LOIS PHILIPPA FLOWER

Automated inclusion of QED corrections in Monte Carlo event generators

Lois Flower

A Thesis presented for the degree of
Doctor of Philosophy

Institute for Particle Physics Phenomenology
Department of Physics
Durham University
United Kingdom

August 2024

Automated inclusion of QED corrections in Monte Carlo event generators

Lois Flower

Submitted for the degree of Doctor of Philosophy

August 2024

Abstract: In this thesis, we present automated, process-independent methods for the calculation of QED real radiative corrections. We review the construction of a parton shower based on Catani-Seymour dipole subtraction, and thus detail the implementation of a QED parton shower. We validate the predictions made by the shower against the YFS soft-photon resummation, and discuss the algorithmic choices made. We then present results for the production of a Higgs boson at the LHC and its decay to leptons, showing that the interleaved QCD+QED parton shower predicts distributions in excellent agreement with the YFS approach. We then study the MC@NLO method for matching a next-to-leading order calculation with a parton shower. Showing that the method preserves its accuracy for the case of QED corrections and of mixed QCD and QED corrections, we present the QCD+QED MC@NLO method. Validating the method against both the YFS resummation and the QED parton shower, we find very good agreement. Finally, we present an extension to the YFS soft-photon resummation, in which we use a one-step parton shower to resum the logarithms associated with charged particle pair production. Throughout this thesis we also discuss the impact of dressed lepton definitions on observables. The methods presented in this thesis are made available in a public

Monte Carlo event generator and analysis framework.

Contents

List of Figures

List of Abbreviations

Declaration

The work in this thesis is based on research carried out in the Department of Physics at Durham University. No part of this thesis has been submitted elsewhere for any degree or qualification. All original work is my own, carried out in collaboration with my supervisor, Dr Marek Schönherr. Chapters 2 and 3 of this thesis are based on ongoing joint research to be published. Chapter 4 is based on ref. [1].

Acknowledgements

I would like to begin by expressing my deepest gratitude to my supervisor, Marek Schönherr, for all his support throughout my PhD, for endless help with SHERPA, and for putting his trust in me. I am also grateful to everyone in the SHERPA collaboration for being such lovely people to work with and for valuable physics discussions.

A very special thanks go to Elliot Fox, Hitham Hassan, Ery McPartland and Malina Rosca, for proofreading. They, and the whole community at IPPP, were invaluable sources of companionship and support, especially coming out of the Covid-19 pandemic. Of course, the IPPP would not function without Trudy Forster and Joanne Bentham, who helped me with countless admin tasks and made everything run smoothly.

I would like to thank all my housemates over the years I spent in Durham for providing good company and many hours of board games. Thank you to my family for checking in with me often, and for all the practical help and advice. Finally, I would like to thank Joe Callow, for always being there for me.

But if you must and you can, then there's no excuse.

— from *The Amber Spyglass* by Philip Pullman

Chapter 1

Introduction

The Standard Model (SM) of particle physics is a triumph of modern physics, being our most precisely tested theory of nature. Over a huge range of energy and distance scales, we are able to describe the interactions of particles at collider experiments with incredible precision. By utilising a number of mathematical and computational methods, ever more precise predictions can be made. At the time of writing, no discovery of physics beyond the SM has definitively been made, although it is known that it must exist (there is evidence for the existence of dark matter, dark energy and massive neutrinos). More concretely, the recent measurements of the muon anomalous magnetic moment $(g-2)_\mu$ [2, 3] are in conflict with the SM prediction [4]. The uncertainty on the prediction is dominated by the hadronic vacuum polarisation, which can be determined using various experiments, such as low-energy e^+e^- collisions or muon-electron scattering. To confirm the disagreement, and an unquestionable signal of new physics coupling to the SM, or to resolve the tension, we require higher precision predictions of these experiments. For this reason, it is imperative that we continue to improve our understanding of the SM itself.

Modern particle colliders such as the Large Hadron Collider (LHC) and electron-positron 'b factories' are entering a precision era where the experimental error on many measurements is smaller than the theoretical error on the SM prediction. In addition to this success of current experiments, there are multiple proposals for a

future lepton-lepton collider, which would provide the most precise measurements yet of the SM, and any physics beyond the SM. While the success of the engineering involved is to be celebrated, this fact presents a challenge to the theory and phenomenology community. The last 20 years have seen a plethora of new methods for increasing theoretical precision, in many cases in a largely automated and process-independent way.

Many of these automated methods for producing precise theoretical predictions fall under the category of Monte Carlo (MC) statistical methods. They are implemented in MC event generators, codes which simulate the physics involved in particle collisions and produce descriptions of the final-state particles, called events. These events can be treated as similar enough to real collider final states and can be used to model the detector response to certain physics scenarios in experiments. Events can also be analysed to produce cross sections and kinematical distributions, to be compared to data. Due to the public nature of these codes and their vast applicability, MC event generators are a cornerstone of modern particle physics. As a result, their physics models are constantly under development to address the aforementioned challenge to theoretical precision.

In this thesis we concern ourselves with improving the precision of MC event generator predictions by implementing new methods to describe electromagnetic radiative corrections in an automated, process-independent manner. We describe each method and present results to validate the description, before presenting new phenomenological results. In chapter 2 we introduce the quantum electrodynamics (QED) dipole parton shower, in chapter 3 we describe the process of matching the shower to a next-to-leading order (NLO) calculation, and in chapter 4 we introduce the Yennie-Frautschi-Suura (YFS) soft-photon resummation and describe its extension to charged particle pair production. Finally, in chapter 5, we conclude and reflect on the impact of all three methods, and give an outlook on future developments in this area.

1.1 The Standard Model and perturbation theory

The SM of particle physics is an $\mathrm{SU}(3)_C \times \mathrm{SU}(2)_L \times \mathrm{U}(1)_Y$ gauge theory. Quantum chromodynamics (QCD) is a Yang-Mills theory which describes quarks, gluons (the gauge bosons of the strong force) and the hadrons they make up. It exhibits confinement [5] and asymptotic freedom [6, 7]. The former means that objects with a colour charge, notably quarks and gluons, cannot be observed in isolation because the energy required to separate them exceeds the energy required for pair production and the formation of colourless hadrons. The latter allows strong interactions to be calculated using perturbation theory when the energy scale of the interaction is sufficiently high. The strong coupling constant $\alpha_s = g_s^2/4\pi$ has a pole at the confinement scale, $\Lambda_{\mathrm{QCD}} = 210 \pm 14$ MeV in the modified minimal-subtraction ($\overline{\mathrm{MS}}$) scheme with 5 light quark flavours [8]. At energies higher than a few GeV, $\alpha_s < 1$ and therefore perturbation theory can be employed. Below this scale non-perturbative methods, such as lattice QCD, must be used. In practice, however, since lattice QCD is still a developing technology, the solution is usually to use other non-perturbative models with free parameters extracted from data. For initial-state hadrons we make phenomenologically-motivated Ansätze for parton distribution functions (PDFs) and fit these to data. Similarly, to understand the production of final-state hadrons we must model hadronisation. There are various physically-motivated methods to model hadronisation, including the Lund string model [9] and the cluster model [10]. Of the whole SM, only quarks, antiquarks and gluons carry colour charge and hence feel the strong force. However, as the strongest interaction in nature, a huge amount of effort has gone into developing methods to allow us to model QCD ever more precisely.

At high energies, the remaining $\mathrm{SU}(2)_L \times \mathrm{U}(1)_Y$ group describes the electroweak (EW) theory. This symmetry is spontaneously broken in nature, leaving an unbroken $\mathrm{U}(1)_{\mathrm{QED}}$ electromagnetic (EM) symmetry and massive weak gauge bosons, as well

as a massive Higgs boson. The low-energy EM force is described by QED. The gauge boson of QED is the photon, which has no electromagnetic charge (contrary to gluons which carry colour charge). All charged particles feel the EM force: quarks, the charged leptons e, μ and τ, and the charged gauge bosons $W^{\pm}$. The EM force decreases with distance and hence increases with the energy of the interaction, unlike the strong force. The electroweak coupling constant $\alpha = e^2/4\pi$, also known as the fine structure constant, is of order 10^{-2} and has a slow running, so the theory remains perturbative over the whole range of energies available in experiments. The weak sector contains the massive Z and W gauge bosons and the Higgs boson. Due to the high energies required to produce these bosons on-shell, when discussing their production and decay we will usually refer to the unified electroweak interaction instead of the low-energy weak and EM interactions.

In this thesis we will be primarily concerned with the QED sector of the SM, as well as its interplay with QCD. We will propose, motivate and present results for methods to bridge the gap between perturbative calculations and experimental observations. As far as possible, these methods will be process-independent, automated and publicly available.

1.1.1 Perturbation theory, renormalisation and cancellation of infrared singularities

The primary technique of quantum field theory calculations is perturbation theory, in which any interactions are assumed to be a small correction to the free theory and so a series expansion in the coupling constant can be performed. The first interacting term of this series is referred to as leading order (LO). We define a Feynman diagram without loops as a tree-level diagram. While for many quantities the the LO contribution is tree-level, the two terms are not synonymous. The corresponding matrix element (ME) is often referred to as the Born ME to distinguish it from higher-order corrections. NLO calculations generally include diagrams which involve

loops. The momentum flowing through the loop particles is not determined by momentum conservation so must be integrated over all possible values. Some of these loop integrals are divergent due to the requirement to integrate the magnitude of the loop momentum up to infinity. However, by regularising the integrals, it can be seen that the divergences can be absorbed into redefinitions of Lagrangian parameters and all integrals become ultraviolet (UV) finite.

In general, calculations of terms in the perturbative series up to a given order in powers of the relevant coupling (α or α_s or a mix of the two) are called 'fixed-order'. When ordering a perturbative expansion in a mixture of α and α_s, a rule of thumb for the relative magnitudes of the terms is $\alpha \approx \alpha_s^2$. Care must be taken not to double-count contributions, since an EW correction to a QCD-induced process and a QCD correction to an EW-induced process may be identical.

After renormalisation, higher-order calculations still lead to divergences. The emission of a soft or collinear photon or gluon, or a collinear massless fermion, is associated with a so-called infrared (IR) singularity in the cross section due to the phase space integration. Separately, the NLO correction involving exchange of a virtual (internal) photon or gluon to a tree-level process leads to an IR singularity in the integration over the loop momentum. The solution to both these problems lies in abandoning the attempt to calculate them separately. At NLO in the cross section, we must consider both the interference of the Born ME with the one-loop ME and the real-emission ME squared. With the use of regularisation, it can be seen that the two singularities cancel exactly. This is the Kinoshita-Lee-Nauenberg (KLN) theorem [11, 12].

This cancellation of IR singularities occurs not only for the total cross section, but for a range of observables. We will define such observables, where IR divergences exactly cancel, as infrared-safe (IR-safe). More precisely, an IR-safe observable O satisfies the two conditions

$$\begin{aligned} &O_{n+1}(\dots, p_i, \dots) \xrightarrow{p_i \to 0} O_n(\dots) && \text{soft-safe,} \\ &O_{n+1}(\dots, p_i, p_j, \dots) \xrightarrow{p_i \to C p_j} O_n(\dots, (p_i + p_j), \dots) && \text{collinear-safe,} \end{aligned} \tag{1.1.1}$$

where 'soft' means low-energy, such that the soft limit is the limit of zero energy; if two particles are exactly collinear they have parallel momenta $p_i = Cp_j$ and the collinear limit is that of zero separation angle. Examples of IR-safe observables include transverse momenta and energies of jets or suitably dressed leptons, and geometrical observables such as thrust, but do not include observables such as the total number of photons in the final state.

In this section we have discussed perturbation theory as a tool to obtain fixed-order predictions for IR-safe observables. However, fixed-order calculations are not always sufficient to get a good description of the physical process. There can exist very significant contributions even from large powers of the coupling when these are multiplied by logarithms of very large or very small quantities, such as a ratio of energies or masses. Calculations which are not fixed-order use resummation of leading logarithms to obtain a better approximation of the quantity under consideration. This can be extended to next-to-leading logarithms, and so on in the same way as fixed-order calculations. Where the size of logarithms in the perturbative series is controlled and small, a resummed calculation will not achieve significantly higher precision than a fixed-order one.

1.1.2 The YFS soft-photon resummation

The work of Yennie, Frautschi and Suura [13] describes the removal of the IR singularities of QED to all orders by reordering the perturbative expansion of a scattering or decay ME. This is achieved by separating the IR divergences from the finite remainders, to all orders. The IR divergent terms form a series which can be exponentiated, amounting to a resummation of soft-photon logarithms in the enhanced real and virtual regions. This leaves a perturbative expansion in IR-finite, hard photons (both real emissions and virtual exchanges). The YFS approach considers all charged particles of the theory to be massive, and as a consequence only singularities associated with soft-photon emission are present.

In the YFS description, photons are emitted coherently from the charged multipole through the eikonal radiator function. This is in contrast to parton shower descriptions of photon radiation, which usually consider emission from one specific emitter particle or from a charge dipole. The photons produced by a YFS implementation are also not ordered in any specific kinematical variable, but do have an IR cutoff on their energy - all radiation below this energy is resummed with the virtual corrections. The YFS resummation has the advantage that, when the perturbative expansion is reordered, what remains after all soft-photon singularities are resummed is the complete perturbative expansion. This means that IR-subtracted real-correct MEs can be calculated and combined with the resummation to yield fixed-order-matched results.

The YFS resummation is widely used in MC event generators to describe photon radiation. An implementation of the algorithm was first included in the event generator KKMC [14, 15], and later in HERWIG [16], SHERPA [17, 18], BHLUMI [19], BHWIDE [20], WINHAC/ZINHAC [21], and KORALW/YFSWW [22]. The inclusion of the algorithm in general-purpose event generators allows it to be used in conjunction with QCD parton showers, hadronisation and other non-perturbative effects. However, the YFS resummation is not the only approach to modelling QED radiative corrections. One can also use a collinear resummation approach and supplement this with soft effects. A prominent example of a successful tool for QED final-state radiation which uses a bespoke algorithm for exponentiation of multiple soft-photon emissions is PHOTOS [23–26]. The PHOTOS algorithm is similar to that of YFS, but was developed independently.

1.2 Monte Carlo event generators

The modern workhorses of particle physics are event generators. These programs translate ME calculations into ‘events’, collections of particles with defined momenta, which can be treated almost identically to those seen in experimental detectors.

An event generator usually consists of multiple modules which simulate different effects: parton showers, decays, hadronisation, PDFs, beam structure, and sometimes multiple interactions and the underlying event. Event generators carry out cross section calculations using MC integration techniques. There are many excellent reviews of MC event generators in the literature, for example refs. [27–29].

1.2.1 Factorisation of the cross section

Many of the techniques carried out by event generators rely on the factorisation of the cross section into parts characterised by different energy scales. At high scales, we have the partonic cross section, which can be calculated using perturbation theory. But the long-distance objects which we measure are dependent on low-energy physics. Thus, we must describe how the initial state that enters the hard scattering is produced and how the observed final state emerges from the hard scattering. We assume that the relevant processes involved at these two energy scales factorise. The factorisation Ansatz is [30, 31]

$$\sigma_{AB\to X} = \sum_{a\in A}\sum_{b\in B}\int \mathrm{d}x_a \int \mathrm{d}x_b\, f_a^A(x_a,\mu_F^2) f_b^B(x_b,\mu_F^2) \int \mathrm{d}\Phi_{ab\to X} \frac{\mathrm{d}\hat{\sigma}_{ab}(\Phi_{ab\to X},\mu_F^2)}{\mathrm{d}\Phi_{ab\to X}} \tag{1.2.1}$$

where A, B are the incoming beam particles (hadrons or leptons), a, b are their constituent flavours (quarks, gluons, leptons and/or photons), x_a is the momentum fraction carried by constituent a, and f_a^A is the Parton Distribution Function of constituent a in particle A. Additionally, μ_F^2 is the factorisation scale, with units of energy squared. $\hat{\sigma}_{ab\to X}$ is the partonic cross section for the production of a final state X, calculated using perturbation theory.

Note that the cross section in eq. (1.2.1) is the inclusive cross section: it specifies the cross section for the production of X in any kinematical configuration and accompanied by any number of additional particles. However, the way that MC event generators work is to generate an event according to eq. (1.2.1) containing

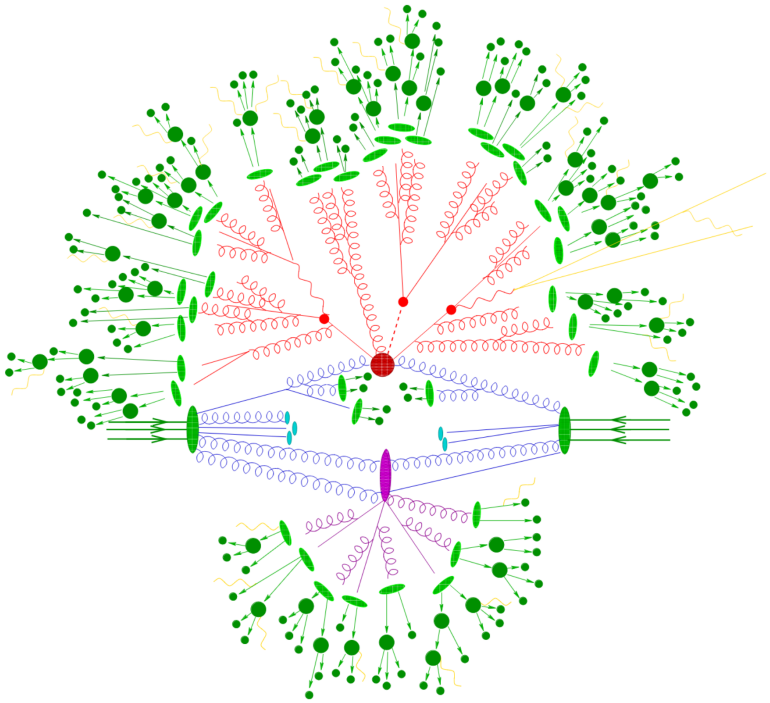

Figure 1.1: A pictorial representation of a $t\bar{t}H$ event at a hadron collider, as represented in the event generator SHERPA [32]. The beams are resolved into partons (blue) which radiate before entering either the hard interaction (red blob) or secondary softer interactions (purple). The heavy final state, the Higgs and top quarks, decay (smaller red blobs) and further QCD radiation is produced by the parton shower (red). Hadronisation is shown in light green and the produced hadrons then decay (dark green). QED radiation is shown in yellow and can occur at all scales.

exactly X as the final state, and then augment this event with additional particles. By using Markov processes to produce these additional particles, probability is conserved, as well as four-momentum, respecting the inclusivity requirement. This is shown schematically in fig. 1.1. For this thesis the relevant Markov process, applicable at hadron and lepton colliders, is the parton shower, which we introduce in section 1.2.2.

1.2.2 The parton shower

The property that a real-emission ME factorises into the Born ME multiplied by a universal splitting function in the collinear limit leads to the derivation of evolution equations for the PDFs, since these must obey the strict collinear limit. The dependence of the PDFs on the factorisation scale is given by the Dokshitser-Gribov-Lipatov-Altarelli-Parisi (DGLAP) equation [33–36],

$$\frac{\mathrm{d}f_a^A(x,\mu_F^2)}{\mathrm{dlog}\,(\mu_F^2)} = \sum_{b\in A}\int_x^1 \frac{\mathrm{d}z}{z}\frac{\alpha}{2\pi}\hat{P}_{b\to a}(z) f_b^A(x/z,\mu_F^2), \tag{1.2.2}$$

where the $\hat{P}_{b\to a}(z)$ are the regularised Altarelli-Parisi splitting functions. These describe the collinear splitting of particle b into particle a in QCD or QED [36]. This leads to an interpretation of the factorisation Ansatz as separating unresolved parton branchings (absorbed into the definition of the PDFs) and resolved parton branchings, which are generated by a parton shower using variants of the Altarelli-Parisi splitting functions. The crossover point between the two is related to the factorisation scale.

Repeatedly generating parton branchings according to eq. (1.2.2) produces new final-state particles in a Markov process which we call initial-state radiation. The final-state radiation will be generated in an analogous manner, without considering the PDFs and instead considering physical cutoff scales for the evolution, such as Λ_{QCD} for QCD radiation or photon resolution scales for QED radiation.

1.2.3 Next-to-leading order calculations and matching

NLO calculations of cross sections generally involve interference terms between loop diagrams (virtual corrections) and the Born ME, and emissions of undetectable particles off external legs (real corrections). IR divergences appear in both cases, when the propagator of a virtual particle goes on-shell or when a real emission becomes infinitely soft or collinear to another particle. In the soft or collinear limit, the particle becomes undetectable. There is no divergence associated with the soft

limit of a fermion, but photons and gluons have this divergence and the collinear limit of any massless emission is associated with a divergence. As described above, to ensure the cancellation of these IR singularities by the KLN theorem, we must consider only IR-safe observables. When the integrals are regularised, for example by moving to $d = 4 - 2\epsilon$ dimensions, the cancellation of singularities is apparent, and the $\epsilon \to 0$ limit can be safely taken. Nevertheless, the need to carry out integrals in d dimensions to facilitate the cancellation prevents numerical integration of NLO quantities.

In order to carry out NLO calculations as described in sec. 1.1 in an event generator, we must ensure that the real and virtual contributions are separately finite. There are two main families of methods to achieve this: phase-space slicing, and subtraction. In this thesis we will exclusively consider subtraction methods. To define an NLO subtraction, we add or remove particles from the Born configuration using a dipole splitting picture. The notation is detailed in sec. 1.3 below; briefly, a tilde is used to denote quantities pre-splitting (in this case, relating to the Born configuration) while unmodified quantities relate to the real-emission configuration. We introduce a notation for mapping from the real-emission phase space Φ_{n+1} to the Born phase space Φ_n [37],

$$b_{ij,k}(\{a\}) = \begin{cases} \{f\} \cup \{f_{\widetilde{ij}}\} \setminus \{f_i, f_j\} \\ \{\vec{p}\} \to \{\vec{\tilde{p}}\}, \end{cases} \tag{1.2.3}$$

where $\{a\} = \{a_1, a_2, \dots a_n\}$ denotes the particle configuration, $\{f\}$ is the set of flavours and $\{\vec{p}\}$ is the set of four-momenta. This mapping removes the emitter particle $\widetilde{ij}$ and adds its splitting products i and j. The inverse is a mapping from the Born phase space to the real-emission phase space,

$$r_{\widetilde{ij},\tilde{k}}(f_j, \Phi^{ij,k}_{R|B}, \{\tilde{a}\}) = \begin{cases} \{\tilde{f}\} \cup \{f_i, f_j\} \setminus \{f_{\widetilde{ij}}\} \\ \{\vec{\tilde{p}}\} \to \{\vec{p}\}, \end{cases} \tag{1.2.4}$$

where $\Phi^{ij,k}_{R|B}$ is the factorised one-particle phase space for an emission $\widetilde{ij}(\tilde{k}) \to ij(k)$, and f_j is the emitted particle flavour. Of course, only those splittings which are

allowed by the theory are considered. In the soft limit, $p_j \to 0$, both these mappings must leave all non-soft particles unchanged. Similarly, in the collinear limit, only the emitter particle may be changed.

These mappings allow us to write down the factorisation of the squared matrix element in the infrared limits. In the collinear limit,

$$|\mathcal{M}_{n+1}|^2(\{a\}) \longrightarrow \frac{8\pi\alpha}{2p_ip_j}\mathcal{M}_n(b_{ij,k}(\{a\})) \otimes \hat{P}_{\widetilde{ij}\to i}(z) \otimes \mathcal{M}_n^*(b_{ij,k}(\{a\})) \tag{1.2.5}$$

where the tensor products indicate spin correlations. In QED, these spin correlations only exist for photon splittings into fermions, which do not have a true collinear singularity in any case. In this thesis we will use spin-averaged splitting functions and reduce this to an ordinary product. In the soft limit, a similar factorisation holds where the Altarelli-Parisi splitting functions divided by the virtuality $2p_ip_j$ are replaced by an eikonal

$$\mathcal{S}_{ij,k} = \frac{p_ip_k}{(p_ip_j)(p_jp_k)} \tag{1.2.6}$$

accompanied by appropriate colour or charge correlators for QCD or QED evolution respectively. These are the ingredients needed to define a subtraction scheme, to allow us to calculate the parts of an NLO calculation individually without encountering divergences.

Here we will use the Catani-Seymour (CS) subtraction method, which is built on dipole factorisation. The subtraction terms include both soft and collinear singularities, obtained by partial fractioning the eikonals [38, 39]. The dipole subtraction terms are denoted by $D^S_{ij,k}$ and their integrals by $I^S_{\widetilde{ij},\tilde{k}}$. Then an observable O has expectation value

$$\begin{aligned}\langle O\rangle^{\mathrm{NLO}} =& \sum_{\{\tilde{f}\}}\int \mathrm{d}\Phi_n\left(\{\tilde{f}\}\right)\left(B\left(\{\tilde{a}\}\right)+\tilde{V}\left(\{\tilde{a}\}\right)+\sum_{\widetilde{ij},\tilde{k}} I^S_{\widetilde{ij},\tilde{k}}\left(\{\tilde{a}\}\right)\right)O\left(\{\tilde{p}\}\right)\\ &+\sum_{\{f\}}\int \mathrm{d}\Phi_{n+1}\left(\{f\}\right)\left(R_{n+1}\left(\{a\}\right)O\left(\{p\}\right)-\sum_{ij,k} D^S_{ij,k}\left(\{a\}\right)O(b_{ij,k}\left(\{p\}\right))\right)\end{aligned} \tag{1.2.7}$$

where $\tilde{V}$, in addition to the one-loop MEs interfered with the Born contribution,

contains the collinear counterterm. It is common to redefine I^S to only cancel the divergences from 1-loop diagrams, and absorb the collinear counterterm and its cancellation into separate K and P terms. This simplifies the evaluation in 4 dimensions and separates the phase space dependence of the terms. R_{n+1} is the real ME squared.

When combining an NLO calculation with a particle-generating Markov process such as a parton shower, care must be taken to avoid double-counting the first emission. Further details will be discussed in chapter 3, but the main difficulty lies in exponentiating only the logarithmically enhanced soft and collinear parts of the subtraction terms. This requires defining suitable starting scale for the parton shower, while treating hard emissions as IR-regular. Many matching methods have been proposed and implemented, including POWHEG [40, 41], MC@NLO [42] and KRKNLO [43].

1.2.4 Summary

The Standard Model of particle physics has been hugely successful in describing a wide range of physics at collider experiments. Modern efforts focus on using perturbation theory and resummation techniques to increase the precision of SM predictions. Monte Carlo event generators are one aspect of this effort, implementing automated methods to make precise predictions for many processes and observables. In this thesis, we will detail the implementation of new methods to describe QED radiative corrections in the event generator SHERPA [32].

1.3 Notation

Throughout this thesis we will use notation consistent with the SHERPA parton shower and NLO matching publications, introduced in refs. [44] and [45].

A dipole parton splitting process is denoted $\widetilde{ij}\,(\tilde{k}) \to ij\,(k)$, where $\widetilde{ij}$ is the emitter parton and $\tilde{k}$ is the spectator parton. A tilde denotes quantities before the splitting, as ordered in a parton shower ordering variable, and i and j are the splitting products. The corresponding splitting function is denoted $S_{\mathrm{f}_{\widetilde{ij}}(\tilde{k})\to\mathrm{f}_i\mathrm{f}_j(k)}$, where f_i is the flavour of parton i. Fermions are denoted f in general, or $q = \{u, d, c, s, t, b\}$ for the quarks, $\ell = \{e, \mu, \tau\}$ for the charged leptons and $\nu = \{\nu_e, \nu_\mu, \nu_\tau\}$ for the neutrinos. Neutrinos are considered massless throughout this thesis. Scalars are denoted s and photons are denoted γ. Momenta, masses and other quantities in splitting processes are labelled with the splitting index.

For NLO calculations, the LO contribution to the squared ME is denoted B, such that the total cross section $\sigma = \int \mathrm{d}\Phi\, B$, where Φ is the Lorentz-invariant phase space. Similarly, the real correction is represented by R and the virtual by V.

The strong coupling constant α_s is always considered to run with the scale, usually denoted by its argument. The EW coupling constant α depends on the input scheme used in the calculation. Unless otherwise specified, for ME calculations we use a fixed α in the G_μ scheme.

Chapter 2

QED parton showers

2.1 Introduction to parton showers

One of the standard tools, almost the defining feature, of any MC event generator is a QCD parton shower. Early parton showers were developed in the 1980s due to the need to describe the large number of final-state particles produced in the newer, higher-energy particle colliders. The process of hadronisation depends on the quantum properties of the hadronising parton ensemble, necessitating a modelling of the whole partonic final state up to timescales comparable to hadronisation. A parton shower provides this by modelling the perturbative splitting of quarks and gluons over a wide range of energy scales using a Markov process. By solving variants of the DGLAP equations for parton splittings of the initial and final states of a hard process, the evolution between the hard scattering partons and the long-distance states is bridged probabilistically. The first parton showers were built on the leading-logarithmic (LL) collinear approximation of QCD MEs for the decay of off-shell partons, ordered in the virtuality of the partons [46–49]. Initially, there was no description of momentum conservation in the shower since the process of hadronisation involved a smooth momentum convolution into the momenta of hadrons. In addition to collinear logarithms, soft logarithms were first resummed in a parton shower in the work of Marchesini and Webber [50, 51]. This work also introduced angular

ordering, ensuring the inclusion of colour coherence effects. This was developed into a full-fledged parton shower in the event generator HERWIG [52]. For the case of the initial state, an important development in QCD parton showers was the advent of backward evolution [53]. This led to the interleaved initial- and final-state QCD shower in many modern showers, pioneered by PYTHIA [54]. While early work on parton showers was intended to replace the use of higher-order MEs, it became clear that even at high-energy colliders, the soft- and collinearly-approximated parton shower was not sufficient to describe the hard wide-angle radiation. Thus a method to merge LO multileg MEs with the parton shower was developed [55, 56], which became the cornerstone of the event generator SHERPA [57].

Despite the flourishing development of QCD parton showers over the last 40 years, the need for precise description of QED radiation has been much less pronounced and so QED showers are not ubiquitous in event generators. PHOTOS [23–26] was the first process-independent tool developed for modelling QED final-state radiation. HERWIG has a QED parton shower which includes all spin correlation effects [58]. PYTHIA also includes a QED shower which treats each $f\bar{f}$ pair as an independent dipole, thus approximating the correct multipole soft limit for photon emissions. The parton shower in SHERPA has also been previously updated to include QED splittings in order to model hard photon production [59]. However, until this work, only positive dipoles have been included, leading to an overestimate of the photon radiation produced in the soft limit. In addition, photon splittings into fermions were previously not modelled correctly in the dipole picture. This has little effect on observables where a hard photon is selected, but can have non-negligible effects on reconstructed resonances, especially when dressed leptons are used to reconstruct them. In this chapter, we will detail the modifications made to the QED parton shower in SHERPA.

We begin by outlining the ingredients behind a parton shower algorithm. We follow the description given in ref. [27], which, like the QED parton shower we will outline here, is built on the CS dipole subtraction.

First, we motivate an initial-state parton shower as the ability to model initial-state radiation, not inclusively via PDFs, but exclusively such that actual particles are produced. Since any parton shower must have an IR cutoff, however, the DGLAP equations must be modified for initial-state radiation. The parton shower IR cutoff means that the plus-prescription and δ-function part are no longer needed. This would amount to including real-emission corrections to the cross section in the LL approximation. This is the approach taken in many QED parton showers for e^+e^- colliders, for example in the event generator BabaYaga [60–64]. For the case of parton showers at hadron colliders, however, the approach taken is to respect unitarity of the LO cross section. This results in a probabilistic interpretation of the splitting functions, at least in the leading-colour limit of a QCD parton shower. To achieve unitarity, an extra term is added to the DGLAP equations (eq. (1.2.2)) to represent the virtual corrections in the restricted phase space,

$$\begin{aligned}\frac{\mathrm{d}f_a^A(x,t)}{\mathrm{d}\log t} =& \sum_{b\in A}\int_x^{z_{\max}}\frac{\mathrm{d}z}{z}\frac{\alpha}{2\pi}P_{b\to a}(z)f_b^A(x/z,t)\\ &- f_a^A(x,t)\sum_{b\in A}\int_{z_{\min}}^{z_{\max}}\mathrm{d}z\frac{\alpha}{2\pi}\frac{1}{2}P_{a\to b}(z),\end{aligned} \tag{2.1.1}$$

where the second term represents the probability for removing a particle of flavour a through its splitting to other flavours. The factor $1/2$ is due to the symmetry in the splitting variable z and its complement $1-z$. In this equation, we have also written t instead of the factorisation scale μ_F^2. This is the parton shower evolution variable, which will be defined later.

A final-state parton shower, or more generally one which can model initial-final interference as well as radiation from the initial and final states, does not need to replicate PDF evolution, but is built from the same collinear factorisation picture which will be detailed in the next section.

In chapter 1, we introduced a mapping from a Born particle configuration to that of a real-emission event, eq. (1.2.4). This mapping is not uniquely defined for each splitter-spectator pair, unlike its inverse. It depends not only on the three kinematical

variables needed to describe the momentum of the newly created particle, but also on its flavour (although the latter is often fixed by the Born particle configuration). The parton shower uses the MC methods described in this section to select these variables while respecting the underlying evolution equations.

Key to the parton shower algorithm is the 'hit and miss' provided by the veto algorithm described below. The process begins at some scale t' where all the possible splitter partons are iterated over, then all the possible spectators. An overestimate for the splitting is calculated and a new scale t is computed. The new scale is then accepted with a probability which corrects for the overestimate. If the splitting is accepted, the new particle is created and flavours, colours and kinematics are updated. The whole process is repeated at the new lower scale until some IR cutoff t_c, needed to regulate the divergence of the splitting functions. This cutoff is usually taken around the hadronisation scale for QCD showers, since quarks and gluons would no longer be meaningful degrees of freedom below this scale. For QED evolution, a natural cutoff for photon splittings is provided by the mass of the produced fermions, and for photon emissions the cutoff should be chosen low enough to not affect the observables of interest.

In this chapter, we describe the construction of a QED parton shower, starting from the CS dipole subtraction scheme for NLO electroweak corrections. In the construction we take inspiration from QCD parton showers based on CS subtraction. In section 2.2.3 we show that the veto algorithm reproduces the desired integral of the probability distribution. We present results from the updated QED shower in SHERPA in section 2.4. Before concluding and providing an outlook in section 2.6, we detail the additional considerations required in the case of initial-state radiation at an e^+e^- collider in section 2.5.

2.2 Construction of a QED parton shower

As motivated in section 1.2.2, parton showers based on CS dipole subtraction have been highly successful phenomenological tools for QCD. In this section we describe the construction of a QED parton shower from the CS dipole subtraction terms.

Eq. (1.2.7) for the expectation value of an IR-safe observable at NLO in the CS dipole subtraction formalism is repeated here for convenience,

$$\begin{aligned}\langle O\rangle^{\mathrm{NLO}} =& \sum_{\{\tilde{f}\}} \int \mathrm{d}\Phi_n\left(\{\tilde{f}\}\right)\left(B\left(\{\tilde{a}\}\right)+\tilde{V}\left(\{\tilde{a}\}\right)+\sum_{\widetilde{ij},\tilde{k}} I^S_{\widetilde{ij},\tilde{k}}\left(\{\tilde{a}\}\right)\right) O\left(\{\tilde{p}\}\right) \\ &+\sum_{\{f\}}\int \mathrm{d}\Phi_{n+1}\left(\{p\}\right)\left(R_{n+1}\left(\{a\}\right)O\left(\{p\}\right)-\sum_{ij,k} D^S_{ij,k}\left(\{a\}\right)O(b_{ij,k}\left(\{p\}\right))\right).\end{aligned}$$

To construct a parton shower from the subtraction terms $D^S_{ij,k}$, we start from the factorisation of the $(n+1)$-particle phase space in the IR limit,

$$\mathrm{d}\Phi_{n+1}\, D^S_{ij,k}(\{a\}) \xrightarrow{\text{soft or collinear}} \mathrm{d}\Phi_n\left[\sum_{\widetilde{ij},\tilde{k}\in\{f\}}\sum_{f_j}\mathrm{d}\Phi_1^{ij,k} D^S_{ij,k}(r_{\widetilde{ij},\tilde{k}}\{\tilde{a}\})\right], \tag{2.2.1}$$

where $\{a\},\{\tilde{a}\}$ are particle configurations, and $r_{\widetilde{ij},\tilde{k}}$ is the momentum mapping, eq. (1.2.4). In a parton shower, our goal is to generate the one-particle phase space $\mathrm{d}\Phi_1^{ij,k}$. We parametrise it in three variables t, z and the azimuthal angle ϕ,

$$\mathrm{d}\Phi_1^{ij,k} = \frac{1}{16\pi^2}\,\mathrm{d}t\,\mathrm{d}z\frac{\mathrm{d}\phi}{2\pi}J(t,z,\phi), \tag{2.2.2}$$

where $J(t,z,\phi)$ is the Jacobian. Now we also use factorisation of the soft and collinear limits of particle radiation, and factorise out the Born differential cross section $\mathrm{d}\sigma_B$ from the radiative part,

$$\mathrm{d}\sigma = \mathrm{d}\sigma_B \sum_{\widetilde{ij},\tilde{k}\in\{f\}}\sum_{f_i}\frac{\mathcal{L}(r_{\widetilde{ij},\tilde{k}}(\{a\}))}{\mathcal{L}(\{\tilde{a}\})}\,\frac{D^S_{ij,k}(r_{\widetilde{ij},\tilde{k}}(\{a\}))}{B(\{\tilde{a}\})}, \tag{2.2.3}$$

where we have also included the particle luminosity factors $\mathcal{L}$, since this is a differential cross section. The particle luminosity is given by

$$\mathcal{L}(\{a\},\mu_F^2) = x_1 f^A_{f_1}(x_1,\mu_F^2)\, x_2 f^B_{f_2}(x_2,\mu_F^2), \tag{2.2.4}$$

where x_i is the momentum fraction of f_i in A or B, as appropriate. For final-state radiation, since the initial-state flavours and momenta do not change, the ratio of particle luminosities is 1. This is the essence of our parton shower factorisation. We will give the explicit forms of the splitting functions $D^S_{ij,k}$ below. However, as mentioned above, applying this without modification would violate unitarity, neither resulting in the correct LO cross section nor the correct NLO one. Near the IR limit, the logarithmic terms are dominant, and these exactly cancel between the virtual corrections and real-emission contributions due to the KLN theorem. We assume, in our LO-accurate parton shower, that virtual corrections exactly cancel the finite (non-logarithmic) parts of the real corrections. This leads to the addition of an unresolved-emission term

$$\Omega^{\widetilde{ij},\tilde{k}}(t,t') = \exp\left(-\frac{1}{16\pi^2}\sum_{f_i}\int_t^{t'}\mathrm{d}t\int\mathrm{d}z\int\frac{\mathrm{d}\phi}{2\pi}\,\frac{1}{2}\,\frac{\mathcal{L}(r_{\widetilde{ij},\tilde{k}}(\{a\}))}{\mathcal{L}(\{\tilde{a}\})}\,\frac{D^S_{ij,k}(r_{\widetilde{ij},\tilde{k}}(\{a\}))}{B(\{\tilde{a}\})}\right). \tag{2.2.5}$$

The product $\Omega(t,t') = \prod_{\{\widetilde{ij},\tilde{k}\}}\Omega^{\widetilde{ij},\tilde{k}}(t,t')$ gives the total no-emission probability of the parton shower, which is clearly seen by extending the sum over emitter-spectator pairs into the exponential. Since $\Omega(t,t')$ is a Poisson distribution in $\log t$, the probability of a branching at a scale t, starting from scale t', is given by

$$\mathcal{P}(t,t') = \frac{\mathrm{d}\Omega(t,t')}{\mathrm{d}\log t}. \tag{2.2.6}$$

In a final-state parton shower, the no-emission probability $\Omega = \Delta$, the Sudakov form factor, which is defined to solve the DGLAP equations. However, where initial-state particles are involved, Ω also contains a ratio of particle luminosities. A parton shower uses our knowledge of the form of $\mathcal{P}(t,t')$ using QCD or QED splitting functions to solve eq. (2.2.6) for t, the splitting scale.

The forms of the emission and no-emission probabilities will inform our construction of the parton shower algorithm in section 2.2.3 below. First, however, we will give specific expressions for the parton shower splitting functions. The subtraction terms $D^S_{ij,k}$ have different forms depending on whether $\widetilde{ij}$ and $\tilde{k}$ are in the initial or final

state.

2.2.1 Splitting functions

Final-final For a final-state splitter $\widetilde{ij}$ and a final-state spectator $\tilde{k}$,

$$D^S_{ij,k} = -\frac{1}{(p_i+p_j)^2 - m^2_{\widetilde{ij}}}\,\mathbf{Q}^2_{\widetilde{ij}\tilde{k}}\,\langle \ldots, \widetilde{ij}, \ldots, \tilde{k}, \ldots |\mathbf{V}_{ij,k}| \ldots, \widetilde{ij}, \ldots, \tilde{k}, \ldots \rangle, \quad (2.2.7)$$

where $|\ldots, \widetilde{ij}, \ldots, \tilde{k}, \ldots\rangle$ is a vector in colour and helicity space, and thus the product indicates a squared matrix element, summed over final-state colours and spins.

The charge correlator is defined as [13, 65–68]

$$\mathbf{Q}^2_{\widetilde{ij}\tilde{k}} = \begin{cases} \frac{Q_{\widetilde{ij}}\theta_{\widetilde{ij}} Q_{\tilde{k}}\theta_{\tilde{k}}}{Q^2_{\widetilde{ij}}}, & \text{for } \widetilde{ij} \neq \gamma \\ \kappa_{\widetilde{ij}\tilde{k}}, & \text{for } \widetilde{ij} = \gamma, \end{cases} \quad (2.2.8)$$

where the Q are the charges of the particles and $\theta = 1\,(-1)$ if the particle is in the final (initial) state. Clearly $Q_{\tilde{k}} = Q_k$, since the spectator does not change flavour, and $\theta_{\tilde{k}} = \theta_k$. The $\kappa_{\widetilde{ij}\tilde{k}}$ are parameters that can be chosen to implement a spectator-assigning scheme but are subject to the constraint

$$\sum_{\tilde{k}\neq\widetilde{ij}} \kappa_{\widetilde{ij}\tilde{k}} = -1 \quad \forall \widetilde{ij} = \gamma, \quad (2.2.9)$$

in order that the sum over all possible spectators adds up to the correct collinear limit. There are various schemes for assigning spectators to photon splittings, discussed further in chapter 4 and in ref. [69].

The parton shower splitting functions are the spin-averaged forms of $\mathbf{V}_{ij,k}$, in 4 dimensions, divided by the Born contribution,

$$S_{\widetilde{ij}(\tilde{k})\to ij(k)} = \frac{\langle s|\mathbf{V}_{ij,k}|s\rangle|_{\epsilon=0}}{B}, \quad (2.2.10)$$

in terms of the splitting variable $y_{ij,k}$ and light-cone momentum fraction z_i, which

are defined as

$$y_{ij,k} = \frac{p_i p_j}{p_i p_j + p_i p_k + p_j p_k} \qquad \text{and} \qquad z_i = \frac{p_i p_k}{p_i p_k + p_j p_k} \,. \tag{2.2.11}$$

We will usually suppress the splitting indices and write y to mean $y_{ij,k}$ and z instead of z_i. From the definition of z_i it is clear that $z_j = 1 - z_i$, and so under $i \leftrightarrow j$, each splitting function is given by the exchange $z \leftrightarrow 1 - z$.

Then the splitting functions are

$$\begin{aligned} S_{f_{\widetilde{ij}}(\tilde{k}) \to f_i \gamma_j(k)} \;=\; S_{\bar{f}_{\widetilde{ij}}(\tilde{k}) \to \bar{f}_i \gamma_j(k)} &= 8\pi\,\alpha \left[\frac{2}{1 - z + zy} - \frac{\tilde{v}_{\widetilde{ij},\tilde{k}}}{v_{ij,k}} \left(1 + z + \frac{m_i^2}{p_i p_j} \right) \right] \\ S_{\gamma_{\widetilde{ij}}(\tilde{k}) \to f_i \bar{f}_j(k)} &= 8\pi\,\alpha \left[1 - 2z(1-z) - z_+ z_- \right] . \end{aligned} \tag{2.2.12}$$

The relative velocities $v, \tilde{v}$ are introduced to facilitate the analytic integration for the case of massive partons. $z_\pm$ are the phase space boundaries. Explicit expressions for these are given in the SHERPA parton shower literature, e.g. ref. [44]. In chapter 4 we use different solutions for the relative velocities and phase space boundaries, which are detailed there.

Final-initial For a final-state splitter $\widetilde{ij}$ and a massless initial-state spectator $\tilde{a}$,[1]

$$D^S_{aj,k} = -\frac{1}{(p_i + p_j)^2 - m^2_{\widetilde{ij}}} \frac{1}{y_{ij,a}} \mathbf{Q}^2_{\widetilde{ij}\tilde{a}} \left\langle \dots, \widetilde{ij}, \dots, \tilde{a}, \dots \middle| \mathbf{V}_{ij,a} \middle| \dots, \widetilde{ij}, \dots, \tilde{a}, \dots \right\rangle, \tag{2.2.13}$$

where $y_{ij,a}$ is the splitting variable defined below in eq. (2.2.14).

The splitting variables are

$$y_{ij,a} = 1 - \frac{p_i p_j - \frac{1}{2}\left(m^2_{\widetilde{ij}} - m_i^2 - m_j^2 \right)}{p_i p_a + p_j p_a} \qquad \text{and} \qquad z_i = \frac{p_i p_a}{p_i p_a + p_j p_a} \,. \tag{2.2.14}$$

The initial-state splitting variable is often called $x_{ij,a}$, but we will retain the label $y_{ij,a} = y$, to distinguish it from the momentum fraction x of the beam which is carried by a given parton.

[1] The splitting functions for the case of a massive spectator are given in sec. 4.4.

Then, analogously to the final-final case,

$$\begin{aligned} S_{f_{\widetilde{ij}}(\tilde{a})\to f_i\gamma_j(a)} &= S_{\bar{f}_{\widetilde{ij}}(\tilde{a})\to \bar{f}_i\gamma_j(a)} = 8\pi\,\alpha\,\left[\frac{2}{2-z-y}-(1+z)-\frac{m_i^2}{p_ip_j}\right] \\ S_{\gamma_{\widetilde{ij}}(\tilde{a})\to f_i\bar{f}_j(a)} &= 8\pi\,\alpha\,\left[1-2(z_+ + z)(z_- - z)\right]. \end{aligned} \tag{2.2.15}$$

Initial-final For a massless initial-state splitter $\widetilde{aj}$ and a final-state spectator $\tilde{k}$,

$$D^S_{aj,k} = -\frac{1}{2p_ap_j}\,\frac{1}{z_{aj,k}}\,\mathbf{Q}^2_{\widetilde{aj}\tilde{k}}\,\langle\ldots,\widetilde{aj},\ldots,\tilde{k},\ldots|\mathbf{V}_{aj,k}|\ldots,\widetilde{aj},\ldots,\tilde{k},\ldots\rangle, \tag{2.2.16}$$

where the splitting variables are defined by

$$z_{aj,k} = 1-\frac{p_jp_k}{p_jp_a+p_kp_a} \qquad \text{and} \qquad u_i = \frac{p_ip_a}{p_ip_a+p_kp_a}\,. \tag{2.2.17}$$

Then the splitting functions are given by

$$\begin{aligned} S_{f_{\widetilde{aj}}(\tilde{k})\to f_a\gamma_j(k)} &= S_{\bar{f}_{\widetilde{aj}}(\tilde{k})\to \bar{f}_a\gamma_j(k)} = 8\pi\,\alpha\,\left[\frac{2}{2-u-z}-(1+u)\right] \\ S_{\gamma_{\widetilde{aj}}(\tilde{k})\to f_a\bar{f}_j(k)} &= 8\pi\,\alpha\,\left[1-2z(1-z)\right]. \end{aligned} \tag{2.2.18}$$

Initial-initial For a massless initial-state splitter $\widetilde{aj}$ and a massless spectator $\tilde{b}$,

$$D^S_{aj,b} = -\frac{1}{2p_ap_j}\,\frac{1}{z_{aj,b}}\,\mathbf{Q}^2_{\widetilde{aj}\tilde{b}}\langle\ldots,\widetilde{aj},\ldots,\tilde{b},\ldots|\mathbf{V}_{aj,b}|\ldots,\widetilde{aj},\ldots,\tilde{b},\ldots\rangle, \tag{2.2.19}$$

where the splitting variable $z_{aj,b}$ is now given by

$$z_{aj,b} = 1-\frac{p_jp_a+p_jp_b}{p_ap_b}\,. \tag{2.2.20}$$

Then, as before, the splitting functions are

$$\begin{aligned} S_{f_{\widetilde{ij}}(\tilde{a})\to f_i\gamma_j(a)} &= S_{\bar{f}_{\widetilde{ij}}(\tilde{a})\to \bar{f}_i\gamma_j(a)} = 8\pi\,\alpha\,\left[\frac{2}{2-z}-(1+z)\right] \\ S_{\gamma_{\widetilde{ij}}(\tilde{a})\to f_i\bar{f}_j(a)} &= 8\pi\,\alpha\,\left[1-2z(1-z)\right]. \end{aligned} \tag{2.2.21}$$

Only one splitting variable is needed to specify the splitting functions in this case, but for the full kinematics a second variable $v_i = p_ip_a/p_ap_b$ must be defined [44].

These splitting functions, for the four dipole cases discussed, reproduce both the soft eikonal limit and, when massless fermions are involved, the collinear Altarelli-Parisi limit [38].

2.2.2 The dipole picture and QED

Most QCD parton showers are built on the large-N_C limit, or the leading-colour approximation. This is justified by the fact that the next-to-leading term in the expansion in N_C goes as $1/N_C^2$, which for $N_C = 3$ is approximately a 10% correction on what is already formally a 10% effect, since $\alpha_s \approx 0.1$. Many newer showers go beyond this limit and include subleading colour effects [70–73]. However, in QED, there is no leading-colour approximation since $N_C = 1$. This reflects the fact that photon emission is properly described by coherent radiation from a whole charged multipole, rather than individual dipole terms. A parton shower can still be built using a dipole picture, however, but all charge dipoles must be included. This necessarily includes either same-charge dipoles or opposite-charge initial-final interference, which in both cases will give a negative contribution as seen from the charge correlator defined in eq. (2.2.8).

Now we will show how a 'hit and miss' algorithm, ordered in a suitable ordering parameter defined later, reproduces the correct distribution of radiation according to the splitting functions defined above. Hence, by iterating these splittings, we resum the leading soft and collinear logarithms by exponentiating them into a Sudakov factor. The problem of negative splitting functions will be solved by an analytic weighting method.

2.2.3 The veto algorithm

The veto algorithm [74, 75] is a method for generating a parton splitting at a scale t (the parton shower evolution variable) according to a probability distribution $f(t)$ when the integral of the distribution, $F(t)$ is unknown. To simplify the notation, the

presence of only one splitting function is assumed here but the extension to multiple functions, including flavour changing splittings, is straightforward. This description is based on many excellent arguments in the literature, for example refs. [54, 76, 77].

The differential probability for generating an emission at scale t, starting from an upper scale t', is given by eq. (2.2.6), i.e.

$$\mathcal{P}(t,t') = f(t)\exp\left(-\int_t^{t'} \mathrm{d}\tilde{t}\, f(\tilde{t})\right), \tag{2.2.22}$$

and the new scale is generated according to the distribution of $f(t)$:

$$t = F^{-1}(F(t') + \log r), \tag{2.2.23}$$

where r is a random number between zero and one, $F(t)$ is the indefinite integral of $f(t)$, and $F^{-1}(x)$ is the inverse of $F(t)$.

If $F(t)$ is unknown, an overestimate $g(t) \geq f(t)$ is defined, where the integral $G(t)$ of the overestimate is known. Then we generate the new scale instead using the integral of the overestimate $G(t)$,

$$t = G^{-1}(G(t') + \log r), \tag{2.2.24}$$

and the new scale (and splitting) is accepted with probability $f(t)/g(t)$. Then the probability of a splitting being accepted, with n intermediate rejections, is

$$\begin{aligned}\mathcal{P}_n(t,t') = \frac{f(t)}{g(t)}\, g(t)\exp\left(-\int_t^{t_1} \mathrm{d}\tilde{t}\, g(\tilde{t})\right) \\ \times \prod_{i=1}^{n}\left[\int_{t_{i-1}}^{t_{n+1}} \mathrm{d}t_i \left(1 - \frac{f(t_i)}{g(t_i)}\right) g(t_i)\, \exp\left(-\int_{t_i}^{t_{i+1}} \mathrm{d}\tilde{t}\, g(\tilde{t})\right)\right],\end{aligned} \tag{2.2.25}$$

where $t_0 = t$ and $t_{n+1} = t'$. Note that $n = 0$ is allowed here: in that case $t_1 = t'$ and the second line of eq. (2.2.25) gives a factor of unity.

To reproduce eq. (2.2.22), we use that

$$\mathcal{P}(t,t') = \sum_{n=0}^{\infty} \mathcal{P}_n(t,t'), \tag{2.2.26}$$

i.e. we cannot distinguish the number of rejections which occur before a splitting.

Note that the product in eq. (2.2.25) can be simplified using properties of exponentials and integrals,

$$\prod_{i=1}^{n} \exp\left(-\int_{t_i}^{t_{i+1}} \mathrm{d}\tilde{t}\, g(\tilde{t})\right) = \exp\left(-\sum_{i=1}^{n}\int_{t_i}^{t_{i+1}} \mathrm{d}\tilde{t}\, g(\tilde{t})\right) = \exp\left(-\int_{t_1}^{t_{n+1}} \mathrm{d}\tilde{t}\, g(\tilde{t})\right). \tag{2.2.27}$$

When summing over all n, using symmetry under $t_i \leftrightarrow t_j$, we also recognise the infinite series

$$\sum_{n=0}^{\infty}\prod_{i=1}^{n}\int_{t_{i-1}}^{t_{n+1}} \mathrm{d}t_i \left(1-\frac{f(t_i)}{g(t_i)}\right) g(t_i) = \sum_{n=0}^{\infty}\frac{1}{n!}\left[\int_{t_0}^{t_{n+1}} \mathrm{d}\tilde{t}\left(1-\frac{f(\tilde{t})}{g(\tilde{t})}\right) g(\tilde{t})\right]^n = \exp\left(\int_{t}^{t'} \mathrm{d}\tilde{t}\left(1-\frac{f(\tilde{t})}{g(\tilde{t})}\right)\right). \tag{2.2.28}$$

Therefore, eq. (2.2.22) follows immediately upon summation of eq. (2.2.25) over all numbers of rejections n.

In equation (2.2.22), the term

$$\Delta(t,t') = \exp\left(-\int_{t}^{t'} \mathrm{d}\tilde{t} f(\tilde{t})\right), \tag{2.2.29}$$

which resums an infinite series, is defined as the Sudakov form factor and interpreted as the probability for no branching to occur between the two scales t' and t. In the case of an NLO-matched parton shower, it will acquire additional meaning as the exponential of the IR subtraction terms at NLO.

When we apply a lower cutoff t_c to the algorithm, we will encounter events which do not generate a splitting with $t > t_c$. In those cases, we no longer generate eq. (2.2.22), but only the exponential term, as expected. These events are rare in a QCD parton shower, but much more common in a QED parton shower due to the smallness of α.

We have shown that the veto algorithm correctly produces the probability distribution for one or zero emissions to occur, after any number of rejected splittings. To extend the argument to a complete parton shower, therefore, we must consider the fact that all evolution is strictly ordered in the variable t. Since $g(t) \geq f(t)$, and

therefore the no-emission probability according to $g(t)$ is smaller than that from $f(t)$, once we have generated no emissions in a t region, it is not necessary to revisit this region. In this way, nested integrals from subsequent emissions decouple, and the full parton shower evolution can be generated by repeated application of the veto algorithm in descending t.

The weighted veto algorithm

When describing QED radiation in a dipole picture, we must be mindful that unlike in QCD, there is no leading-colour limit. Thus, all dipoles must be included, some of which have negative splitting functions due to the product of splitter and spectator charges. This would destroy the probabilistic interpretation of the splitting functions. To restore this, we can introduce an additional overestimate, $h(t)$. We sample using the positive-definite $h(t)$, veto with probability $0 \leq f(t)/g(t) \leq 1$, and then apply the additional weight $g(t)/h(t)$ analytically.

Using this method, the modified probability of a splitting being accepted after n rejections is

$$\mathcal{P}_n(t,t') = \frac{f(t)}{g(t)}\, h(t) \exp\left(-\int_t^{t_1} \mathrm{d}\tilde{t}\, h(\tilde{t})\right) \times \prod_{i=1}^{n} \left[\int_{t_{i-1}}^{t_{n+1}} \mathrm{d}t_i \left(1 - \frac{f(t_i)}{g(t_i)}\right) h(t_i) \exp\left(-\int_{t_i}^{t_{i+1}} \mathrm{d}\tilde{t}\, h(\tilde{t})\right)\right], \quad (2.2.30)$$

and the correct distribution $\mathcal{P}(t,t')$ is reproduced after applying the weight

$$w_n(t,t_1,...,t_n) = \frac{g(t)}{h(t)} \prod_{i=1}^{n} \frac{g(t_i)}{h(t_i)} \frac{h(t_i) - f(t_i)}{g(t_i) - f(t_i)}, \quad (2.2.31)$$

and summing over n from 0 to infinity. To see that this is the correct weight, we follow the same procedure as in equations 2.2.25-2.2.28 to find that the weighted probability of acceptance after n rejections becomes

$$w_n \mathcal{P}_n(t,t') = f(t) \prod_{i=1}^{n} \left[\int_{t_{i-1}}^{t_{n+1}} \mathrm{d}t_i \left(1 - \frac{f(t_i)}{g(t_i)}\right) h(t_i) \frac{g(t_i)}{h(t_i)} \frac{h(t_i) - f(t_i)}{g(t_i) - f(t_i)}\right] \times \exp\left(-\int_{t_0}^{t_{n+1}} \mathrm{d}\tilde{t}\, h(\tilde{t})\right). \quad (2.2.32)$$

Simplifying and summing over all n,

$$\begin{aligned} w\mathcal{P}(t,t') &= \sum_{n=0}^{\infty}\left\{f(t)\frac{1}{n!}\left[\int_{t_0}^{t_{n+1}}\mathrm{d}\tilde{t}(h(\tilde{t})-f(\tilde{t}))\right]^n \exp\left(-\int_{t_0}^{t_{n+1}}\mathrm{d}\tilde{t}\,h(\tilde{t})\right)\right\} \\ &= f(t)\exp\left(-\int_t^{t'}\mathrm{d}\tilde{t}\,h(\tilde{t})\right)\exp\left(\int_t^{t'}\mathrm{d}\tilde{t}\,(h(\tilde{t})-f(\tilde{t}))\right) \\ &= f(t)\exp\left(-\int_t^{t'}\mathrm{d}\tilde{t}\,f(\tilde{t})\right), \end{aligned} \tag{2.2.33}$$

which reproduces eq. (2.2.22). This works for all choices of $h(t)$, and the primary reason for its use in this thesis is to correctly model photon emission from same-sign dipoles. In this case, when there are negative QED splitting functions, we let $h(t) = -g(t)$. The weighted veto algorithm can also be used to probe statistically unlikely regions with better precision. For example, with a weight $h(t) = 10g(t)$, the emission of a photon from a quark could be considered roughly as often as the emission of a gluon. This is extremely useful in an interleaved shower when studying observables which depend on QED radiation.

2.2.4 The generating functional of the parton shower

We will now put all the ingredients together and express the full parton shower evolution as a generating functional. This will allow us to write down the effect of the parton shower on a general IR-safe observable. We will also refer to this formalism when we discuss matching in chapter 3.

The generating functional is recursively defined in terms of the splitting functions $D^{ij,k}$ as

$$\begin{aligned} \mathcal{F}_n(\Phi_n, O) = &\underbrace{\Delta(\mu_Q^2, t_c)\, O(\Phi_n)}_{\text{virtual + unresolved}} \\ &+ \sum_{\{\widetilde{ij},k\}}\sum_f \int \mathrm{d}\Phi_1^{ij,k}\,\Theta(t_{ij,k}-t_c)\,\underbrace{S_{ij,k}\,\Delta(\mu_Q^2,t)\,D^{ij,k}}_{\text{resolved}} \\ &\times \mathcal{F}_{n+1}(\Phi_{n+1}, O), \end{aligned} \tag{2.2.34}$$

where $S_{ij,k}$ is a ratio of symmetry factors, and $\mathcal{F}_{n+1}$ is the result of the parton shower

acting on the new $(n+1)$-particle configuration. Then the expectation value of an observable O is given by

$$\langle O\rangle^{\mathrm{PS}} = \sum_f \int \mathrm{d}\Phi_n \, B \, \mathcal{F}_n(\Phi_n, O), \tag{2.2.35}$$

where B contains the appropriate parton luminosity factors.

2.2.5 Kinematics

To obtain the kinematics of the individual splittings, we invert the phase space factorisation which emerges from the subtraction scheme. For details, see ref. [44]. It is important to note that initial-state spectators cannot absorb any transverse recoil, so the whole final state undergoes a Lorentz transformation. In this way, the initial-state radiation induces logarithmic corrections to the transverse masses of intermediate resonances. This process has been improved with a new recoil scheme, described in ref. [59].

2.2.6 Details of the implementation

There are a few remaining subtleties in implementing an interleaved QCD+QED parton shower, which are detailed below.

Evolution variable. The choice of the evolution variable t is an important factor in defining a parton shower algorithm. Here we follow the default choice made in the QCD dipole shower in SHERPA, namely that final-state fermions emit vectors (gluons and photons) with the modified transverse momentum

$$t = \bar{k}_T^2 = (Q^2 - m_i^2 - m_j^2 - m_k^2)\, y\, (1-z), \tag{2.2.36}$$

and that photon splitting into fermions is described by the modified virtuality

$$t = \tilde{q}^2 = (Q^2 - m_i^2 - m_j^2 - m_k^2)\, y. \tag{2.2.37}$$

This ensures colour and charge coherence, and angular ordering where appropriate. More details are given in section 4.2.2. Different choices of evolution variable are made for initial-state evolution, which are described in the SHERPA user manual.

In addition, the generation of evolution variables can be simplified. Throughout the description of the veto algorithm, sec. 2.2.3, we treated $f(t)$ and $g(t)$ as (in principle) different functions of t, subject only to the constraint $g(t) \geq f(t)$. However, in the case of parton shower splitting functions, the t dependence is typically straightforward. As can be seen in equations (2.2.7)-(2.2.19), the t dependence enters only through the virtuality, and hence all splitting functions $f(t) \propto 1/t$. Therefore $g(t) \propto 1/t$ and $F(t) \propto G(t) \propto \log t$. Using this fact, and defining an overestimate G' of $S_{\widetilde{ij}(\tilde{k})\to ijk}$, eq. (2.2.24) is usually implemented as

$$t = t'\, r^{2\pi/G'}. \tag{2.2.38}$$

Infrared cutoff. For QCD evolution, the quarks and gluons are not physical degrees of freedom at scales below a few GeV due to confinement. For this reason, the IR cutoff of a QCD parton shower is usually around 1-2 GeV. However, photon emission has no such intrinsic cutoff, and photon splittings into electrons are kinematically allowed to occur while the photon has virtuality greater than twice the electron mass. This means that the evolution variable can in principle take values of the order of the electron mass. In QED there is no process like hadronisation to take care of the effects of softer radiation, so to properly model QED radiation we must allow the parton shower to evolve to lower scales. Here we choose a cutoff $t_c = 10^{-6}\,\mathrm{GeV}^2$ for final-state evolution of leptons and photons. For initial-state evolution of leptons, the IR cutoff is coupled with the upper cutoff on the PDF or structure function momentum fraction, so the discussion is postponed to sec. 2.5.

Efficiency. In the case where many charged particles are present in the shower evolution, for example as a result of gluon splittings into quark-antiquark pairs, considering all dipoles as possible photon emitters prohibitively impacts efficiency,

due to the abundance of negative weighted events. However, since these $q\bar{q}$ pairs are usually close in phase space due to the collinear enhancement in their production, soft photon emissions will not resolve their individual charges if emitted outside the cone spanned by the dipole. Since the dominant contribution to the radiation pattern is from soft and collinear photons, the effect of all dipoles except that spanned by the $q\bar{q}$ pair in question is to pairwise approximately cancel. This applies to all cases where there are many final-state charge dipoles, and the obvious efficiency improvement is to identify the dominant dipole in each case. The solution we propose is to identify as spectator only the opposite-sign charge same-flavour (OSSF) particle which results in the smallest dipole invariant mass[1]. This scheme must be used with consideration of the process in question. In particular, whenever initial-final dipoles are important, this scheme will fail. It will also fail for any process involving decay products of W bosons, since these are not OSSF pairs. However, this scheme performs well in most non-resonant situations, and in addition, where there are neutral resonances this scheme will preserve their virtuality in the shower. We have verified that in all processes presented in section 2.4, the transverse momentum distributions and the resonance lineshapes are statistically in agreement between the unaltered shower and the efficiency-improved shower. The relevant settings to effect these options are detailed in appendix A.

Finally, we will discuss another important factor in any EW calculation, which has not yet been systematically addressed for a QED shower.

2.3 α and electroweak input schemes

Before presenting results from the QED parton shower, we briefly discuss EW input schemes and the treatment of α. For the evaluation of MEs in hard processes, it is most appropriate to use a value of α which resums higher-order corrections. Using

[1]This scheme is similar to the one implemented in PYTHIA, where new $f\bar{f}$ pairs are tracked manually.

$\alpha(0)$ for processes at scales of the EW gauge bosons or higher leads to logarithms of the type $\log(m_f^2/m_{Z/W}^2)$, which are large for light flavours f. To absorb these photonic vacuum polarisation corrections to the coupling, a commonly used choice is the $\alpha(m_Z)$ scheme. Alternatively, the G_μ scheme absorbs higher-order corrections to the renormalisation of the weak mixing angle. In the G_μ scheme, α is a derived parameter and does not run, so it will be denoted α_{G_μ}, without any scale dependence. However, since the difference between α in different schemes is formally subleading, we have the freedom to define a different scheme for radiative corrections [78]. In the case of NLO calculations, of course, this must be consistent in all parts of the NLO calculation to ensure cancellation of singularities. For the case of the shower, which is unitary, we are free to use a running α in the shower, analogously to QCD.

For photon emissions, since most will become long-distance photons (i.e. they will not split again), their QED coupling should be evaluated in the Thomson limit, so we choose $\alpha(0)$. This is because the photonic wavefunction renormalisation already exactly cancels the light-fermion logarithms in the renormalisation of the coupling constant. For photon splittings into fermions, we choose $\alpha(t)$, where t is the splitting variable, here the modified virtuality.

To implement these choices, and to allow for freedom in choosing the most appropriate EW input scheme in many different cases, some changes to the computation of the running α in SHERPA were necessary.

The scale dependence of α is given, in terms of the Thomson limit, by

$$\alpha(Q^2) = \frac{\alpha(0)}{1 - \frac{\alpha(0)}{3\pi}\left[\Pi_{\text{lep}}(Q^2) + \Pi_{\text{top}}(Q^2)\right] - \Pi_{\text{had}}(Q^2)}, \tag{2.3.1}$$

where each $\Pi_f(Q^2)$ term is the vacuum polarisation induced by species f. Π_{had} is fitted from data and implemented using a series of thresholds. Meanwhile, the analytically known Π_{lep} and Π_{top} have the form

$$\Pi_f(Q^2) = \frac{1}{3} - \left(1 + 2\frac{m_f^2}{Q^2}\right)\left(\sqrt{1 - 4\,\frac{m_f^2}{Q^2}}\,\log\left(\frac{1 - \sqrt{1 - 4m_f^2/Q^2}}{1 + \sqrt{1 - 4m_f^2/Q^2}}\right)\right). \tag{2.3.2}$$

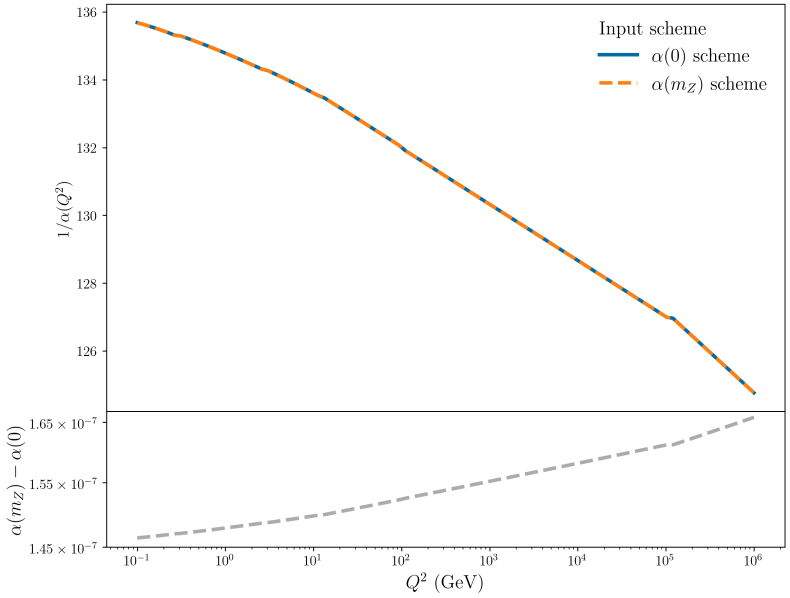

Figure 2.1: The running of α with energy, displayed as $1/\alpha$, in the $\alpha(0)$ scheme and in the $\alpha(m_Z)$ scheme.

However, when one defines α at a scale $\mu > 0$, the running must be computed from this defined value and scale. To achieve this, we first compute $\alpha(0)$ in the chosen scheme by rearranging eq. (2.3.1),

$$\alpha(0) = \frac{\alpha(\mu^2)(1 - \Pi_{\text{had}}(\mu^2))}{1 + \frac{\alpha(\mu^2)}{3\pi}\left[\Pi_{\text{lep}}(\mu^2) + \Pi_{\text{top}}(\mu^2)\right]}, \tag{2.3.3}$$

then use this value of $\alpha(0)$ to compute all necessary values of $\alpha(Q^2)$. Note that while it appears that the hadronic vacuum polarisation is needed as input here, in fact the dependence on Π_{had} disappears when the $\alpha(\mu^2)$ input scheme is used for the calculation of a hard process at the scale μ.

Figure 2.1 shows the scheme dependence of the running α. From the residual plot, it can be seen that taking the measured value at the Thomson limit and running to $Q^2 = m_Z^2$ using eq. (2.3.1) induces a small correction to the value of α as measured at the Z boson mass and evolved from there. However, the schemes are consistent to a high degree, showing that this method of modelling the running (in particular the hadronic vacuum polarisation) is valid.

For all the LO hard process calculations discussed in this thesis, we use the G_μ input scheme which takes $\{G_F, m_W, m_Z, m_H\}$ and the decay widths as inputs. In this

scheme, α is a derived parameter and does not run. However, as discussed above, we use a running α, defined in the $\alpha(0)$ scheme, for the radiative corrections. Wherever an external photon is present, it is considered to couple with $\alpha(0)$.

Note: processes with external Born photons

The discussion above is predicated on the Born-level process under consideration having no external photons. For a pure EW process at order n with ℓ external photons, the correct power counting would therefore be $\alpha(0)^\ell\alpha(m_Z^2)^{n-\ell}$, or similarly $\alpha(0)^\ell\alpha_{G_\mu}^{n-\ell}$ if the G_μ scheme is preferred. The factor $\alpha^{n-\ell}$ should be replaced by the appropriate power counting for the process under consideration.

2.4 Final-state results

In this section, we will present results produced using the QED parton shower. More work is needed to adapt the shower for the case of an electron-positron collider due to the electron structure function (see sec. 2.5), so here we focus on showing its applicability to charged lepton final states. We first use a test process $\nu_\mu\bar{\nu}_\mu \to e^+e^-$ at centre-of-mass energies of 91.2 GeV and 500 GeV, which are proposed energies of future e^+e^- colliders, where leptonic final states will be of great importance for precision measurements [79]. By colliding muon neutrinos in this case study, we fully isolate the final state to validate the method. Then, in section 2.4.2 we will study the leptonic decays of a Higgs boson. We will again isolate the QED final state by considering the Higgs to be produced through gluon fusion.

Throughout this section we will compare the QED parton shower with the YFS soft-photon resummation. To produce the following results, SHERPA's PHOTONS module was used [17]. This produces exclusive photons in the soft approximation using eikonal factors, which can be corrected either using collinear splitting functions, or exact higher-order soft-subtracted MEs can be used, if available. While the YFS

framework can incorporate higher-order corrections to any order, and next-to-next-to-leading order (NNLO) QED corrections have been implemented in SHERPA [18], here we use the publicly available NLO EW corrections in PHOTONS for the resonance decays presented here. Note that in all cases the total cross section is not changed from the LO cross section, so the results are comparable with the LO unitary parton shower without needing to account for differences in the total cross section. In addition, the extension of the YFS algorithm to charged particle pair production is included [1] (see chapter 4 for a detailed description of the YFS formalism and the extension). All charged particles are considered massive in the YFS framework, while in the parton shower, all charged leptons and the b and t quarks are massive, but other quarks are treated massless. For all results, AMEGIC was used for the tree-level ME generation [80].

2.4.1 Case study: $\nu_\mu\bar{\nu}_\mu \to e^+e^-$

We will first look at a process $\nu_\mu\bar{\nu}_\mu \to e^+e^-$. In this section we will present results from this process on the Z pole (with a centre-of-mass energy of 91.2 GeV) and at higher energy, $\sqrt{s} = 500$ GeV.

To analyse our QED parton shower in a way that is comparable to standard QCD parton showers, we will use jet observables. We define our QED jets as objects produced using a k_T jet algorithm (sometimes referred to as the Durham jet algorithm) [81,82]. The distance parameter is given by

$$d_{ij} = \min(p_{Ti}^2, p_{Tj}^2)\,\frac{\Delta R_{ij}^2}{R^2}, \tag{2.4.1}$$

where ΔR_{ij} is the distance in pseudorapidity and azimuthal angle, $\Delta R_{ij}^2 = \Delta\eta_{ij}^2 + \Delta\phi_{ij}^2$. We use a radius parameter $R = 1$. We choose to include electrons, muons and photons as input to the algorithm. This means we will miss contributions from photon splittings into $q\bar{q}$, pairs of light hadrons, or $\tau^+\tau^-$, but these are very rare (see chapter 4). Using a jet algorithm to define a final state means that we

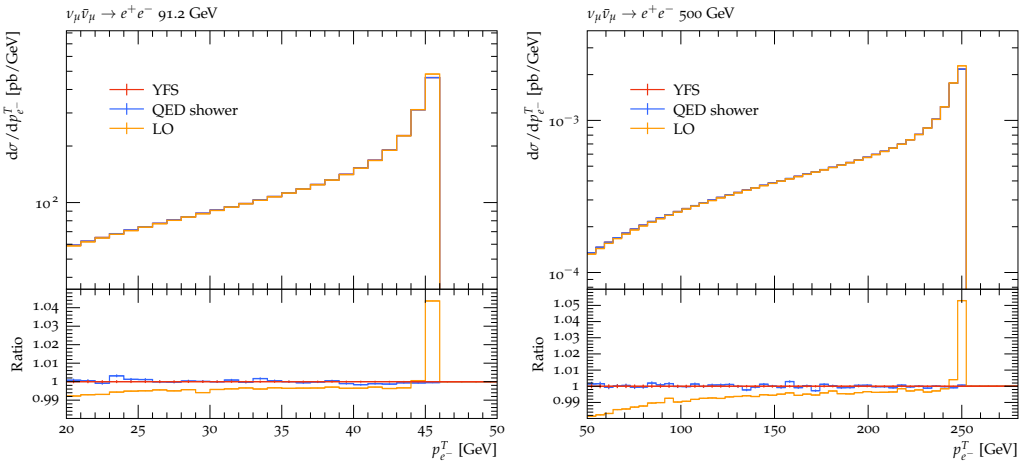

Figure 2.2: The electron transverse momentum in $\nu_\mu\bar{\nu}_\mu \to e^+e^-$, comparing the YFS soft-photon resummation with the QED shower prediction and the fixed-order LO distribution, for two different collider energies. **Left:** $\sqrt{s} = 91.2$ GeV. **Right:** $\sqrt{s} = 500$ GeV. The ratio plot shows the ratio to the YFS prediction.

are inclusive with respect to flavour, analogously to QCD parton showers. A k_T algorithm was chosen since it effectively reverses the parton shower evolution, which is approximately ordered in k_T (eq. (2.2.36)). The differential jet rate $d_{n,n+1}$ allows us to see at what scale the $(n+1)^{\text{th}}$ jet is formed, i.e. at what scale the emission happened. We will also study some observables, namely the photon multiplicity with different energy cuts, and the electron transverse momentum, which do not depend on this jet algorithm but similarly characterise our parton shower.

Figure 2.2 shows the cross section differential in the transverse momentum of the hardest electron for the process $\nu_\mu\bar{\nu}_\mu \to e^+e^-$, comparing the prediction from different methods of modelling QED radiation. In addition, we show the total size of the QED corrections by comparing to the fixed-order LO prediction for this observable. The left plot shows a centre-of-mass energy of 91.2 GeV, where it is clear that the YFS prediction and the shower agree to high precision. On the right, for $\sqrt{s} = 500$ GeV, the shower and YFS agree perfectly. For both collider energies, the radiative corrections are approximately 5% in the last bin and up to 1% throughout the distribution.

On the other hand, fig. 2.3 shows $\mathrm{d}\sigma/\,\mathrm{dlog}(d_{23})$, the differential cross section in the

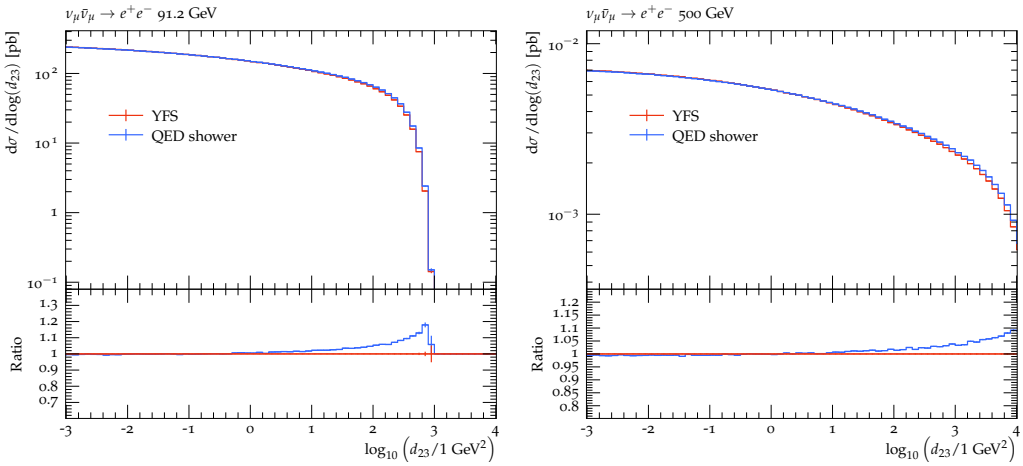

Figure 2.3: The 2-3 Durham jet rate in $\nu_\mu\bar{\nu}_\mu \to e^+e^-$, comparing the YFS method with the LO QED shower prediction for two different collider energies. **Left:** $\sqrt{s} = 91.2$ GeV. **Right:** $\sqrt{s} = 500$ GeV. The ratio plot shows the ratio to the YFS prediction.

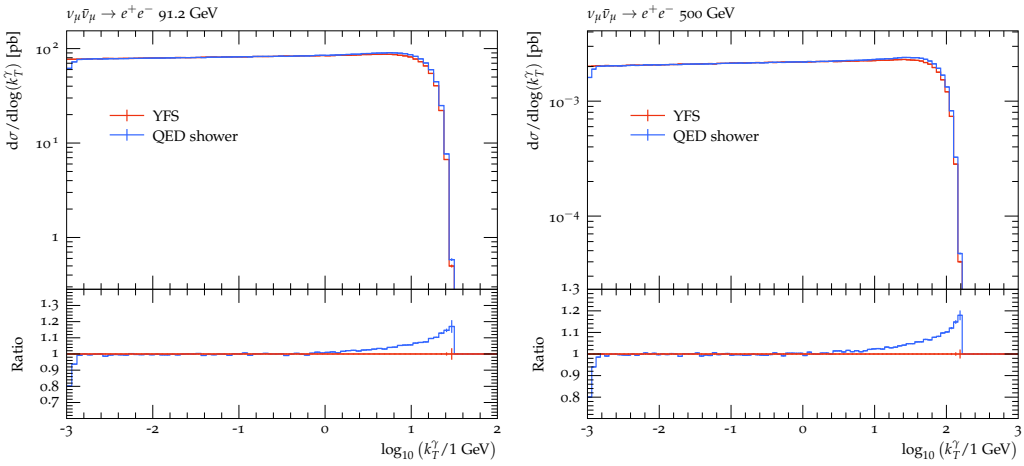

Figure 2.4: The third jet transverse momentum in $\nu_\mu\bar{\nu}_\mu \to e^+e^-$, comparing the YFS method with the LO QED shower prediction for two different collider energies. **Left:** $\sqrt{s} = 91.2$ GeV. **Right:** $\sqrt{s} = 500$ GeV. The ratio plot shows the ratio to the YFS prediction.

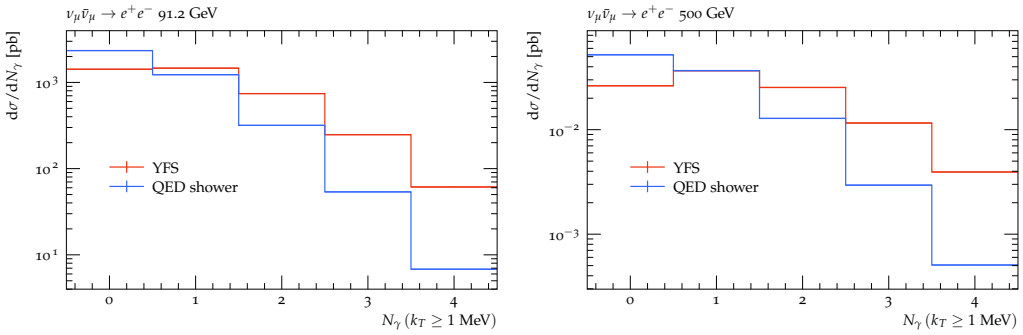

Figure 2.5: The multiplicity of photons with $k_T \geq 1$ MeV in $\nu_\mu\bar{\nu}_\mu \to e^+e^-$, comparing the YFS method with the LO QED shower prediction for two different collider energies. **Left:** $\sqrt{s} = 91.2$ GeV. **Right:** $\sqrt{s} = 500$ GeV.

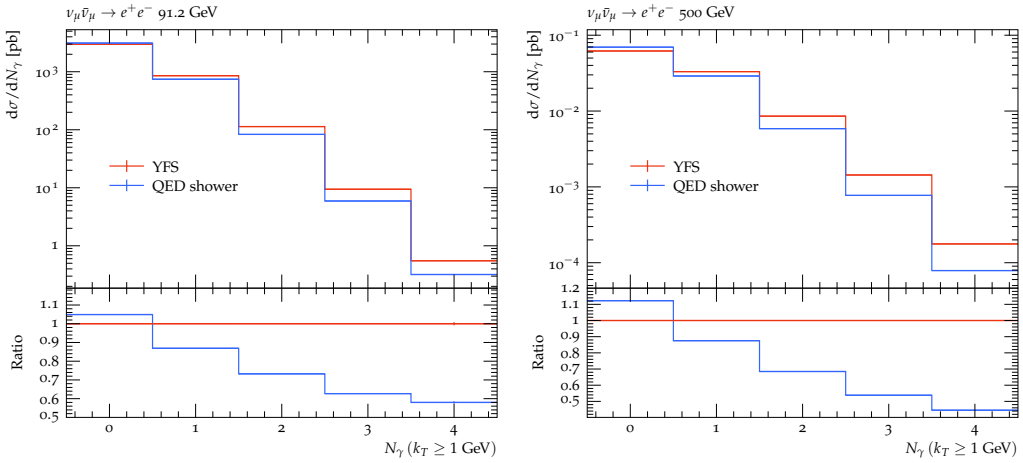

Figure 2.6: The multiplicity of photons with $k_T \geq 1$ GeV in $\nu_\mu\bar{\nu}_\mu \to e^+e^-$, comparing the YFS method with the LO QED shower prediction for two different collider energies. **Left:** $\sqrt{s} = 91.2$ GeV. **Right:** $\sqrt{s} = 500$ GeV. The ratio plot shows the ratio to the YFS prediction.

2-3 Durham jet rate, as described above. This characterises the hardest emission from the final state, which in the shower picture is the first emission. Compared to the YFS prediction, for both collider energies, the parton shower overestimates hard emissions. This is due to resumming the collinear logarithms, without including the interference effects at higher orders, which are negative. Fig. 2.4 similarly shows the third jet transverse momentum, where the jets are ordered in transverse momentum. The shape differences in this observable are very similar to the d_{23} plot, and are also up to 20% in size for the shower compared to the YFS.

Next, we study the multiplicity of photons produced by each method. We consider

two different transverse momentum cuts, 1 MeV and 1 GeV. The former is shown in figure 2.5, which clearly shows that the YFS method produces far more photons (with $k_T \geq 1$ MeV) than the shower does. This is a result of the resummation of all soft logarithms, where the number of photons increases as the energy decreases. While the shower splitting kernels do capture the leading soft divergences, the resummation is primarily of collinear logarithms and the veto algorithm, with its imposition of ordered emissions, does not produce as many soft photons as the unordered YFS approach. However, fig. 2.6 shows the photon multiplicity with a higher cutoff of $k_T \geq 1$ GeV. This considers only the semi-soft and hard photons which have a considerable impact on recoil of leptons and other inclusive observables. We can see that the shower prediction is much closer to the YFS prediction in this case, although large differences still emerge. The fact that both methods produce vastly different numbers of photons (especially soft photons) but agree for a large part of kinematic observables validates the QED parton shower as a description of higher-order QED radiation.

2.4.2 Leptonic Higgs decay

In this section, we will study the processes $gg \to H \to \mu^+\mu^-$ and $gg \to H \to e^+e^-\mu^+\mu^-$ in the Higgs effective field theory (HEFT). The HEFT is an effective field theory in which we obtain a direct effective coupling of gluons to the Higgs,

$$\mathcal{L} = \mathcal{L}_{\text{SM}} + g_{\text{HEFT}}\, G_a^{\mu\nu} G^a_{\mu\nu} H + \ldots, \tag{2.4.2}$$

by integrating out the top quark in the SM loop-induced production of a Higgs via gluon fusion. In the SM, other quarks also contribute to the loop, but since the top Yukawa coupling is much greater than the other quark Yukawa couplings due to its large mass, only this contribution must be considered in the HEFT.

We study gluon-induced Higgs production at the LHC, where the colliding protons have a centre-of-mass energy of 13 TeV. We use the PDF set PDF4LHC21 from

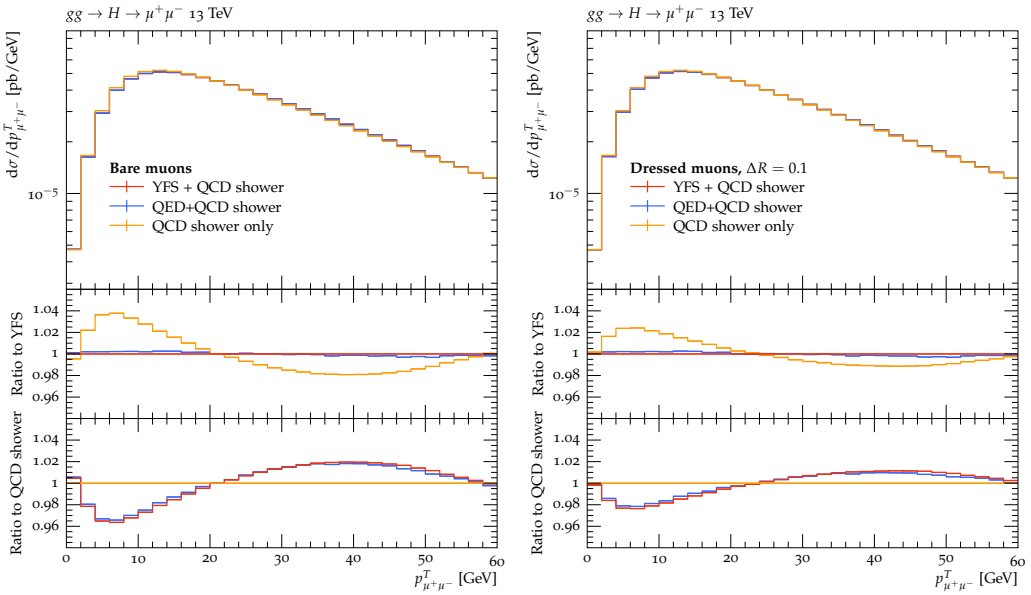

Figure 2.7: The dimuon transverse momentum in the $gg \to \mu^+\mu^-$ process, comparing the YFS prediction with the interleaved QCD+QED shower. The pure QCD shower prediction is also included for comparison. **Left:** bare muons, **Right:** photon-dressed muons with a cone size $\Delta R = 0.1$.

the LHAPDF library [83]. SHERPA's default parton shower, CSSHOWER, was used for the initial-state QCD shower [44]. Beam remnants, hadronisation, and multiple interactions were not modelled.

$gg \to H \to \mu^+\mu^-$

The LO cross section for $gg \to \mu^+\mu^-$ at the 13 TeV LHC in the HEFT is 0.0028662(1) pb. In this section we present differential cross sections in various kinematical observables for bare muons and dressed muons. The muons are dressed with photons in a cone of radius $\Delta R = 0.1$, where $\Delta R = \sqrt{\Delta\eta^2 + \Delta\phi^2}$. The primary muons, whether bare or dressed, are subject to cuts on transverse momentum, $p_\mu^T > 10\,\text{GeV}$, and rapidity, $\left|y_\mu\right| < 2.5$. We compare the interleaved QCD+QED shower presented in this chapter with the scenario where no QED radiation is included (QCD shower only) in addition to the YFS soft-photon resummation supplemented with exact NLO corrections.

First, figure 2.7 shows the dimuon transverse momentum distribution. The shape of

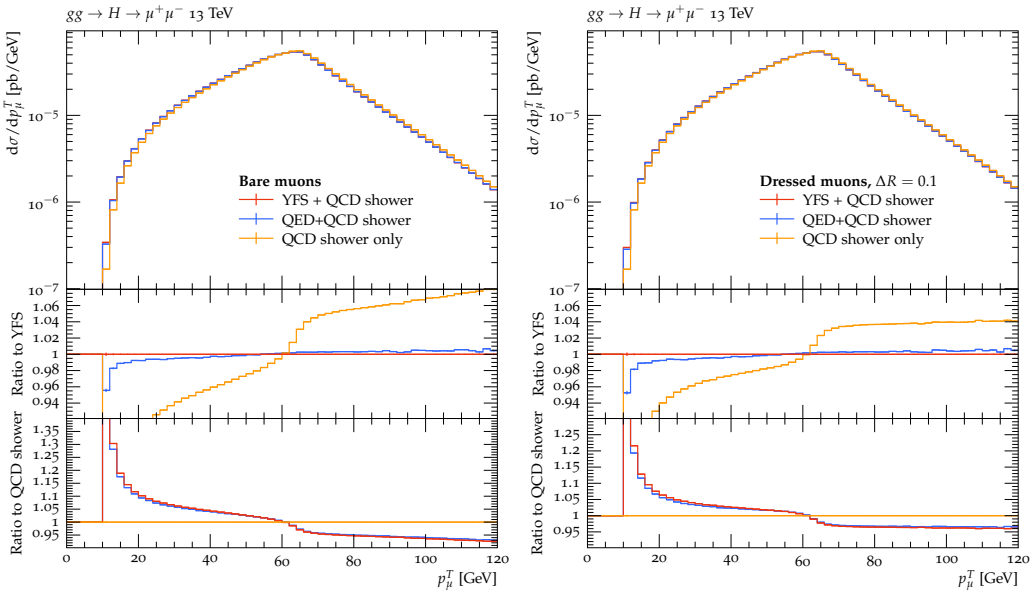

Figure 2.8: The hardest muon transverse momentum in the $gg \to \mu^+\mu^-$ process, comparing the YFS prediction with the interleaved QCD+QED shower and the pure QCD shower prediction. We show ratios to YFS (upper ratio plot) and to the QCD shower only (lower ratio plot). **Left:** bare muons, **Right:** photon-dressed muons with a cone size $\Delta R = 0.1$.

the distribution is dominated by QCD initial-state radiation, which induces transverse recoil on the whole final state. However, there are small effects from QED radiation recoil, as can be seen in the lower ratio plot. As can be seen from the upper ratio plot, in both bare muons and dressed muons, the interleaved shower agrees very well with the YFS prediction.

The distribution of the muon transverse momentum, shown in fig. 2.8, is given already at LO by the kinematics of the Higgs decay. Even without any transverse initial-state radiation, there is a peak at $p_\mu^T = m_H/2$. The distribution including only initial-state QCD radiation is shown in the plot. The addition of QED final-state radiation results in a softer hardest muon, as can be seen from the lower ratio plot. Comparing the two QED radiation methods in the upper ratio plots, we see that the full YFS including exact NLO corrections produces the largest recoil corrections, though the soft logarithms account for the bulk of these. The interleaved QED+QCD shower is in good agreement with YFS for both bare and dressed muons, with better

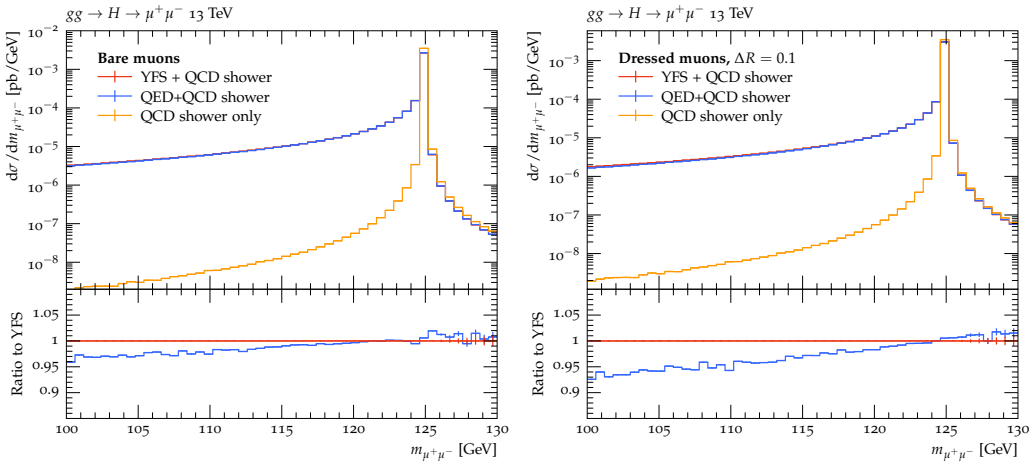

Figure 2.9: The dimuon invariant mass in the $gg \to \mu^+\mu^-$ process, comparing the full YFS prediction with the interleaved QCD+QED shower. The pure QCD shower prediction is also included for comparison. **Left:** bare muons, **Right:** photon-dressed muons with a cone size $\Delta R = 0.1$.

than 1% precision.

Finally, we study the Higgs lineshape in figure 2.9. This plot shows the cross section differential in the dimuon invariant mass, for bare muons (left) and cone-dressed muons (right) with a cone size of $\Delta R = 0.1$. We can see that the QCD shower alone produces very few events below the resonant peak, since if the final state is produced on the resonance, it cannot radiate further. The ratio plot shows the interleaved shower compared to the YFS prediction. For bare muons, we see that the shower is in very good agreement with YFS in the vicinity of the resonance. Below the resonance, the shower underestimates the cross section with respect to YFS, since it does not contain NLO-accurate hard photon emissions. This disagreement is accentuated for the case of dressed muons, since the kinematical impact of collinear radiation is decreased when muons are cone-dressed and hard wide-angle radiation contributes more strongly to the lineshape.

$gg \to H \to \mu^+\mu^- e^+ e^-$

The LO cross section for $gg \to \mu^+\mu^- e^+ e^-$ at the 13 TeV LHC in the HEFT is 0.00084(1) pb. Due to the complex final state, simulations for this process are

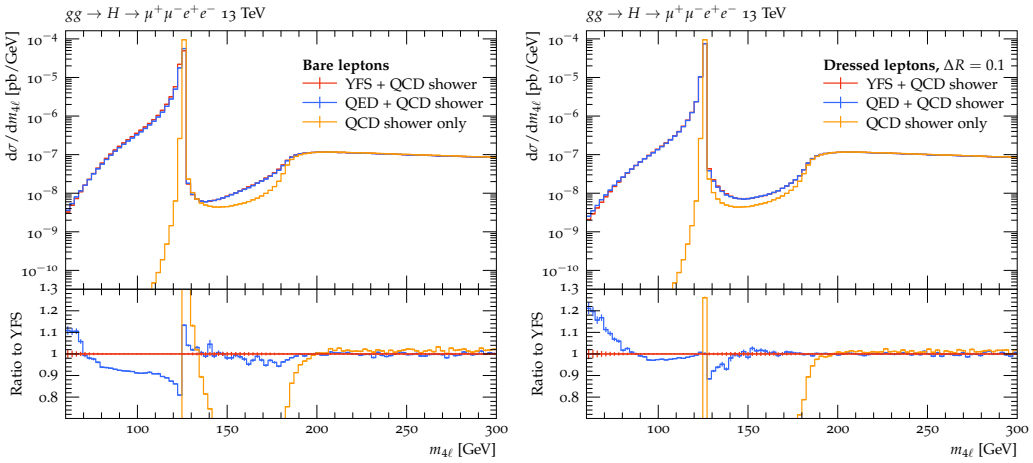

Figure 2.10: The four-lepton bare invariant mass in $gg \to \mu^+\mu^-e^+e^-$, comparing the the QCD shower and YFS prediction with the prediction from an interleaved QCD+QED shower. The pure QCD shower prediction is also included for comparison. **Left:** bare leptons, **Right:** photon-dressed leptons with a cone size $\Delta R = 0.1$.

significantly more expensive than the processes we have studied so far. However, we have found that the interleaved shower is faster or the same speed as the QCD shower plus YFS simulations, when the one-spectator efficiency option described in section 2.2.6 and in the appendix is enabled. We have validated that even for this more complex final state, the one-spectator option reproduces the results of the full dipole shower but with much higher statistical precision. In this section, we will present distributions in the four-lepton invariant mass $m_{4\ell}$, the hardest Z boson transverse momentum $p_Z^T = \max((p_{e^+} + p_{e^-})^T, (p_{\mu^+} + p_{\mu^-})^T)$, and the hardest lepton transverse momentum p_ℓ^T. The primary electrons and muons are subject to cuts on transverse momentum, $p_\ell^T > 10\,\text{GeV}$, and rapidity, $|y_\ell| < 2.5$. We compare the interleaved QCD+QED shower presented in this chapter with the YFS soft-photon resummation including collinearly-approximated ME corrections.

Figure 2.10 shows the four-lepton invariant mass differential cross section. The left plot shows the observable for bare leptons, while the right plot shows the invariant mass of four primary photon-dressed leptons. The main features of the lineshape are the Higgs resonance at 125 GeV and the two on-shell Z threshold at 180 GeV.

Above the threshold, the interleaved shower is in perfect agreement with the YFS approach combined with the QCD shower. Between the Higgs resonance and the di-Z threshold, the interleaved shower produces fewer events for the bare-lepton observable. This is due to the shower producing fewer soft and collinear photon emissions than YFS, as can be seen in the dressed lepton plot where this feature disappears. Of more note are the differences in the two methods at the Higgs mass and just below it. The YFS approach correctly resums all the soft logarithms and hence produces more events just below the Higgs resonance, where the leptons have only lost energy through relatively soft radiation. This effect is clearly mitigated in the dressed lepton plot, where recoil from photon emissions is minimised. The QED shower, by contrast, leaves more bare-lepton events exactly on the Higgs pole. We can clearly see that both QED radiation methods produce a very different distribution from that predicted by the QCD shower alone, which is clearly lacking modelling of final-state radiation.

Next, we study the Higgs decay to Z bosons by reconstructing the momentum of each Z and plot the hardest Z transverse momentum in fig. 2.11, using the flavour identification of bare leptons (left) or dressed leptons (right). Here, we expect better agreement between the QED radiation methods, since QED radiation is already only a 3-6% correction to the distribution predicted by the LO QCD shower (as seen from the lower ratio plots). Indeed, we see perfect agreement between the YFS approach and the QED shower approach for both bare and dressed leptons, when each is combined with the initial-state QCD shower. Unlike the $H \to \mu^+\mu^-$ case in fig. 2.8, there is no peak at $m_H/2$ because the decay preferentially proceeds with one Z on-shell (since both cannot be on-shell). Note that since the p_T cut is applied to the leptons, the reconstructed Z bosons can have zero transverse momentum.

In figure 2.12 we show the cross section differential in the hardest lepton transverse momentum. The left plot shows the hardest bare lepton p_T, while the right plot shows the hardest dressed lepton p_T. The spectrum has a peak at $m_Z/2$ due to the preference for on-shell Z production in the Higgs decay. There is very good

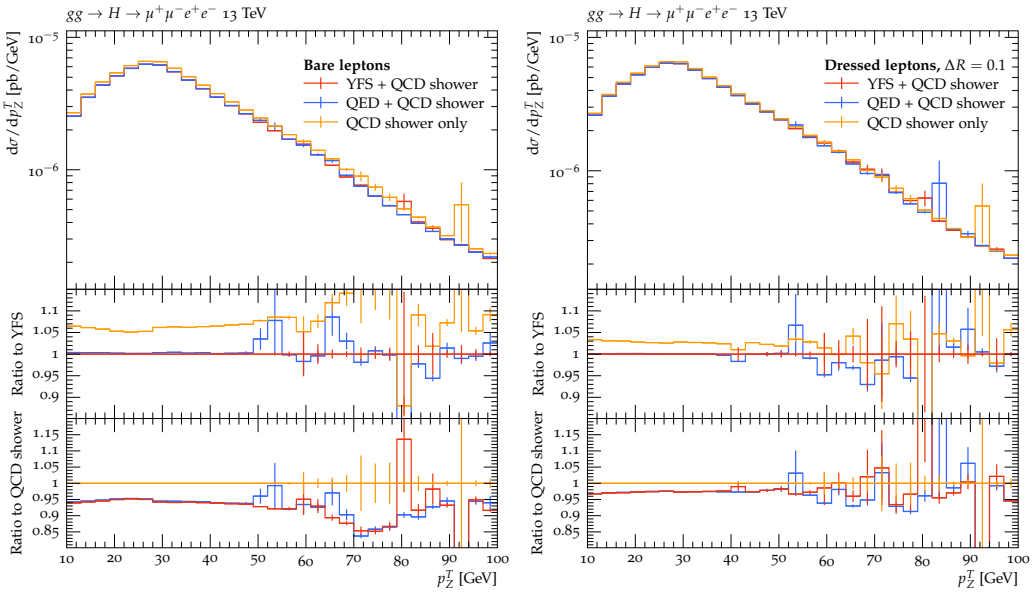

Figure 2.11: The hardest Z boson transverse momentum in $gg \to \mu^+\mu^- e^+ e^-$, comparing the QCD shower and YFS prediction with the prediction from an interleaved QCD+QED shower. The pure QCD shower prediction is also included for comparison. The upper ratio plot shows the ratio to the YFS + QCD shower prediction, while the lower shows the ratio with respect to the QCD shower alone. **Left:** bare leptons, **Right:** photon-dressed leptons with a cone size $\Delta R = 0.1$.

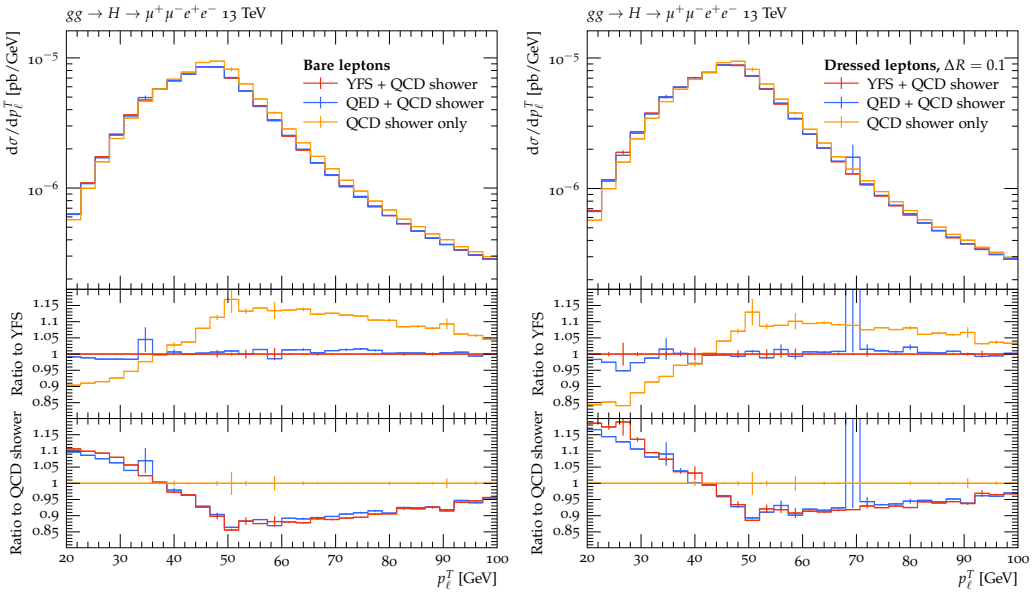

Figure 2.12: The hardest lepton transverse momentum in $gg \to \mu^+\mu^-e^+e^-$, comparing the QCD shower and YFS prediction with the prediction from an interleaved QCD+QED shower. The pure QCD shower prediction is also included for comparison. The upper ratio plot shows the ratio to the YFS + QCD shower prediction, while the lower shows the ratio with respect to the QCD shower alone. **Left:** bare leptons, **Right:** photon-dressed leptons with a cone size $\Delta R = 0.1$.

agreement between the YFS prediction and the interleaved shower. Both methods predict a different shape distribution than the LO QCD shower, with differential cross section differences up to 15% for both bare and dressed leptons. Note that the YFS prediction here includes exact NLO QED corrections to the radiation pattern, and so produces more hard photonic radiation than the shower. This results in the interleaved shower predicting a slightly higher hardest lepton p_T, which is visible when photonic radiation is not recombined.

Figure 2.13 shows the impact of the efficiency improvement described in section 2.2.6. In this approximation, rather than including all possible charged dipoles for photon emission, we identify OSSF pairs and consider only the dipoles spanned by these pairs to radiate photons. In addition to improving efficiency, this is a form of resonance-awareness which can help to avoid unphysical exchanges of momentum between decaying resonances. Resonance-identification methods have been shown to reduce the tendency of real-radiation modelling methods to distort lineshapes [67,84,85]. In these plots we show the invariant mass of the Z boson, reconstructed from particular flavours, for various methods in $gg \to H \to \mu^+\mu^- e^+ e^-$. Only QED radiation is included, since the initial-state QCD radiation affects all methods in the same way. The top-left and top-right plots show the e^+e^- invariant mass for bare and dressed electrons respectively, while the bottom two plots show the $\mu^+\mu^-$ invariant mass. The LO prediction is shown for comparison, which is the case where no radiation effects are included. We see that the all-dipoles case, as compared to the OSSF dipoles only case, performs far worse in terms of statistics. This plot shows the result of simulating 10^9 weighted events for the YFS, OSSF-only and LO predictions, and 10^{10} weighted events for the all-dipoles shower. Despite this, we can clearly see the impact of large numbers of negative weights. The statistical precision is not sufficient to verify whether the unconstrained momentum transfer distorts the Z invariant mass spectrum, however, we can clearly see from these plots that the OSSF approximation is a very good one.

The lower ratio plot of each plot in fig. 2.13 shows the impact of lepton definitions

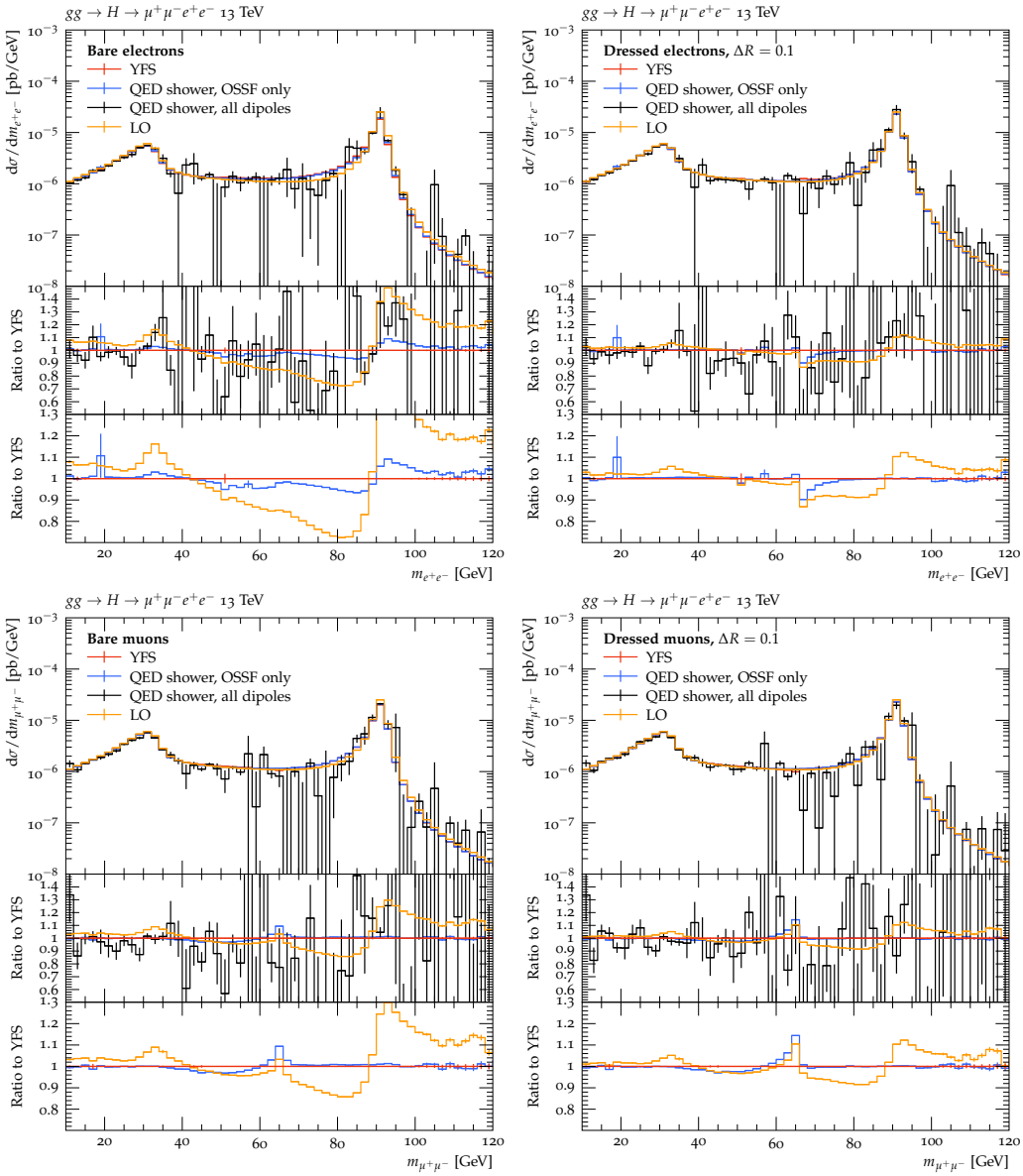

Figure 2.13: The dilepton invariant mass in the $gg \to \mu^+\mu^- e^+ e^-$ process, comparing the QED shower either with OSSF dipoles only, or with all dipoles. The YFS resummation and LO prediction are also shown for comparison. Both ratio plots are with respect to the YFS resummation, but the all-dipoles case is not shown in the lower ratio plot. **Top:** electrons, **Bottom:** muons; **Left:** bare leptons, **Right:** photon-dressed leptons with a cone size $\Delta R = 0.1$.

on the invariant mass distribution. We see that the muon invariant mass is much less impacted by QED radiation on the bare level, due to its higher mass/charge ratio. The differences between YFS and the shower are also greater for the bare electrons than for the bare muons, which is due to differences in how the IR cutoff is implemented in each case. It is clear that dressing the leptons with photons eliminates most of the differences between the YFS and QED shower methods, since only the kinematic impact of the hardest photons (or semi-soft wide-angle photons) remains. We will study the interplay of QED radiation and lepton definitions further in chapter 4.

In this section we have presented results from the final-state QED parton shower. An initial-state QED shower is not usually phenomenologically relevant at the LHC, although as described in section 2.2, all initial-initial and initial-final dipoles are implemented in the shower presented here. However, initial-state QED radiation is of the utmost importance in lepton-lepton colliders. Before concluding this chapter, we outline important considerations when implementing the initial-state QED parton shower for electron-positron colliders.

2.5 The initial-state QED parton shower for e^+e^- colliders

For electron-positron colliders, it is essential to model initial-state radiation both for luminosity measurements and for processes of interest. For example, at low-energy e^+e^- colliders, the measured rate of e^+e^- to hadrons is used to extract the hadronic vacuum polarisation via the optical theorem [4]. Understanding these processes requires precise modelling of the QED radiation produced from the initial and final states. At future high-energy e^+e^- colliders such as the FCC-ee, the precision will be high enough such that a simple structure function approach is unlikely to be sufficient to describe the makeup of the initial states. In both these cases, the YFS approach

can be used [86]. However, we stand to benefit significantly from the resummation of collinear logarithms, which are formally of the same size as soft logarithms. We have seen in this chapter that they can be very important in practice, too, especially when the centre-of-mass energy is far from a resonance (e.g. some low-energy colliders and any future collider above the Z mass). NLO corrections, and possibly even higher orders, are also necessary to reach the precision of future experiments. There have been many tools developed for NLO parton shower matching for QCD initial states, from which we can take inspiration. These ideas will be discussed further in chapter 3, but first we discuss the necessary prerequisite of a parton shower for electron-positron initial states.

2.5.1 The electron structure function

In QCD, to obtain the PDFs for hadrons, they must be fitted to data and then evolved numerically using the DGLAP equations. In QED, obtaining a structure function for the electron is more straightforward. The DGLAP equations for QED can be solved exactly to LL accuracy, using the initial condition

$$f_e(x,0) = \delta(1-x), \tag{2.5.1}$$

for the electron or positron (in pure QED they are identical to all orders; in the EW theory they are identical at LO). With the inclusion of approximate higher-order corrections and a modification of the collinear exponentials to take into account soft radiation, this results in the LL structure function

$$f_e(x,Q^2) = \beta \frac{\exp\left(-\gamma_E\beta + \frac{3}{4}\beta_S\right)}{\Gamma(1+\beta)}(1-x)^{\beta-1} + \beta_H \sum_{n=0}^{\infty} \beta_H^n \mathcal{H}_n(x), \tag{2.5.2}$$

where $\beta = \frac{\alpha}{\pi}\left(\log\left(\frac{Q^2}{m_e^2}\right) - 1\right)$. This form of β comes from integration over all phase space available for the emission of soft photons in the YFS framework, thus allowing the resummation of soft radiation effects in the collinearly-derived structure function. The soft photon residue β_S can be set either to β, or to $\eta = \frac{\alpha}{\pi}\log\left(\frac{Q^2}{m_e^2}\right)$. The β_H

logarithms which come with the hard coefficients $\mathcal{H}_n$ have the same freedom: one can choose $\beta_H = \beta_S$, or define a mixed scheme in which $\beta_S = \beta$, $\beta_H = \eta$ [86, 87].

Note that beyond LO+LL accuracy, the initial condition is a mixed electron-photon state. The NLO PDFs have been recently derived in the one-flavour QED case [88–90]. These are expected to be implemented in a future version of MadGraph [91]. When these PDFs are extended to the case of multiple fermions, and can be implemented in an event generator in a similar way to hadron PDFs, this will allow for fully NLO-accurate simulations of events at e^+e^- colliders. With the present LO+LL structure function, any calculation is formally limited by the structure function accuracy. This will be an active area of future research.

The LL structure function, eq. (2.5.2), has an integrable singularity at $x = 1$, since $0 < \beta < 1$. This means that provided the observable of interest does not diverge as $x \to 1$, the result after integration over x will be finite, despite the singularity. However, MC integration and event generation rely on sampling from $f_e(x)$, and any numerical algorithm must have an upper limit $x_{\max}$. For convenience, in the following, we introduce a small positive number ϵ, defined as $x_{\max} = 1 - \epsilon$. However, no matter how small ϵ is taken, significant contributions to the total cross section are missed, due to the singularity in $f_e(x)$.

This problem is traditionally solved by using the analytic knowledge of the singularity structure to rescale the structure function near the numerical upper limit, to ensure the correct total cross section is obtained. We define a second small number δ, such that $\delta > \epsilon$. Then, assuming that the partonic cross section is roughly flat in x for $x > 1 - \delta$, we can write

$$\int_{1-\delta}^{1-\epsilon} \mathrm{d}x\, \lambda(\epsilon, \delta)\, f_e(x, Q^2) = \int_{1-\delta}^{1} \mathrm{d}x\, f_e(x, Q^2), \tag{2.5.3}$$

introducing the scale factor $\lambda(\epsilon, \delta)$. Using the asymptotic form of eq. (2.5.2) and solving for λ, we obtain

$$\lambda(\epsilon, \delta) = \frac{(\delta/\epsilon)^\beta}{(\delta/\epsilon)^\beta - 1}, \tag{2.5.4}$$

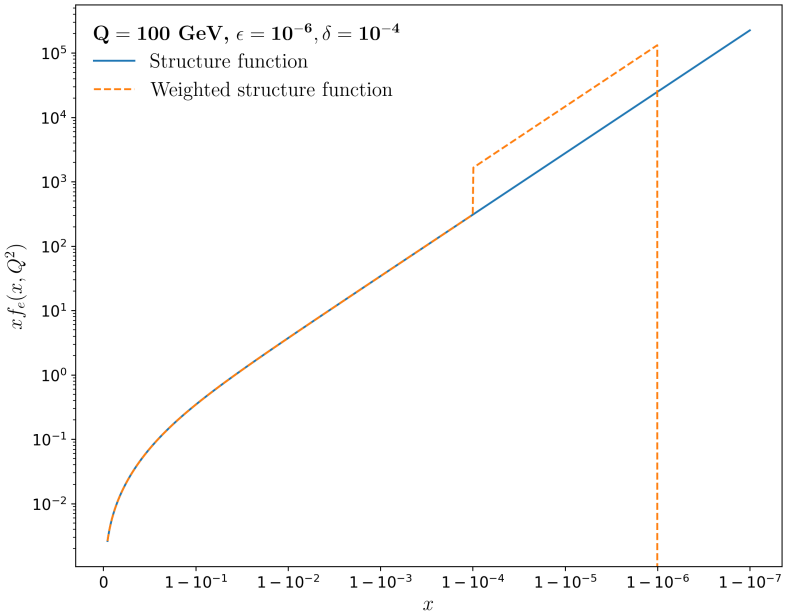

Figure 2.14: The LL electron structure function at a scale 100 GeV, compared to the weighted structure function usually used for MC integration and event generation.

where β is evaluated at $Q^2 = s$. Then the structure function $W_e^\lambda(x, Q^2)$ used in MC integration is

$$W_e^\lambda(x, Q^2) = \begin{cases} f_e(x, Q^2) & 0 \leq x \leq 1 - \delta \\ \lambda(\epsilon, \delta) f_e(x, Q^2) & 1 - \delta < x < 1 - \epsilon \\ 0 & \text{else.} \end{cases} \tag{2.5.5}$$

Figure 2.14 shows the logarithmic behaviour of the structure function as $x \to 1$, at a scale $Q = 100\,\text{GeV}$. The weighted structure function, eq. (2.5.5), is also shown, for the choices $\epsilon = 10^{-6}, \delta = 10^{-4}$. We can see that the weighted structure function is discontinuous at the point $x = 1 - \delta$, and therefore is no longer a valid solution of the DGLAP equations. If the weight $\lambda(\epsilon, \delta)$ is also applied in the parton shower, this will lead to an overestimate of emissions into the region $1 - \delta < x < 1 - \epsilon$, which is unphysical.

We can solve some of these problems by instead considering the unweighted structure function with a cutoff ϵ, and defining a component proportional to $\delta(1 - x)$ which

contains the missing cross section contributions. This is defined as

$$W_e^{\delta}(x,Q^2) = \begin{cases} f_e(x,Q^2) & 0 \leq x \leq 1-\epsilon \\ 0 & 1-\epsilon < x < 1 \\ C\delta(1-x) & x = 1. \end{cases} \tag{2.5.6}$$

Solving for C in the same way as above, again approximating $Q^2 = s$, we obtain $C = \epsilon^{\beta/2}$.

This method, rather than smearing the missing cross section contributions across the high-x region, adds it into the $x = 1$ region. This has the advantage that a whole kinematical region is not affected by the overweighting. It is also more physically meaningful when considering photon emissions, since we define all emissions within the $1 - \epsilon < x < 1$ region to be unresolvable, both in terms of detectability and in their kinematical effects. Therefore, they are combined with the $x = 1$ no-emission piece. This implementation is less convenient, however, since the phase space has four distinct regions in e^+e^- collisions:

- $x_1 < 1-\epsilon$, $x_2 < 1-\epsilon$
- $x_1 < 1-\epsilon$, $x_2 = 1$
- $x_1 = 1$, $x_2 < 1-\epsilon$
- $x_1 = 1$, $x_2 = 1$.

Therefore, the event generation must be completed in four phases. In SHERPA, this process has not been automated.

Both methods for dealing with the integrable divergence in the electron structure function work well for LO computations. However, neither solve some of the problems which arise from a unitary parton shower acting on the electron-positron initial state.

2.5.2 Implementation of a QED initial-state shower

There are a few difficulties with implementing the QED parton shower, as described in section 2.2, for the case of an e^+e^- collider.

One challenge lies in embedding the structure function into the veto algorithm (*see* sec. 2.2.3). The parton shower splitting function includes the ratio of particle luminosities $\mathcal{L}(r_{\widetilde{ij},\tilde{k}}(\{a\}))/\mathcal{L}(\{\tilde{a}\})$. In the initial-state splitting $e^\pm \to e^\pm\gamma$, both the numerator and the denominator of this fraction contain the LL electron structure function:

$$\frac{\mathcal{L}(r_{\tilde{aj},\tilde{b}}(\{a\}))}{\mathcal{L}(\{\tilde{a}\})} = \frac{\frac{x}{z_{aj,b}} f_e\left(\frac{x}{z_{aj,b}}, Q^2\right)}{x f_e(x, Q^2)}, \tag{2.5.7}$$

where $z_{aj,b}$ is the splitting variable defined in eq. (2.2.20). We can see from this equation that the splitting function diverges for $z_{aj,b} \to x$. In addition, we can see that as $x \to 1$, the emission phase space becomes restricted to very soft emissions, i.e. $z_{aj,b}$ must be very close to 1, for the argument of the structure function to be less than unity.

The fact that this ratio contains an additional divergence is not the only difficulty. The veto algorithm requires an overestimate $g(t)$ of the splitting function, which is needed before any splitting kinematics are computed. This means we need an expression which overestimates eq. (2.5.7) which is independent of $z_{aj,b}$. The solution to this appears straightforward: applying the same $x_{\max}$ logic as before leads to an x-dependent overestimate given by

$$g(t) \supset \frac{x_{\max} f_e(x_{\max}, Q^2)}{x f_e(x, Q^2)}. \tag{2.5.8}$$

We would like to include the effect of radiation which, in a backwards-evolution picture, takes the initial electron/positron line into the $x_{\max} < x < 1$ region. This radiation is not restricted to be soft, so may be very relevant to a range of observables. We can achieve this to a first approximation by allowing the generation of $z_{aj,b} > x/x_{\max}$. However, if the current x is above $x_{\max}$, further emissions are forbidden. These further emissions must be soft, since $z_{aj,b}$ is restricted to be very close to unity,

so are unlikely to be relevant phenomenologically. This choice allows the dominant effects of emission into the kinematically favoured $x \to 1$ region to be included. Eq. (2.5.8) is not always strictly an overestimate in this case, but if this is problematic in practice, it is always possible to reweight it.

Correctly overestimating the splitting function introduces another difficulty, however. The veto algorithm requires the new scale t to be calculated according to the distribution of $g(t)$, as in eq. (2.2.24) and eq. (2.2.38). For any sensible (small) value of ϵ, this calculation is likely to occasionally produce a new scale which is, in floating-point arithmetic, indistinguishable from the current scale. When this happens, the algorithm will stall. By imposing a limit on the size of the overestimate used to generate t, one can produce radiation using the shower. As expected, however, a dependence on the form of the overestimate and on ϵ remains, so the results cannot be trusted.

To avoid the divergence as $z_{aj,b} \to x$, we can flatten the function which is sampled using standard MC techniques [54]. By sampling logarithmically in $x - z_{aj,b}$, we flatten the first-order $1/(x - z_{aj,b})$ pole.

To deal with large overestimates in the generation of new scales, which will be necessary even with the above modification since $f_e(x_{\max}, Q^2)$ is very large numerically, we can use the method of analytic weights (*see* section 2.2.3). However, this method has not been used before for large overweights and so should be stringently tested. It will also have a negative impact on MC statistics, as with any method which introduces large weight fluctuations between events.

The results of these new developments in modelling the e^+e^- initial state radiation will be detailed in a future publication, and made available in a future release of SHERPA.

2.6 Conclusions

In this chapter we have presented novel results from a QCD+QED final-state parton shower. After outlining the construction of a parton shower and detailing QED-specific considerations, we validated our implementation using a test process $\nu_\mu\bar{\nu}_\mu \to e^+e^-$ at two different energies: just above the s-channel resonance and far above it. We saw that the parton shower produces a radiation pattern which is in good agreement with that produced by the YFS soft-photon resummation, when the latter is supplemented with exact NLO corrections.

We also presented results showing the applicability of our method to phenomenological studies. We studied the production of a Higgs boson via gluon fusion and its decay to two or four leptons. We found that for $H \to \mu^+\mu^-$, the QED shower predictions agreed with the YFS predictions to within 1% for transverse observables and within 5% for the Higgs invariant mass. Similarly, for the four-lepton final state, the transverse momentum distributions of the hardest lepton and hardest Z were in very good agreement. The differences in the Higgs invariant mass were larger for this decay, but localised, as expected, just below the resonant H pole. The interleaved shower presented in this chapter thus produces useful predictions, for a range of processes, which are consistent with other methods for calculating QED radiative corrections. We also validated the use of a primary dipole identification method to preserve resonance lineshapes and improve efficiency.

Finally, we discussed the differences which arise when considering an electron-positron collider. We presented the situations in which the current algorithm is insufficient, and outlined methods to solve these difficulties. This will be an important topic of future research, becoming ever more relevant as future collider plans are confirmed.

In the next chapter, we extend our interleaved QCD+QED shower by matching it to NLO. We outline the proof of the MC@NLO method for QED and for QCD+QED, and discuss details of the implementation. We will show that matching to NLO

improves the accuracy of our shower perturbatively while retaining the resummation accuracy of the parton shower which we have demonstrated in this chapter.

The interleaved dipole shower was implemented in the event generator SHERPA and will be incorporated in a future release in the SHERPA 3 series. All analyses and plots were made using RIVET [92, 93].

Chapter 3

QED MC@NLO

3.1 Introduction to NLO matching

As was described in section 1.2.3, there are various difficulties in computing NLO observables numerically, but these have been solved by using phase-space slicing or subtraction schemes. In this chapter we will review the solution to the additional problem of incorporating these NLO calculations into an event generator, in particular, of combining an NLO calculation with a parton shower.

Around the turn of the 21st century, LO QCD plus parton shower predictions were insufficient to describe the multi-jet final states being produced at colliders. As a result, LO parton shower merging was developed [55,56], which allows one to describe each additional jet with its own full matrix element correction to the parton shower approximation. However, for many processes including Higgs production via gluon fusion, large K-factors were observed in comparisons to data, indicating that NLO virtual corrections are non-negligible in many cases. This led to the development of matching methods.

The idea of NLO parton shower matching is to produce a prediction for an observable $\langle O \rangle$ which contains the parton shower factor (containing emission probabilities and Sudakov form factors), but which reproduces the correct NLO value for the

observable, i.e.

$$\langle O \rangle^{\text{Matched}} = \langle O \rangle^{\text{NLO}} + \mathcal{O}(\alpha^{m+2}), \tag{3.1.1}$$

for an observable which is $\mathcal{O}(\alpha^m)$ at LO.

As was explained in detail in chapter 2, a parton shower resums the leading logarithms associated with the emission of soft or collinear radiation, whilst assuming perfect cancellation of both the IR singularities and the finite parts of the NLO contribution to an observable. Contrary to analytic resummation, a parton shower produces exclusive final states containing a number of additional particles. The radiation pattern is, however, formally only correct in the soft and collinear limits, although the choice of finite parts of the splitting functions can improve the description away from these limits. An NLO matched parton shower, on the other hand, describes the first emission radiation pattern at LO everywhere in phase space. This is interpolated with the parton shower resummed prediction in the soft and collinear regions. Importantly, in contrast to LO merging predictions, the total cross section is the correct NLO one and the NLO K-factor is present in observable predictions. The K-factor is defined by $\sigma^{\text{LO}}(1+K) = \sigma^{\text{NLO}}$, sometimes called a global K-factor, and usually quoted as a percentage. In MC event generators, an NLO matched parton shower allows us to carry out a full simulation of events at this accuracy, including hadronisation, hadron decays, multiple interactions and underlying event.

The MC@NLO [42] and POWHEG [40] methods were developed to solve the problem of double-counting the first emission, while exponentiating the appropriate parton shower factors. Both methods utilise so-called additive matching, but some newer matching methods use multiplicative matching, for example KRKNLO [43], or a combination of both types. In this chapter, we will focus exclusively on the MC@NLO method, since it only exponentiates the IR-singular parts of the real correction. This is an advantage over POWHEG, which sometimes suffers from artificial local K-factors caused by exponentiating large hard real corrections. However, MC@NLO has the disadvantage that negative event weights occur when the parton shower overestimates the NLO real-emission pattern. This most often occurs when the shower is leading-

colour and is matched to full-colour NLO [94]. However, we will use weighted events to produce distributions shown here; in addition, we do not need to pass events through a detector simulation, and more events can be generated to overcome the statistical inefficiencies caused by negative weights. For a detailed review of the strengths and drawbacks of POWHEG and MC@NLO, see ref. [45].

In the following section, we will outline the MC@NLO method and show that the predictions it produces have the desired properties. We will then summarise some subtleties in the implementation of this method, in particular with regards to QED. We present test results from a hypothetical neutrino collider in sec. 3.3.1. In section 3.3.2 we present results for a QCD+QED MC@NLO for Higgs production via gluon fusion, where the EW corrections are effected to the Higgs decay to leptons. Finally, we conclude in sec. 3.4.

3.2 Methods

3.2.1 The MC@NLO method in detail

In this section we will show how, by applying a parton shower to a subset of an NLO calculation, we can generate a formula for the observable which reproduces its NLO value. This calculation follows the original MC@NLO paper, ref. [42]. We will begin by outlining the process symbolically, suppressing flavour sums, splitting indices, and phase space mappings. The latter are given in equations (1.2.3) and (1.2.4).

The expectation value of an IR-safe observable at NLO can be written, with subtraction terms D^S, as

$$\begin{aligned}\langle O\rangle^{\mathrm{NLO}} = &\int \mathrm{d}\Phi_n \left[B + \tilde{V} + I^S\right] O(\Phi_n) \\ &+ \int \mathrm{d}\Phi_{n+1} \left[R\, O(\Phi_{n+1}) - D^S\, O(\Phi_n)\right]. \end{aligned} \tag{3.2.1}$$

Before we can extend this to NLO plus parton shower (NLOPS) accuracy, it will be helpful to reformulate eq. (3.2.1) by adding and subtracting an additional set of

subtraction terms D^A, as

$$\langle O\rangle^{\mathrm{NLO}} = \int \mathrm{d}\Phi_n \, \bar{B}\, O(\Phi_n) + \int \mathrm{d}\Phi_{n+1} \left[R\, O(\Phi_{n+1}) - D^A\, O(\Phi_n)\right], \tag{3.2.2}$$

where we define a $\bar{B}$ term containing the Born and subtracted virtual terms, in addition to the finite combination of both subtraction terms $D^A - D^S$, i.e.

$$\bar{B} = B + \tilde{V} + I^S + \int \mathrm{d}\Phi_1 \left[D^A - D^S\right]. \tag{3.2.3}$$

As was argued in ref. [42], generating the R and D^A terms in eq. (3.2.2) independently results in double counting, so we combine them into a subtracted real ME squared, $R - D^A$, and separate out the observable dependence:

$$\begin{aligned}\langle O\rangle^{\mathrm{NLO}} = &\int \mathrm{d}\Phi_n \, \bar{B}\, O(\Phi_n) + \int \mathrm{d}\Phi_{n+1} \left[R - D^A\right] O(\Phi_{n+1}) \\ &+ \int \mathrm{d}\Phi_{n+1}\, D^A \left[O(\Phi_{n+1}) - O(\Phi_n)\right].\end{aligned} \tag{3.2.4}$$

We will see that the new subtraction terms D^A must capture the soft and collinear parts of the real emission, which should be exponentiated by the parton shower.

The parton shower factor $\mathcal{F}_n$ acting on an n-particle state contribution to an observable O can be written recursively as (eq. (2.2.34))

$$\mathcal{F}_n(\Phi_n, O) = \Delta_n(\mu_Q^2, t_c)\, O(\Phi_n) + \int \mathrm{d}\Phi_1 \, \Delta_n(\mu_Q^2, t)\, \mathcal{K}_n\, \mathcal{F}_{n+1}(\Phi_{n+1}, O), \tag{3.2.5}$$

where $\mathcal{K}_n$ are the splitting kernels and

$$\Delta_n(\mu_Q^2, t') = \exp\left(-\int_{t'}^{\mu_Q^2} \mathrm{d}\Phi_1 \mathcal{K}_n\right) \tag{3.2.6}$$

is the Sudakov form factor.

As an aside, note that throughout this section the phase space element $\mathrm{d}\Phi$ is written symbolically as a single integral. Practically, we write the single-particle phase space element $\mathrm{d}\Phi_1$ in terms of a quantity t with units of energy squared, a dimensionless variable z and the azimuthal angle ϕ. As in chapter 2, the phase space element is

given by

$$\mathrm{d}\Phi_1 = \frac{1}{16\pi^2}\,\mathrm{d}t\,\mathrm{d}z\frac{\mathrm{d}\phi}{2\pi}J(t,z,\phi), \tag{3.2.7}$$

where $J(t,z,\phi)$ is the Jacobian. The variable t was referred to as the parton shower evolution variable in chapter 2. The limits on the integral in the Sudakov form factor, eq. (3.2.6), refer to the integral over t for the given emission. t_c is the IR cutoff of the parton shower, and μ_Q^2 is the shower starting scale, sometimes called the resummation scale.

We would like to examine the effect of the parton shower on the NLO observable. We will do this by expanding the formulae in α, defining our observable O to be $\mathcal{O}(\alpha^m)$ at LO. First, we expand the Sudakov factor in α,

$$\Delta_n(\mu_Q^2,t) = 1 - \int \mathrm{d}\Phi_1\,\mathcal{K}_n + \mathcal{O}(\alpha^2), \tag{3.2.8}$$

and therefore the parton shower factor expands as

$$\begin{aligned}\mathcal{F}_n(\Phi_n,O) &= O(\Phi_n) - \int \mathrm{d}\Phi_1\,\mathcal{K}_n\,O(\Phi_n)\\ &\quad + \int \mathrm{d}\Phi_1\,\left(1-\int \mathrm{d}\Phi_1\,\mathcal{K}_n\right)\,\mathcal{K}_n\left[O(\Phi_{n+1}) - \int \mathrm{d}\Phi_1\,\mathcal{K}_{n+1}\,O(\Phi_{n+1}) + \dots\right]\\ &= O(\Phi_n) - \int \mathrm{d}\Phi_1\,\mathcal{K}_n\,O(\Phi_n) + \int \mathrm{d}\Phi_1\,\mathcal{K}_n\,O(\Phi_{n+1}) + \mathcal{O}(\alpha^2).\end{aligned} \tag{3.2.9}$$

To relate this to the NLO observable defined above, we let the splitting kernels be the newly-defined subtraction terms, $\mathcal{K}_n = D^A/B$. Then the parton shower is applied to eq. (3.2.4),

$$\langle O\rangle^{\mathrm{NLOPS}} = \int \mathrm{d}\Phi_n\,\bar{B}\,\mathcal{F}_n(\Phi_n,O) + \int \mathrm{d}\Phi_{n+1}\,\left[R - D^A\right]\mathcal{F}_{n+1}(\Phi_n,O). \tag{3.2.10}$$

Recalling that $\bar{B} = B + \mathcal{O}(\alpha^{m+1})$ and expanding in α, we obtain

$$\begin{aligned}\langle O\rangle^{\mathrm{NLOPS}} &= \int \mathrm{d}\Phi_n\,\bar{B}\,O(\Phi_n) + \int \mathrm{d}\Phi_{n+1}\,D^A\left[O(\Phi_{n+1}) - O(\Phi_n)\right]\\ &\quad + \int \mathrm{d}\Phi_{n+1}\,\left[R - D^A\right]O(\Phi_{n+1}) + \mathcal{O}(\alpha^{m+2}),\end{aligned} \tag{3.2.11}$$

i.e. the parton shower generates the third term of eq. (3.2.4). Eq. (3.2.11) is therefore accurate to NLO.

To obtain a clearer physical picture, we can expand the parton shower factor in eq. (3.2.10) in terms of its Sudakov factor $\bar{\Delta}^A$,

$$\langle O\rangle^{\text{NLOPS}} = \int \mathrm{d}\Phi_n\, \bar{B}\, \left[\bar{\Delta}^A\, O(\Phi_n) + \int \mathrm{d}\Phi_1\, \bar{\Delta}^A\, \frac{D^A}{B}\, O(\Phi_{n+1})\right] + \int \mathrm{d}\Phi_{n+1}\, \left[R - D^A\right] O(\Phi_{n+1}). \tag{3.2.12}$$

This is the main idea of the MC@NLO method. However, there are many subtleties, and to see these it will be important to include the splitting sums and indices which we have neglected so far. The Sudakov factor $\bar{\Delta}^A$, unlike the standard parton shower Sudakov factor, must be integrated over all phase space. It is given by

$$\bar{\Delta}^A(t') = \prod_{\widetilde{ij},\tilde{k}} \bar{\Delta}^A_{\widetilde{ij},\tilde{k}}(t'), \tag{3.2.13}$$

where

$$\bar{\Delta}^A_{\widetilde{ij},\tilde{k}}(t') = \exp\left(-\sum_f \int \mathrm{d}\Phi_1^{ij,k}\, \Theta(t_{ij,k} - t')\, S_{ij,k}\, \frac{D^A_{ij,k}}{B}\right). \tag{3.2.14}$$

$S_{ij,k}$ is a ratio of symmetry factors, explained in ref. [37], and we have also included the sum over flavours. This encodes whether QCD and/or QED subtraction terms are being considered. Eq. (3.2.12) is, more precisely,

$$\langle O\rangle^{\text{NLOPS}} = \sum_f \int \mathrm{d}\Phi_n\, \bar{B}\, \Big[\bar{\Delta}^A(t_c)\, O(\Phi_n) + \sum_{\widetilde{ij},\tilde{k}} \sum_f \int \mathrm{d}\Phi_1^{ij,k}\, \Theta(t_{ij,k} - t_c)\, S_{ij,k}\, \bar{\Delta}^A_{\widetilde{ij},\tilde{k}}(t)\, \frac{D^A_{ij,k}}{B}\, O(\Phi_{n+1})\Big] + \int \mathrm{d}\Phi_{n+1}\, \left[R - \sum_{ij,k} D^A\right] O(\Phi_{n+1}). \tag{3.2.15}$$

The Θ-functions ensure the uniqueness of the first emission and define a starting scale for the parton shower.

The MC@NLO method as implemented within SHERPA, referred to henceforth as the S–MC@NLO method, makes the choice $D^A_{ij,k} = D^S_{ij,k}\,\Theta(\mu_Q^2 - t_{ij,k})$. Modified versions of the CS subtraction terms are used both for the NLO subtraction and the parton shower evolution. While in QED the weighted veto algorithm (see sec. 2.2.3) is used

in the ordinary shower to deal with negative charge correlators, in the S–MC@NLO method it is needed even in QCD to deal with the exponentiation of subtraction terms which are negative due to subleading colour or spin effects. However, beyond the first emission, the usual spin-averaged and leading-colour shower can be used to generate further emissions. The S–MC@NLO method has the advantage that to generate the unresolved emission term proportional to $\bar{B}$, the parton shower kernels do not need to be integrated over the one-particle phase space. Integrating the remaining D^S is then easy since the I^S are known analytically.

In the next section we will briefly consider the implementation of the S–MC@NLO method. We will introduce terminology and discuss the modifications needed for a QED matching, and for mixed matching to NLO QCD+QED.

3.2.2 Implementation

In an event generator, to generate events according to the MC@NLO equation (3.2.15), we use eq. (3.2.10), shown in the previous section to be NLO accurate. A seed event is generated either using $\bar{B}$ (a so-called soft event or $\mathbb{S}$-event) or $R - D^A$ (a hard or $\mathbb{H}$-event). $\mathbb{S}$-events are passed to a one-step parton shower where the splitting kernels are either exactly equal to D^A/B, or are reweighted to this value using the weighted veto algorithm. An emission may or may not occur, generating the first and second terms of eq. (3.2.15) respectively. The event is then passed to the standard parton shower to generate further emissions, starting from the scale of any emission that occurred. If an $\mathbb{H}$-event is selected, it already has real-emission kinematics, and is thus passed directly to the standard shower. This generates the third term of eq. (3.2.15). For further details of the implementation of the MC@NLO method in SHERPA, see refs. [45, 59]. However, in this section we will discuss some of the implementation details which are relevant for QED.

Scale choice. The choice of scales in QED MC@NLO is relevant despite the slow running of α compared to that of α_s. As has been argued [45,95], a lack of phase-space

restrictions on the exponentiated (D^A) part of the real emission can lead to logarithmic contributions to MC@NLO of $\alpha \log^2(q^2/s)$, where q^2 is the virtuality of the emitter particle, instead of the correct parton shower contribution of $\alpha \log^2(q^2/\mu_F^2)$. This implies that where $\mu_F^2 \ll s$, a careful choice of scale is needed. The scale chosen must be soft- and collinear-safe, so the invariant mass of bare charged particles cannot be used to define the scale.

Electron PDF. The electron structure function and the full electron PDF both provide an obstacle to initial-state showers and MC@NLO, due to their divergent behaviour. Some techniques to control this behaviour have been described in section 2.5.1. These involve using a cutoff to produce an overestimate which can be used for shower evolution, and generating shower variables logarithmically to avoid the divergence. The under-production of hard collinear radiation when a cutoff is used can cause additional problems in MC@NLO compared to an LO parton shower, however. When the subtracted real correction is sizeable and negative, there is no room for an underestimate of the first shower emission, since the difference can become negative for observables which are LO in the first emission. Work is currently underway to minimise this issue.

Running α and EW input scheme. As described in sec. 2.3, external photons (whether produced in the hard interaction or by a QED parton shower) should couple with $\alpha(0)$. This is completely consistent with our matching procedure, since differences between definitions of α enter beyond NLO. Here we make the choice to use a running α for the $\mathcal{O}(\alpha^{m+1})$ parts of the NLO calculation and for further shower emissions, while using the G_μ scheme for the $\mathcal{O}(\alpha^m)$ parts. Specifically, however, we use the coupling $\alpha(0)$ for photon emissions, since the majority of emitted photons will become long-distance objects, and hence should have the appropriate long-distance coupling. Correcting the NLO calculation thus involves rescaling the virtual-Born interference term, the $D^A - D^S$ term, and the subtracted real correction with a

factor $\alpha(0)/\alpha_\mu \approx 0.96$.

3.3 Results

In this section, we will present results produced using the QED MC@NLO method for charged lepton final states. More work is needed to adapt the MC@NLO method for the case of an electron-positron collider due to the electron structure function, so here we will focus on validating the method for matching a final-state shower. To this end, we first use a test process $\nu_\mu\bar{\nu}_\mu \to e^+e^-$ at 91.2 GeV and 500 GeV, then in section 3.3.2 we will study the leptonic decays of a Higgs boson.

Throughout this section, we will compare the QED MC@NLO method with the LO QED parton shower and with the YFS soft-photon resummation. To produce the following results, SHERPA's PHOTONS module was used [17]. Exclusive N-photon final states are produced in the soft approximation using eikonal factors, and can be corrected either using collinear splitting functions or exact higher-order soft-subtracted MEs, if the latter are specifically implemented. While the YFS framework can incorporate higher-order corrections to any order, and NNLO QED corrections have been implemented in SHERPA [18], here we use the publicly available NLO EW corrections in PHOTONS for the resonance decays presented here. Note that in all cases the total cross section in the YFS prediction is not changed, and so the NLO K-factor is not present. Also, the extension of the YFS algorithm to charged particle pair production is included [1] (see chapter 4 for a detailed description of the YFS formalism and the extension). It is also important to note that in the YFS framework, all fermion masses must be taken into account to regulate the collinear divergences. The parton shower results presented here were also produced with finite lepton masses. The MC@NLO method can in principle also take into account all fermion masses. However, to aid in efficiency of calculating the virtual contributions, we have here set all fermion masses to zero in the NLO parts of the calculation. The resummation includes the lepton masses. For all results, AMEGIC was used for the

Born ME generation [80] and COMIX was used for the real-emission MEs [96]. The one-loop MEs for MC@NLO were provided by OPENLOOPS [97–100]. We use the G_μ EW input scheme for the Born ME calculation, and the running α scheme described in sec. 2.2.6 for the shower and the YFS resummation. The MC@NLO EW scheme is described in sec. 3.2.2.

3.3.1 Case study: $\nu_\mu\bar{\nu}_\mu \to e^+e^-$

As in chapter 2, we first isolate the QED MC@NLO from other parts of event generation by looking at a process $\nu_\mu\bar{\nu}_\mu \to e^+e^-$. In this section we will present results from this process on the Z pole (with a centre-of-mass energy of 91.2 GeV) in addition to at higher energy, $\sqrt{s} = 500$ GeV. In the latter case, where the invariant mass of the electron-positron pair (before any radiation) is far from the Z mass, the on-shell Z decay ME is not usually appropriate. Hence, the PHOTONS module used to produce the YFS prediction usually employs a collinearly-approximated NLO correction. This would reduce its formal accuracy to the same as the parton shower. However, it was observed that the collinearly-approximated correction to this process suffers from an overestimate of hard radiation, and does not reproduce the correct real-emission cross section to the desired accuracy. Therefore, we use the Z decay ME to describe the process at 500 GeV. This is justified here, since in this process the initial state completely factorises, there is no photon exchange diagram, and there are no three-vector-boson vertices.

The majority of the cross section for this process resides at $\sqrt{s} = 91.2$ GeV. The LO cross section is $\sigma_{\text{LO}} = 3950.30(2)$ pb and the NLO total cross section is $\sigma_{\text{NLO}} = 3985.1(3)$ pb resulting in a positive K-factor of 0.9%. At a centre-of-mass energy of 500 GeV, far above the Z pole, the Born cross section is much smaller, $\sigma_{\text{LO}} = 0.10524(1)$ pb, and there is a negative NLO K-factor of 7.6% since $\sigma_{\text{NLO}} = 0.972197(1)$ pb.

First, fig. 3.1 shows a comparison of our MC@NLO implementation with the QED

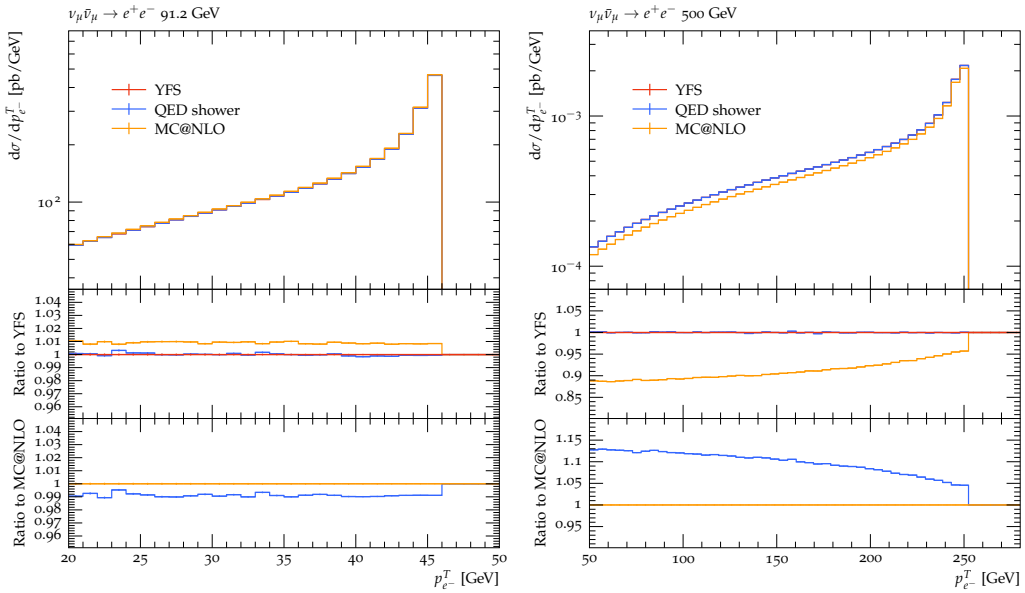

Figure 3.1: The electron transverse momentum in $\nu_\mu\bar{\nu}_\mu \to e^+e^-$, comparing the YFS soft-photon resummation with the LO QED shower prediction and the QED MC@NLO prediction for two different collider energies. **Left:** $\sqrt{s} = 91.2$ GeV. **Right:** $\sqrt{s} = 500$ GeV. The upper ratio plot shows the ratio to the YFS prediction while the lower shows the ratio of the LO QED shower to the QED MC@NLO prediction.

parton shower and with the YFS soft-photon resummation for the cross section differential in the electron transverse momentum. The left plot shows the electron k_T for a collider energy of $\sqrt{s} = 91.2$ GeV, while the right plot is for $\sqrt{s} = 500$ GeV. We see that the only difference between the methods for the process on the Z mass is the NLO K-factor describing the difference in the total cross section. For 500 GeV, on the other hand, there is a shape difference between the methods, with the MC@NLO producing comparatively more events with higher electron transverse momentum. Since this observable does not depend on real radiation except through small recoil effects, the YFS predictions only have LO accuracy here. In the NLO calculation, resonant structures are also present, for example due to resonant di-Z production in a box diagram, but these are very small and not visible here.

Fig. 3.2 shows an observable which is LO in the first emission, so here we expect to see significant shape differences between the four predictions. In this plot we show the cross section differential in the Durham $2 \to 3$ jet rate, produced by clustering

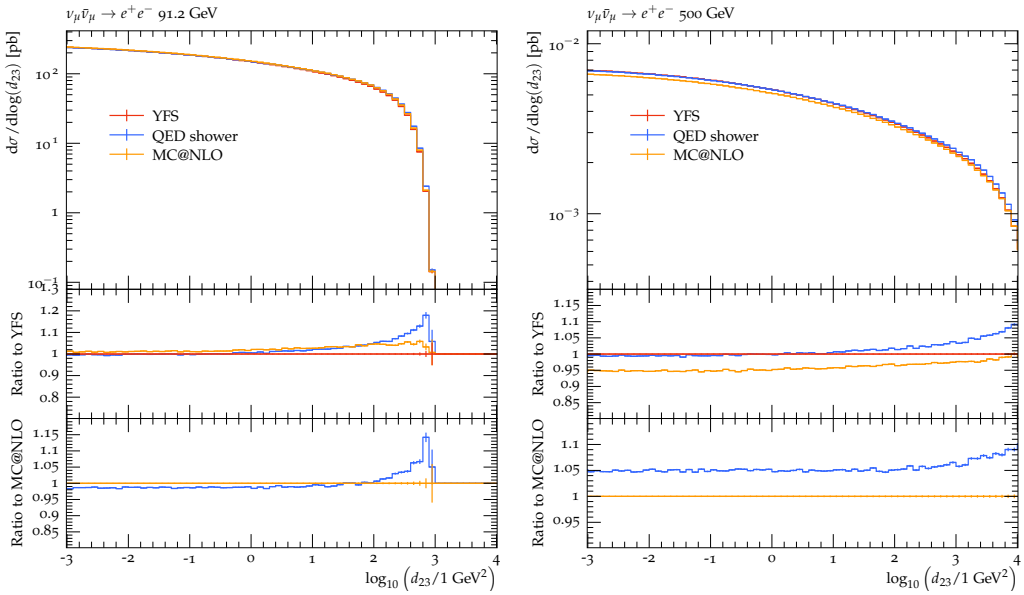

Figure 3.2: The 2-3 Durham jet rate in $\nu_\mu\bar{\nu}_\mu \to e^+e^-$, comparing the YFS method with the LO QED shower prediction and the QED MC@NLO prediction for two different collider energies. **Left:** $\sqrt{s} = 91.2$ GeV. **Right:** $\sqrt{s} = 500$ GeV. The upper ratio plot shows the ratio to the YFS prediction while the lower shows the ratio of the LO QED shower to the QED MC@NLO prediction.

QED particles with a k_T jet algorithm (for more details see sec. 2.4.1). We expect that the MC@NLO result should give the full real-emission cross section for hard emissions, and should tend to the shower-approximated result (multiplied by a K-factor) for soft or collinear emissions. Comparing the MC@NLO prediction with the YFS prediction (upper ratio plot), there is agreement to within a few percent at all scales, indicating that both predictions are NLO accurate. However, the MC@NLO approach produces slightly more hard radiation than the YFS method at both collider energies. Looking at the lower ratio plot, we can see that the MC@NLO corrects the overproduction of hard radiation that the LO shower suffers from.

Similarly, fig. 3.3 shows the third jet transverse momentum, produced using the same Durham jet algorithm. This observable has a strong probability of corresponding to the hardest photon transverse momentum, so we denote it k_T^γ. Again, for both centre-of-mass energies, both NLO-accurate predictions agree up to a K-factor. The shape differences caused by only including a collinear resummation, in the form of the QED

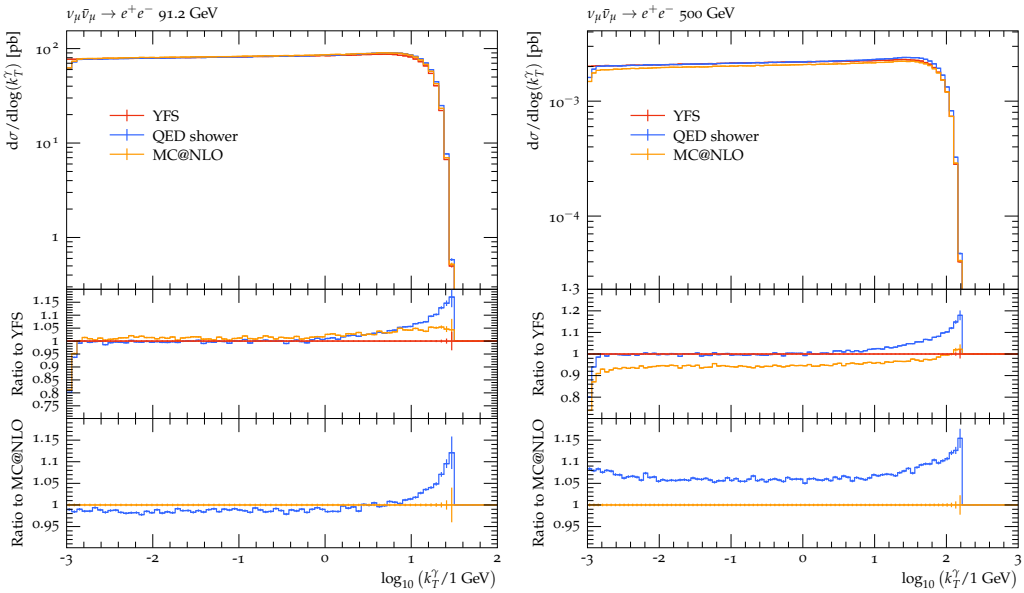

Figure 3.3: The third jet transverse momentum in $\nu_\mu\bar{\nu}_\mu \to e^+e^-$, comparing the YFS method with the LO QED shower prediction and the QED MC@NLO prediction for two different collider energies. **Left:** $\sqrt{s} = 91.2$ GeV. **Right:** $\sqrt{s} = 500$ GeV. The upper ratio plot shows the ratio to the YFS prediction while the lower shows the ratio of the LO QED shower to the QED MC@NLO prediction.

shower, are corrected by the MC@NLO method. It is clear that the MC@NLO method reproduces the correct shape across a wide range of photon transverse momenta. The advantage of the MC@NLO method over the matrix-element-corrected YFS resummation is that off-the-shelf NLO calculations can be used.

Fig. 3.4 shows the number of photons with $k_T \geq 1$ MeV produced by each method. The YFS resummation predicts a higher average number of photons per event, with the modal number of photons being 1, compared to the collinear resummation methods which do not produce a large number of soft photons, and retain a modal number of photons of 0. This difference is characteristic of the resummation method employed in each case. The YFS approach primarily resums soft logarithms, and collinear ones are only included through higher-order corrections, meaning that many soft photons are produced. On the other hand, the parton shower is derived from collinear resummation, and only includes the eikonal factors through modifications to the splitting functions.

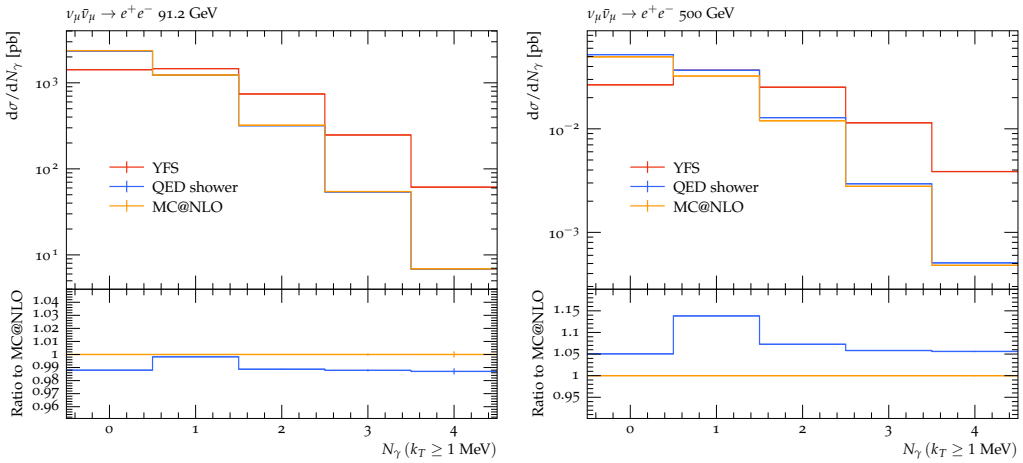

Figure 3.4: The multiplicity of photons with $k_T \geq 1$ MeV in $\nu_\mu\bar{\nu}_\mu \to e^+e^-$, comparing the YFS method with the LO QED shower prediction and the QED MC@NLO prediction for two different collider energies. **Left:** $\sqrt{s} = 91.2$ GeV. **Right:** $\sqrt{s} = 500$ GeV. The ratio plot shows the ratio of the LO QED shower to the QED MC@NLO prediction.

The fact that the two classes of resummation produce vastly different numbers of photons per event, but agree up to a few percent for physical inclusive distributions, validates the methods as viable alternative descriptions of the same physical process.

To verify this statement, we show the number of photons produced by each method, but with a higher k_T cut of 1 GeV, in fig. 3.5. It is immediately clear that the two classes of resummation methods produce similar numbers of hard photons. These will provide the bulk of the recoil effects, in addition to being more detectable experimentally. Differences in the zero-photon and one-photon bins still exist up to 15% at the Z mass and 25% at 500 GeV, but as we have seen from the d_{23} and third jet k_T plots above, the overall differences in the radiation pattern are much smaller than this. In particular, in the lower ratio plot comparing the shower and MC@NLO methods, we see that with this harder photon energy cut the MC@NLO method produces significantly more one-photon events than the shower. The 2-, 3- and 4-photon bins are unchanged compared to fig. 3.4, as expected.

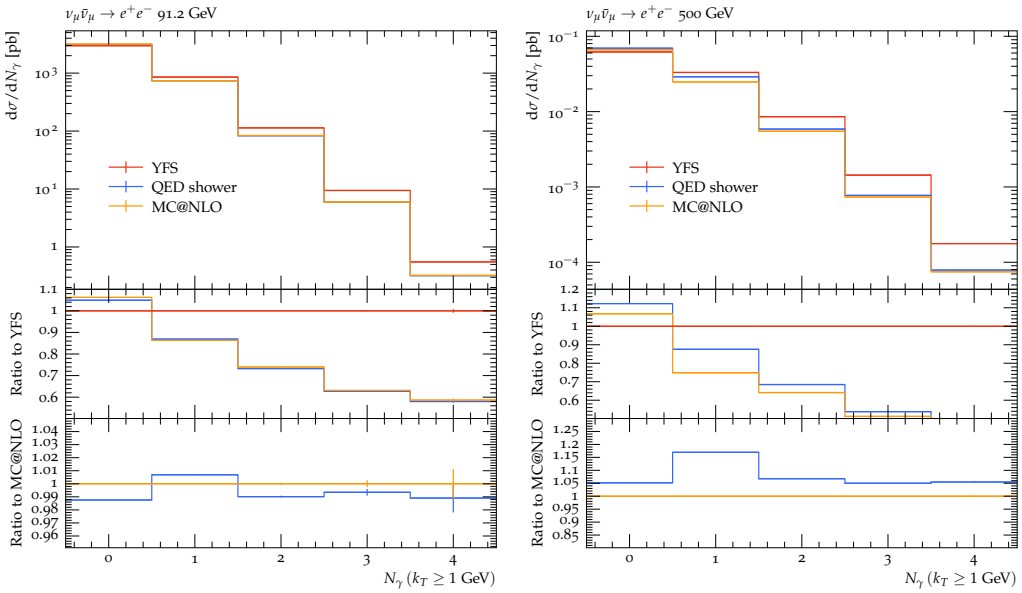

Figure 3.5: The multiplicity of photons with $k_T \geq 1$ GeV in $\nu_\mu\bar{\nu}_\mu \to e^+e^-$, comparing the YFS method with the LO QED shower prediction and the QED MC@NLO prediction for two different collider energies. **Left:** $\sqrt{s} = 91.2$ GeV. **Right:** $\sqrt{s} = 500$ GeV. The upper ratio plot shows the ratio to the YFS prediction while the lower shows the ratio of the LO QED shower to the QED MC@NLO prediction.

3.3.2 Leptonic Higgs decay

One of the primary use cases of NLO EW matching for the LHC is in Higgs decays to leptons, and their irreducible backgrounds in vector boson pair production. Recently the QCD+QED NLO matched corrections were presented for $pp \to VV'$ processes where the vector bosons decay leptonically [101]. However, the method presented is difficult to extend to Higgs decay processes due to POWHEG's exponentiation of large K-factors. Here we present the QCD+QED MC@NLO method, which has no such issue.

In this section, we will study the processes $gg \to H \to \mu^+\mu^-$ and $gg \to H \to e^+e^-\mu^+\mu^-$ in the HEFT. We will present a general method for automating the matching of an interleaved QCD+QED parton shower with the the NLO EW corrections to the Higgs decay and the NLO QCD corrections to the production process. We refer to these NLO corrections as NLO QCD+QED in the following. The method

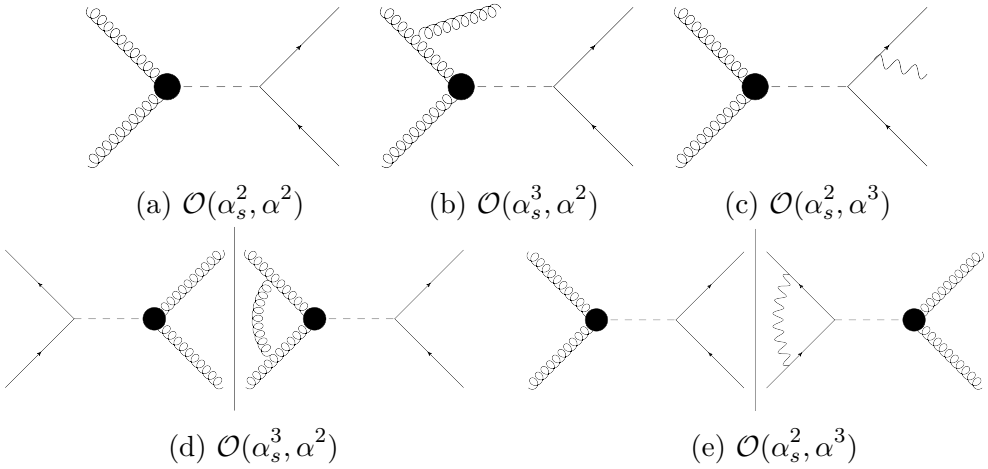

(a) $\mathcal{O}(\alpha_s^2, \alpha^2)$ (b) $\mathcal{O}(\alpha_s^3, \alpha^2)$ (c) $\mathcal{O}(\alpha_s^2, \alpha^3)$

(d) $\mathcal{O}(\alpha_s^3, \alpha^2)$ (e) $\mathcal{O}(\alpha_s^2, \alpha^3)$

Figure 3.6: A representative subset of the diagrams contributing at each order (labelled) of the NLO QCD+QED calculation of the process $gg \to \mu^+\mu^-$. Diagrams 3.6a, 3.6b and 3.6c are individually squared, while the virtual correction diagrams 3.6d and 3.6e are interfered with the Born process as shown.

is process-independent, but to aid in the explanation we will refer to these Higgs decay processes throughout. For clarity, a subsection of the diagrams included in the computation of $gg \to H \to \mu^+\mu^-$ are shown in fig. 3.6. Note that we do not include the mixed contribution, which enters at $\mathcal{O}(\alpha_s^3, \alpha^3)$. Similarly, for the four-lepton decay a selection of diagrams are shown in fig. 3.7. While diagram 3.7e emphasises that pure weak corrections are included at this order, the dominant virtual EW contribution will be from photonic vertex corrections to the Z decay.

The HEFT was introduced in section 2.4.2, but we will briefly recall it here since we now work at NLO QCD+QED. In the HEFT, we obtain a direct effective coupling of gluons to the Higgs,

$$\mathcal{L} = \mathcal{L}_{\text{SM}} + g_{\text{HEFT}}\, G_a^{\mu\nu} G^a_{\mu\nu} H + \ldots, \tag{3.3.1}$$

by integrating out the top quark in the SM loop-induced production of a Higgs via gluon fusion. Of course, other quarks can run in the loop, but since the top Yukawa coupling y_t is much greater than the other quark Yukawa couplings due to its large mass, other contributions can safely be ignored. Using this formalism, we neglect EW corrections to the top quark loop, which would be dominated by EW Sudakov

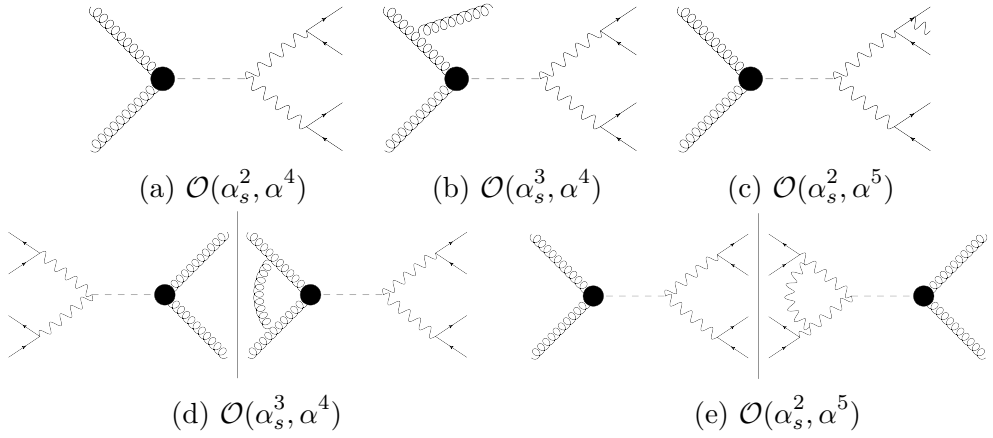

(a) $\mathcal{O}(\alpha_s^2, \alpha^4)$ (b) $\mathcal{O}(\alpha_s^3, \alpha^4)$ (c) $\mathcal{O}(\alpha_s^2, \alpha^5)$

(d) $\mathcal{O}(\alpha_s^3, \alpha^4)$ (e) $\mathcal{O}(\alpha_s^2, \alpha^5)$

Figure 3.7: A representative subset of the diagrams contributing at each order (labelled) of the NLO QCD+QED calculation of the process $gg \to \mu^+\mu^- e^+ e^-$. Diagrams 3.7a, 3.7b and 3.7c are individually squared, while the virtual correction diagrams 3.7d and 3.7e are interfered with the Born process as shown. While diagram 3.7e emphasises that pure weak corrections are included at this order, the dominant virtual EW contribution will be from photonic vertex corrections to the Z decay.

virtual high-energy logarithms (these have been implemented in various automated tools, *see* refs. [102–105]). In the diagrams in figs. 3.6 and 3.7, the ggH vertex is shown as a black blob, since it is not a SM vertex. In the SM, this effective coupling comes with a factor $g_s^2 y_t$. The numerical value of the ggH coupling used here is $g_{\text{HEFT}} \approx 5 \times 10^{-5}$.

Further to the discussion on the interleaved QCD+QED parton shower in section 2.4, we will briefly outline the MC@NLO procedure before presenting results.

The MC@NLO algorithm extends straightforwardly to match QCD+QED NLO in these processes. Separating QCD and QED contributions, eq. (3.2.15) becomes

$$\begin{aligned}\langle O \rangle^{\text{NLOPS}} = &\sum_f \int \mathrm{d}\Phi_n \left[\bar{B}\, \bar{\Delta}^A(t_c)\, O(\Phi_n) \right. \\ &\left. + \sum_{\widetilde{ij},\tilde{k}} \sum_f \int \mathrm{d}\Phi_1^{ij,k}\, \Theta(t_{ij,k} - t_c)\, S_{ij,k}\, \bar{\Delta}^A(t_{ij,k})\, \frac{D^A_{ij,k}}{B}\, O(\Phi_{n+1}) \right] \\ &+ \int \mathrm{d}\Phi_{n+1} \left[R_{\text{QCD}} + R_{\text{QED}} - \sum_{ij,k} \left(D^A_{\text{QCD}} + D^A_{\text{QED}} \right) \right] O(\Phi_{n+1}). \end{aligned} \tag{3.3.2}$$

The R_{QCD} and R_{QED} terms are given by the matrix element squared of the diagrams

in fig. 3.6b and 3.6c, respectively, and the equivalent diagrams where the gluon or photon is emitted from the other external leg, for the $gg \to \mu^+\mu^-$ process. For $gg \to \mu^+\mu^- e^+ e^-$, the diagrams 3.7b and 3.7c contribute. The $\bar{B}$ function is defined as

$$\begin{aligned}\bar{B} = B &+ \tilde{V}_{\mathrm{QCD}} + V_{\mathrm{EW}} + I^S_{\mathrm{QCD}} + I^S_{\mathrm{QED}} \\ &+ \int \mathrm{d}\Phi_1 \left[D^A_{\mathrm{QCD}} - D^S_{\mathrm{QCD}}\right] + \int \mathrm{d}\Phi_1 \left[D^A_{\mathrm{QED}} - D^S_{\mathrm{QED}}\right]. \end{aligned} \tag{3.3.3}$$

$\tilde{V}_{\mathrm{QCD}}$ contains the collinear mass factorisation terms from the initial state, in addition to the interference term shown in fig. 3.6d or 3.7d. V_{EW} contains the interference term, e.g. in fig. 3.6e or 3.7e. The shower kernel $D^A_{ij,k}/B$ and the Sudakov factor $\bar{\Delta}^A$ are generated in the usual way with an interleaved shower, and therefore contain both D^A_{QCD} and D^A_{QED}.

When an $\mathbb{H}$-event is selected, it is selected to be either QCD or QED according to the relative size of R_{QCD} and R_{QED}. If, as is the case here, the QED real emissions are of interest, the ME can be overweighted by a factor α_s/α so that QED real-emission events are selected as often as QCD real-emission events. A corrective weight is then applied as an analytic event weight. In a similar way, for $\mathbb{S}$-events an analytic overweighting can be applied to the QED splitting functions. The weights in this case must also be applied to the Sudakov factors when no emission occurs, as described in the weighted veto algorithm (section 2.2.3).

In this thesis, we are unable to present the full NLO QCD+QED corrections as described, due to current structural limitations of the process handling in SHERPA. Care must be taken when defining the different parts of a mixed NLO calculation to account for all the possible divergences which arise, especially for processes with four or more quarks at Born level. However, these results and considerations will be presented in a future publication. Here, to demonstrate the validity of the method, we present the pure EW NLO-matched parton shower, having already demonstrated the success of the interleaved QCD+QED evolution in chapter 2. We focus on distributions in invariant mass of final-state particles, since these are insensitive to

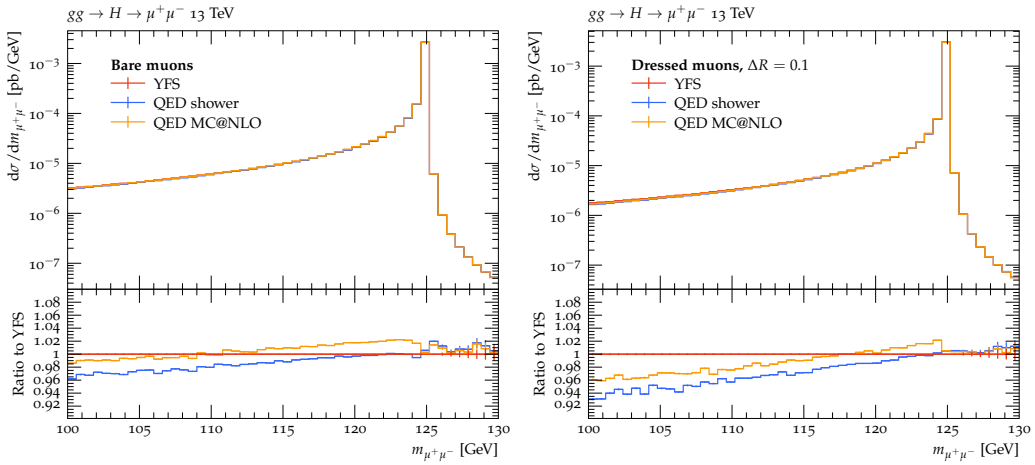

Figure 3.8: The dimuon invariant mass in the $gg \to \mu^+\mu^-$ process, comparing the QED MC@NLO with the YFS prediction and the QED shower. **Left:** bare muons, **Right:** photon-dressed muons with a cone size $\Delta R = 0.1$.

QCD radiation, and hence are NLO accurate up to a K-factor.

We consider gluon-induced Higgs production at the LHC, where the colliding protons have a centre-of-mass energy of 13 TeV. We use the PDF set PDF4LHC21 from the LHAPDF library [83]. Beam remnants, hadronisation, and multiple interactions were not modelled.

$gg \to H \to \mu^+\mu^-$

The LO cross section for $gg \to \mu^+\mu^-$ at the 13 TeV LHC in the HEFT is $\sigma_{\text{LO}} = 0.0028662(1)$ pb. The NLO EW cross section is $\sigma_{\text{NLO}} = 0.0028747(4)$ pb, which results in a positive EW K-factor of 0.3%. In this section we present the differential cross section in the muon invariant mass for bare muons and dressed muons. The muons are dressed with photons in a cone of radius $\Delta R = 0.1$, where $\Delta R = \sqrt{\Delta\eta^2 + \Delta\phi^2}$. The primary muons, whether bare or dressed, are subject to cuts on transverse momentum, $p_\mu^T > 10\,\text{GeV}$, and rapidity, $\left|y_\mu\right| < 2.5$. We compare the QED MC@NLO with the YFS soft-photon resummation supplemented with exact NLO corrections, in addition to the QED shower presented in the previous chapter.

Figure 3.8 shows the dimuon invariant mass in the $gg \to \mu^+\mu^-$ process. No QCD corrections to the initial state are effected, apart from the gluon PDF. We compare

our implementation of the QED MC@NLO with the QED shower described in the previous chapter, and with the YFS resummation. We can see that the YFS and MC@NLO approaches agree to within 2% for this observable when bare muons are used to reconstruct the Higgs, and to within 4% when dressed muons are used. This shows very good agreement, since this invariant mass distribution is approximately a δ-function at LO. The MC@NLO prediction clearly has the same shape as the parton shower prediction, but integrates to the total NLO cross section. Just below the Higgs mass, the MC@NLO prediction has an enhancement of 2% above the YFS prediction for both bare and dressed muons, though the differential cross section in the immediate vicinity of the resonance is in excellent agreement when dressed muons are used.

$gg \to H \to \mu^+\mu^- e^+ e^-$

The LO cross section for the rare process $gg \to \mu^+\mu^- e^+ e^-$ at the 13 TeV LHC in the HEFT is $\sigma_{\text{LO}} = 0.00085(2)$ pb. The NLO EW cross section is $\sigma_{\text{NLO}} = 0.0097(6)$ pb, resulting in a positive K-factor of 13%. To provide some context, the QCD K-factor of around a factor of 2 was one of the primary motivations for the development of matching methods. Here, we see that the EW corrections are also enhanced, and must be included at the level of precision of modern experiments.

In this section, we will present distributions in the four-lepton invariant mass $m_{4\ell}$, as well as invariant masses of Z bosons reconstructed via the primary electrons and muons. As before, the primary electrons and muons are subject to cuts on transverse momentum, $p_\ell^T > 10\,\text{GeV}$, and rapidity, $|y_\ell| < 2.5$. We compare the QED MC@NLO with the YFS soft-photon resummation supplemented with collinearly-approximated NLO corrections, in addition to the QED shower presented in the previous chapter.

Figure 3.9 shows the four-lepton invariant mass differential cross section. The main features of the lineshape are the Higgs resonance at 125 GeV and the two on-shell Z threshold at 180 GeV. The left plot shows the predictions for the invariant mass

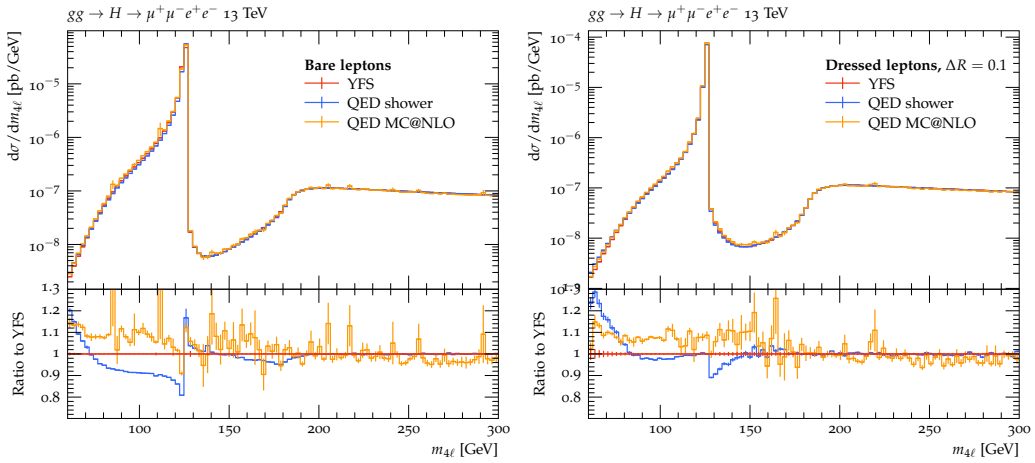

Figure 3.9: The four-lepton invariant mass in $gg \to \mu^+\mu^-e^+e^-$, comparing the QED MC@NLO with the YFS prediction and the QED shower. **Left:** bare leptons, **Right:** photon-dressed leptons with a cone size $\Delta R = 0.1$.

distribution reconstructed from bare leptons, while dressed leptons are used in the right plot. We use a cone dressing with a size $\Delta R = 0.1$ to recombine photons into primary leptons. Above the di-Z threshold, all three predictions are in excellent agreement. Between the resonance and the threshold, for bare leptons, the parton shower approach underestimates the cross section, while the YFS and the MC@NLO approaches agree up to statistical uncertainty. This feature is not present in the dressed lepton distribution. At the Higgs resonance, the MC@NLO shares the parton shower feature of roughly 15% more events on the resonance compared to just below it, compared to the YFS prediction. On the dressed level, the YFS and shower agree perfectly at the resonance, and the MC@NLO prediction has the same shape, but is modulated by the NLO cross section contribution in this region. At lower invariant masses, however, the MC@NLO calculation corrects the underproduction of events which the shower predicts, which is necessary for a good description of this process at the bare level. Overall, the MC@NLO and YFS predictions agree within a few percent. However, we can see in both plots that the MC@NLO suffers from worse statistics, since all dipoles are considered in the MC@NLO $\mathbb{S}$-events, and the same-sign dipoles result in negative weights. This is a motivation to include the OSSF dipole identification efficiency improvement, described in sec. 2.2.6, in the

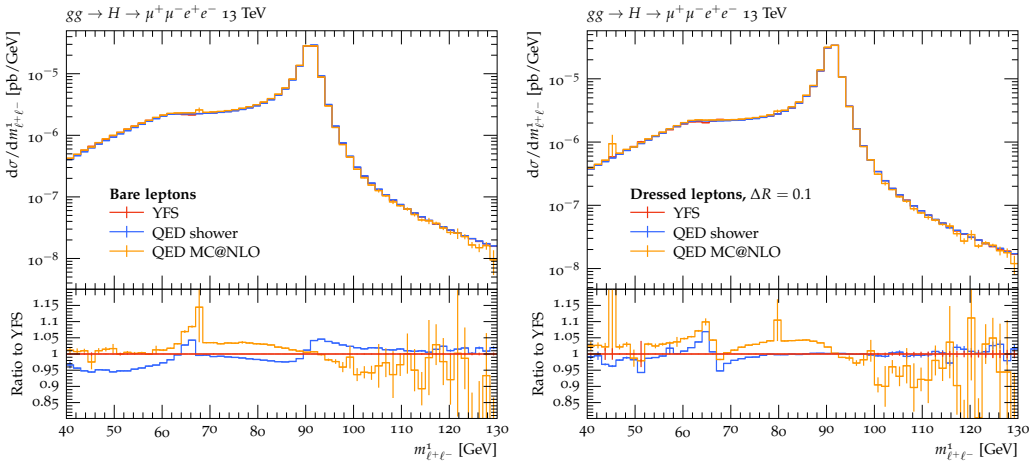

Figure 3.10: The hardest Z boson invariant mass in $gg \to \mu^+\mu^- e^+ e^-$, comparing QED MC@NLO with the YFS prediction and the QED shower. **Left:** bare leptons, **Right:** photon-dressed leptons with a cone size $\Delta R = 0.1$.

MC@NLO method. This would not impact the NLO accuracy of the simulation, and has been shown in sec. 2.4.2 not to impact the parton shower logarithmic accuracy.

We study two more invariant mass distributions, in figs. 3.10 and 3.11. Z bosons were reconstructed from the primary e^+e^- and $\mu^+\mu^-$ pair, identified by their energy. The left plots in both figures show the Z invariant mass reconstructed from bare leptons, while the right plots show the same observable using photon-dressed leptons with a cone size $\Delta R = 0.1$.

Fig. 3.10 shows the larger of the two Z invariant masses, comparing the QED MC@NLO prediction with the shower and the YFS predictions. We see that the shape is well-reproduced in all cases, with the two main features being a small local maximum at $m_H/2$, and a large peak at m_Z. Compared to the YFS prediction, the MC@NLO predicts an excess of events on the $m_H/2$ peak compared to just below it, amounting to differences of up to 10%. The MC@NLO prediction improves on the behaviour of the shower near the Z resonance for bare leptons, but for dressed leptons the main advantage of the MC@NLO method is the correct NLO cross section, mostly concentrated in the region 60-90 GeV.

On the other hand, fig. 3.11 shows the smaller of the Z invariant masses. We see

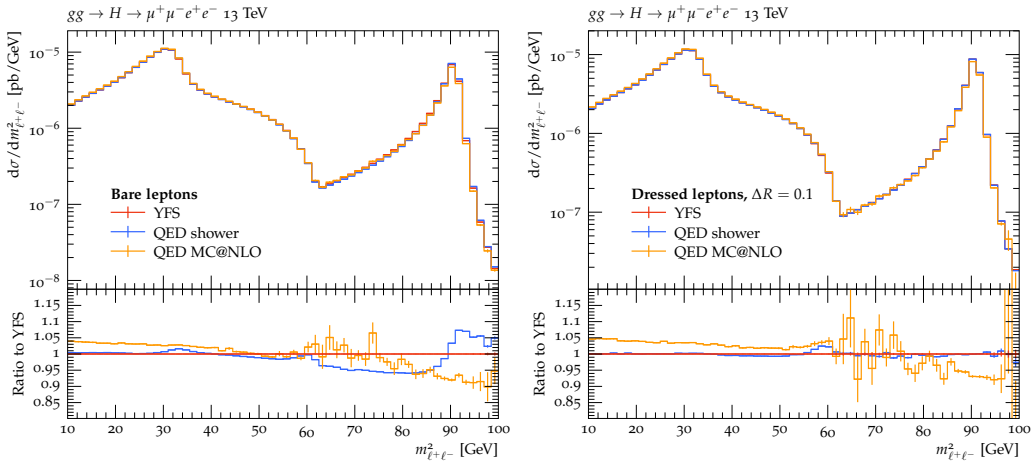

Figure 3.11: The second Z boson invariant mass in $gg \to \mu^+\mu^- e^+ e^-$, comparing QED MC@NLO with the YFS prediction and the QED shower. **Left:** bare leptons, **Right:** photon-dressed leptons with a cone size $\Delta R = 0.1$.

this time that the peak at $m_H/2$ is non-existent, though the Z resonance is still clearly visible, but that there is a peak at around 30 GeV. This is produced by an approximately on-shell Higgs decaying to an on-shell Z, leaving the other with the remaining 35 GeV invariant mass. We do not see a difference in the position of this peak for bare and dressed leptons, suggesting that any QED radiation effects are small in this region. In both plots, we see that compared to the YFS distribution, the MC@NLO prediction is skewed towards smaller Z invariant masses. This suggests that the leptons have lost more energy to photon radiation and secondary charged particles.

Overall, for the invariant mass distributions which are characterised by QED radiation in this process, the MC@NLO method produces distributions consistent with the YFS prediction at a level of a few percent, and the correct NLO cross section.

3.4 Conclusions

In this chapter we have presented novel results from a QCD+QED NLO matched parton shower. After arguing that the MC@NLO method is NLO-accurate and that it

extends to QED and mixed NLO corrections, we validated our implementation of the method using a test process $\nu_\mu\bar{\nu}_\mu \to e^+e^-$ at two different energies: just above the s-channel resonance, and far above it. We saw that the MC@NLO method performs well in both cases, producing results highly consistent with the widely used YFS soft-photon resummation in the former case. In the latter case, collinear logarithms play a larger role in the differential cross section determination, since the electron mass is comparatively smaller. The YFS approach only includes these logarithms at fixed order, while the MC@NLO includes the exact NLO result and the resummation of all orders of leading collinear logarithms. For this reason, we expect the MC@NLO method to provide a more accurate description at this energy.

We also demonstrated the applicability of our method to phenomenological studies. We studied the production of a Higgs boson via gluon fusion and its decay to two or four leptons. By matching the NLO QCD corrections to the production process to a QCD parton shower, and the NLO EW corrections to the decay to a final-state QED parton shower, we produced an NLO QCD+QED matched parton shower. As a first step, before the necessary process handling is available, we presented results from the NLO EW matched parton shower. We studied the Higgs lineshape and found large QED radiative corrections, as expected. These agreed well with the YFS predictions (with ME corrections). In addition, we studied the lineshapes of the intermediate Z bosons. We again found large QED corrections which were well-modelled by the matched shower. We found that an advantage of the MC@NLO approach is the freedom to use massless leptons in the ME calculation, while keeping the mass dependence in the resummed parts of the calculation. In this way, collinear logarithms are resummed without relying on small lepton masses to regularise them. This is an advantage since NLO calculations using massless fermions are more widely available than those with full mass dependence. We also studied the impact of lepton dressing on various invariant mass observables. We showed that dressed lepton observables have a reduced dependence on the radiative correction methods used, and hence a smaller theoretical uncertainty, than bare leptons.

Overall, our results show that in the precision era of particle physics, higher-order EW and QED corrections need to be included, and their accuracy quantified through the comparison of independent methods. Our implementation of the MC@NLO method allows a new class of methods to be explored, including future extensions of the method to electron-positron colliders. This would allow for another cross-check of predictions for the $e^+e^- \to$ hadrons cross section, which is a vital input to the calculation of $(g-2)_\mu$, through the determination of the hadronic vacuum polarisation.

The interleaved dipole shower and MC@NLO were implemented in the event generator SHERPA, and will be incorporated in a future release in the SHERPA 3 series. One-loop matrix elements were provided by OPENLOOPS [97–100]. All analyses and plots were made using RIVET [92, 93].

Chapter 4

Photon splitting corrections to YFS

4.1 Introduction

Precision measurements of the SM continue to stress-test our understanding of particle physics at an unprecedented level. In particular, charged and neutral Drell-Yan production at hadron colliders like the LHC are used as standard candles due to their large cross sections and exceedingly small experimental uncertainties, often below the percent level. However, these electroweak precision observables have also been brought to the forefront of searches for new physics, in the form of measured deviations from the SM prediction. For example, the recent extraction of the W boson mass, performed by the CDF experiment on legacy Tevatron data [106], is in apparent tension with the world average [107] and previous hadron and lepton collider measurements [108–125], as well as measurements of other fundamental EW parameters in Z production [126–135]. Measurements such as this motivate precise theoretical input with uncertainties in the permille range or lower. At this level of required accuracy, higher-order QCD and EW corrections in vector-boson production must be supplemented with additional sources of theoretical precision. In addition to a consideration of the structure functions that describe the make-up of the incident

particles, a detailed description of the vector boson's decay is paramount. Special emphasis must lie on the precise phase space distribution and flavour composition of the accompanying radiation, in order to be able to precisely model the detector response. With this chapter we contribute to the effort to determine the size and uncertainty of higher-order QED corrections in the description of the decay of massive vector bosons.

Higher-order corrections to Drell-Yan processes are known to NLO in the complete EW SM [136–145]. The recent advances at NNLO QCD-EW mixed calculations [146–155], though an impressive achievement in their own right, have not increased the perturbative accuracy of the description of EW or QED radiative corrections themselves. Alternatively, universal QED corrections can be resummed to all orders either in traditional QED parton showers by means of the DGLAP equation [156] (see chapter 2), or through the soft-photon resummation devised by Yennie, Frautschi, and Suura [13]. These resummations can of course be matched to the fixed-order calculations mentioned above (see chapter 3). As was described in chapter 2, a QED parton shower is available in all major general-purpose Monte-Carlo event generators: Herwig [157, 158], Pythia [159, 160], and Sherpa [32, 59, 161], while the YFS approach is implemented in Herwig [16] and Sherpa [17, 18] for particle decays. The implementation in Sherpa has recently been extended to also resum initial-state soft-photon radiation in e^+e^- collisions [86]. In addition, dedicated MC programs such as Photos [23–26] are widely used to add QED final-state radiation to any process.

To reach the necessary precision to make full use of the existing and future experimental datasets, the QED effects impacting the leptonic final state of the Drell-Yan process have to be understood in detail. These effects are driven by soft and collinear photon radiation. They can be resummed to all orders, and be further improved order by order in perturbation theory. Such calculations, matching to at least NLO EW corrections and sometimes even including NNLO QED ones, have been implemented using QED parton showers in Horace [63, 162–166] and Powheg [167–170],

using the structure function approach in RADY [142, 143], and through a YFS-type soft-photon resummation in WINHAC/ZINHAC [21], HERWIG [16] and SHERPA [17, 18]. In addition, the PHOTOS Monte-Carlo provides an algorithm based on both soft-photon resummation and ME corrections. Dedicated comparisons between SHERPA's YFS-type resummation and PHOTOS [171], between HORACE and PHOTOS [172], as well as HORACE and WINHAC [173] have yielded very good agreement.

A key element in the description of final state radiative corrections, however, has only been sporadically and not very systematically addressed: the possible splitting of the radiated bremsstrahlungs photons into secondary charged-particle pairs. These corrections only enter at a relative $\mathcal{O}(\alpha^2)$ in Drell-Yan processes, but the production of light flavours may be enhanced logarithmically and thus gain relevance. In addition, and in contrast to QCD, photons and light charged flavours like electrons, muons, or pions, are experimentally distinguishable – such conversions alter the visible make-up of the final state and are thus of importance at the envisaged theoretical precision. It is also important to consider here the usual experimental and phenomenological practice of dressing charged leptons with photon radiation. While definitions of QCD jets have been constantly refined, there has been little discussion of dressed lepton algorithms since the adoption of cone-dressing strategies where all photons within a certain radius of the lepton are absorbed. Considering higher-order corrections in the form of photons splitting into charged particles has the potential to spoil the physically meaningful definition of a lepton dressed with photons. The treatment of charged leptons in the presence of secondary charged flavours must therefore be handled with care. Thus, while a first implementation of pair-production corrections exists in PHOTOS [174, 175], it only covers photon splittings into electrons and muons, and their theoretical and phenomenological impact has not been rigorously appraised. In this chapter, we address this issue by introducing a rigorous independent framework to calculate these corrections and study the resulting theoretical and phenomenological implications.

This chapter proceeds as follows: We begin by providing a brief summary of the

YFS soft-photon resummation as implemented in SHERPA before providing a comprehensive description of the photon splitting implementation, including a detailed examination of their interplay and the splitting properties in sec. 4.2. We then present a detailed discussion of possible extensions of the standard lepton dressing algorithm to cope with the presence of secondary pairs of (light) charged particles, and quantify their effect on $Z \to e^+e^-$ decays in sec. 4.3. Finally, we offer some concluding remarks in sec. 4.5.

4.2 Soft-photon resummation and photon splittings

Incorporating photon-splitting processes alongside photon emissions are straightforwardly implemented when both are described in a common parton shower framework, as was discussed in chapter 2. In this chapter, however, we base our implementation on the existing and superior description of photon emission corrections in the YFS framework of the PHOTONS module in SHERPA [17], including its inherent coherent-radiation formulation and existing NNLO QED and NLO EW corrections [18]. In this section we thus start by providing a brief summary of the YFS soft-photon resummation and its implementation in the SHERPA event generator. The remainder of this section discusses the construction of the photon splitting algorithm in detail before examining its properties.

4.2.1 The YFS soft-photon resummation

The work of Yennie, Frautschi and Suura [13] describes the IR singularities of QED to all orders. To achieve this, the YFS approach considers all charged particles of the theory to be massive, and as a consequence only singularities associated with soft-photon emission are present. In particular, all photon splittings are finite and thus do not partake in the analysis of the IR singular structure. Using that knowledge,

the YFS algorithm reorders the perturbative expansion of a scattering or decay ME. This is achieved by separating the IR divergences from the finite remainders to all orders. The IR divergent terms form a series which can be exponentiated, amounting to a resummation of soft-photon logarithms in the enhanced real and virtual regions, leaving a perturbative expansion in IR-finite, hard photons (both real emissions and virtual exchanges).

In the implementation of the YFS resummation in SHERPA for particle decays [17], the all-orders soft-photon resummed differential decay rate is written as

$$\mathrm{d}\Gamma^{\mathrm{YFS}} = \mathrm{d}\Gamma_0 \cdot e^{\alpha Y(\omega_{\mathrm{cut}})} \cdot \sum_{n_\gamma=0}^{\infty} \frac{1}{n_\gamma!} \left[\prod_{i=1}^{n_\gamma} \mathrm{d}\Phi_{k_i} \cdot \alpha\, \tilde{S}(k_i)\, \Theta(k_i^0 - \omega_{\mathrm{cut}}) \cdot \mathcal{C} \right], \qquad (4.2.1)$$

wherein $\mathrm{d}\Gamma_0$ is the LO differential decay rate and the YFS form factor $Y(\omega_{\mathrm{cut}})$ contains the soft-photon logarithms. The decay rate is then summed over all possible additional photon emissions with an energy larger than ω_{cut} with respect to the LO decay. Each emission is described through its eikonal $\tilde{S}$ and corrected for hard emission effects up to a given order through the correction factor $\mathcal{C}$.[1]

Unlike a conventional parton shower, where the resummation is reliant on the factorisation of subsequent emissions when ordered in an evolution variable, YFS photons are unordered. They are also emitted coherently from the charged multipole through the radiator function $\tilde{S}$ and are thus not inherently associated with a specific emitter particle. Consequently, when the produced final state is to be further treated by a dedicated photon-splitting parton shower, the existing configuration must be interpreted in the parton shower's evolution and splitting language before any further splittings take place. Of course, care has to be taken so as to not compromise its LL soft-photon resummation. The effects of the algorithm we will describe in the following are completely beyond the scope of the YFS formulation without any potential overlap. Hence, this requirement amounts to ensuring the kinematic recoil induced by a splitting photon on the primary charged particle ensemble (and possibly other

[1] The hard (real and virtual) photon-emission corrections $\mathcal{C}$ are available up to NLO EW for leptonic W decays and up to NNLO QED + NLO EW for leptonic Z decays [18].

existing photons) vanishes in the limit that the energy of the splitting photon vanishes. While this is trivially true as all charged particles are treated as massive, the recoil assignment performed in this study and described in section 4.2.2 introduces corrections to the momenta of the primary charged particle ensemble which scale non-logarithmically with the photon energy and hence do not contribute to the LL resummation.

4.2.2 Photon splittings

In this section we introduce the parton shower algorithm which computes the photon splitting probabilities and kinematics, while the principal user input commands to steer its behaviour are described in appendix A. We will use the usual notation associated with a CS dipole shower. Since the YFS algorithm requires massive charged particles, it is necessary to include all masses in this shower for consistency. There are therefore no IR singularities associated with our photon splittings, since the collinear pole is regulated by the fermion and scalar masses. However, the aim is still to capture the correct behaviour in the quasi-collinear limit, accounting for the logarithmic enhancement for collinear splitting into light flavours. Throughout this section we will focus on configurations where all relevant particles are in the final state of the decay process, *i.e.* decays of neutral resonances. In section 4.4, we discuss the modifications needed to describe the decay of charged resonances.

The key part of the parton shower algorithm is, as usual, the veto algorithm (*see* sec. 2.2.3). This allows us to avoid the problem of analytically integrating the splitting functions, which are detailed below, by using an overestimate to evaluate the cumulative emission probability, and then vetoing emissions with a probability which corrects for the overestimate. The evolution begins at some starting scale t_{start} which is the highest possible scale for a splitting to take place; we postpone its exact definition to the end of this section. All splitting functions compete: a splitting scale is calculated for each possible combination of splitter, splitting products, and

spectator. Whichever splitting results in the highest splitting scale is selected. If the splitting is accepted (not vetoed), a new particle is created and the flavours and kinematics of existing particles are updated. The whole process is repeated, starting from the selected splitting scale, and iterated until some IR cutoff t_c is reached. This cutoff is needed to regulate the divergence of the splitting functions in the general case where these appear. For a QCD shower, a physical choice for the cutoff is the hadronisation scale, which is of $\mathcal{O}(1\,\text{GeV})$, well above Λ_{QCD} where QCD dynamics turn non-perturbative. For a QED shower, however, the splittings which do not involve quarks can evolve to arbitrarily low scales. In the algorithm presented here, which contains only splitting functions of photon emissions off charged scalars and fermions as well as of photons splitting into massive fermions or pseudo-scalar hadrons, the cutoff is dictated by the mass of the lightest fermion, i.e. $t_c = 4m_e^2$ or lower.

As stated earlier, in the case of a photon splitting to a fermion or scalar particle-antiparticle pair, there is no soft divergence. The collinear divergence present for massless splitting products is converted into a logarithmic collinear enhancement when masses are included; hence, lighter particles will have a larger contribution to photon splitting corrections. Here we include all possible splittings up to a mass cutoff of $2m_i \lesssim 1\,\text{GeV}$ in addition to τ pair production which, while rare, contributes to some observables through the decays to lighter leptons or hadrons. Since most splittings occur near or below the hadronisation scale, we consider hadrons, not quarks, to be the relevant QCD degrees of freedom. Using this mass cutoff, the hadrons which can be produced are the charged pions and kaons. They are pseudo-scalars, and their interaction with photons is modeled using point-like scalar QED, neglecting any substructure effects. We use the scalar splitting functions of ref. [39]. Depending on the experimental environment, the kaons and τ leptons might decay before hitting any detector. This can be handled within the usual (hadron) decay treatment available within the SHERPA framework [161, 176].

Splitting functions and spectator assignment. In the usual parton shower notation, we use the following dipole splitting functions [39, 44, 68]

$$\begin{aligned}
S_{s_{\widetilde{ij}}(\tilde{k})\to s_i\gamma_j(k)} &= S_{\bar{s}_{\widetilde{ij}}(\tilde{k})\to \bar{s}_i\gamma_j(k)} = -\mathbf{Q}^2_{\widetilde{ij}\tilde{k}}\,\alpha\left[\frac{2}{1-z+zy}-\frac{\tilde{v}_{\widetilde{ij},\tilde{k}}}{v_{ij,k}}\left(2+\frac{m_i^2}{p_ip_j}\right)\right]\\
S_{f_{\widetilde{ij}}(\tilde{k})\to f_i\gamma_j(k)} &= S_{\bar{f}_{\widetilde{ij}}(\tilde{k})\to \bar{f}_i\gamma_j(k)} = -\mathbf{Q}^2_{\widetilde{ij}\tilde{k}}\,\alpha\left[\frac{2}{1-z+zy}-\frac{\tilde{v}_{\widetilde{ij},\tilde{k}}}{v_{ij,k}}\left(1+z+\frac{m_i^2}{p_ip_j}\right)\right]\\
S_{\gamma_{\widetilde{ij}}(\tilde{k})\to s_i\bar{s}_j(k)} &= S_{\gamma_{\widetilde{ij}}(\tilde{k})\to f_i\bar{f}_j(k)} = -\mathbf{Q}^2_{\widetilde{ij}\tilde{k}}\,\alpha\left[1-2z(1-z)-z_+z_-\right],
\end{aligned} \tag{4.2.2}$$

for splittings involving the scalars s, fermions f, their antiparticles $\bar{s}$ and $\bar{f}$, and a photon γ, in terms of the splitting variable y and light-cone momentum fraction z. These are defined as

$$y=\frac{p_ip_j}{p_ip_j+p_ip_k+p_jp_k}\qquad\text{and}\qquad z=\frac{p_ip_k}{p_ip_k+p_jp_k}\,. \tag{4.2.3}$$

Further, m_i is the mass of the splitting product i, and z_- and z_+ are the phase space boundaries

$$z_\pm=\frac{2\mu_i^2+(1-\mu_i^2-\mu_j^2-\mu_k^2)\,y}{2(\mu_i^2+\mu_j^2+(1-\mu_i^2-\mu_j^2-\mu_k^2)\,y)}(1\pm v_{ij,i}\,v_{ij,k})\,, \tag{4.2.4}$$

where the dimensionless rescaled masses $\mu_i^2=m_i^2/Q^2$ are introduced for convenience, and $Q^2=(p_i+p_j+p_k)^2=(p_{\widetilde{ij}}+p_{\tilde{k}})^2$ is the invariant mass of the dipole. The relative velocities $\tilde{v}_{\widetilde{ij},\tilde{k}}$, $v_{ij,k}$, and $v_{ij,i}$ are given by

$$\begin{aligned}
\tilde{v}_{\widetilde{ij},\tilde{k}} &= \frac{\sqrt{\lambda(1,\mu^2_{\widetilde{ij}},\mu^2_{\tilde{k}})}}{1-\mu^2_{\widetilde{ij}}-\mu^2_{\tilde{k}}}\,,\\
v_{ij,i} &= \frac{\sqrt{(1-\mu_i^2-\mu_j^2-\mu_k^2)^2\,y^2-4\mu_i^2\mu_j^2}}{(1-\mu_i^2-\mu_j^2-\mu_k^2)\,y+2\mu_i^2}\,,\\
v_{ij,k} &= \frac{\sqrt{(2\mu_k^2+(1-\mu_i^2-\mu_j^2-\mu_k^2)(1-y))^2-4\mu_k^2}}{(1-\mu_i^2-\mu_j^2-\mu_k^2)(1-y)}\,.
\end{aligned} \tag{4.2.5}$$

Finally, the charge correlator $\mathbf{Q}^2_{\widetilde{ij}\tilde{k}}$ is defined in eq. (2.2.8), repeated here for convenience:

$$\mathbf{Q}^2_{\widetilde{ij}\tilde{k}} = \begin{cases} \frac{Q_{\widetilde{ij}} Q_{\tilde{k}} \theta_{\widetilde{ij}} \theta_{\tilde{k}}}{Q^2_{\widetilde{ij}}} & \widetilde{ij} \neq \gamma \\ \kappa_{\widetilde{ij}\tilde{k}} & \widetilde{ij} = \gamma \end{cases} \quad \text{with} \quad \sum_{\tilde{k} \neq \widetilde{ij}} \kappa_{\widetilde{ij}\tilde{k}} = -1 \quad \forall\, \widetilde{ij} = \gamma \,, \tag{4.2.6}$$

where the $Q_{\widetilde{ij}}$ and $Q_{\tilde{k}}$ are the charges of the splitter and spectator respectively and their $\theta_{\widetilde{ij}/\tilde{k}}$ are 1 (-1) if they are in the final (initial) state. The $\kappa_{\gamma\tilde{k}}$ must ensure that the splitting functions are appropriately normalised such that the correct IR limit is found, but are otherwise unconstrained. Here we choose

$$\kappa_{\gamma\tilde{k}} = -\frac{1}{\mathcal{N}_{\text{specs}}}, \tag{4.2.7}$$

where $\mathcal{N}_{\text{specs}}$ is the chosen number of possible spectators, *i.e.* we choose to weigh all selected spectators $\tilde{k}$ equally. The photon splittings themselves are free of soft divergences, hence the spectator is only needed for momentum conservation and, in principle, any other particle of the process may assume this role. In the present context, we consider all primary charged decay products as possible spectators of photon splittings as our default, but the choice to consider only the splitting photon's originator particle (as reconstructed, described below) has also been implemented, *see* appendix A. While the other present YFS photons and other neutral decay products as well as the decaying particle itself are all valid spectators, the two choices described above both guarantee that enough energy is available to allow photon splitting into heavier flavours to occur. Limiting the number of spectators also helps to reduce the computational complexity. For further photon radiation off the products of a photon splitting, the spectator assignment, and therefore the recoil, should be kept local in that system.

Evolution variable. For the evolution variable t used in the parton shower, the requirement of LL accuracy means that any choice which preserves $\mathrm{d}t/t$ is formally correct in the IR limit. We consider two variants, modified virtuality $\bar{q}^2$ and trans-

verse momentum k_T^2. We will usually refer to the modified virtuality simply as the virtuality, since as we see from the definition in eq. (4.2.8) below, for photon emitters the definitions coincide. The virtuality is defined in terms of the dipole invariant mass Q^2 and the masses of the emitter $m_{\widetilde{ij}}$, splitting products $m_{i/j}$, and spectator m_k. The modified virtuality is given by

$$\bar{q}^2 = (Q^2 - m_i^2 - m_j^2 - m_k^2)\, y + m_i^2 + m_j^2 - m_{\widetilde{ij}}^2 \,. \tag{4.2.8}$$

Specifically, for the two relevant cases this translates to

$$\bar{q}^2_{\mathrm{f}\to\mathrm{f}\gamma} = (Q^2 - m_\mathrm{f}^2 - m_k^2)\, y \tag{4.2.9}$$

for photon emissions, where the flavour f can either be a scalar s, fermion f, or their antiparticles $\bar{s}$ and $\bar{f}$, and

$$\bar{q}^2_{\gamma\to\mathrm{f}\bar{\mathrm{f}}} = (Q^2 - 2m_\mathrm{f}^2 - m_k^2)\, y + 2m_\mathrm{f}^2 \tag{4.2.10}$$

for photon splittings. We see that, as stated earlier, photon emissions are possible at arbitrarily low evolution scales while photon splittings can only occur if the virtuality exceeds the pair-production threshold. Likewise, the transverse momentum is given by

$$\mathrm{k}_\mathrm{T}^2 = (Q^2 - m_i^2 - m_j^2 - m_k^2)\, y\, z(1-z) - m_i^2\,(1-z)^2 - m_j^2\, z^2 \,. \tag{4.2.11}$$

This is the momentum generated in the splitting which is transverse to the plane defined by the emitter-spectator dipole. Again, for photon emissions this translates to

$$\mathrm{k}^2_{\mathrm{T}\,\mathrm{f}\to\mathrm{f}\gamma} = (Q^2 - m_\mathrm{f}^2 - m_k^2)\, y\, z(1-z) - m_\mathrm{f}^2\,(1-z)^2 \tag{4.2.12}$$

and to

$$\mathrm{k}^2_{\mathrm{T}\,\gamma\to\mathrm{f}\bar{\mathrm{f}}} = (Q^2 - 2m_\mathrm{f}^2 - m_k^2)\, y\, z(1-z) - m_\mathrm{f}^2\,(z^2 + (1-z)^2) \tag{4.2.13}$$

for photon splittings. As discussed, photon emissions are possible down to $\mathrm{k}_\mathrm{T}^2 = 0$, but in this case the photon-splitting threshold also lies at $\mathrm{k}_\mathrm{T}^2 = 0$. As a result,

the chosen IR cutoff t_c will induce a minimal $\mathrm{k_T}$, and thus a minimal opening angle, produced in the pair-creation process. The pair's virtuality $\bar{q}^2$ automatically introduces a pair-production threshold, making it a viable candidate for the ordering variable for photon emissions. In addition, the Brodsky-Lepage-Mackenzie (BLM) argument [177] states that since the only ultraviolet divergences in this process come from vacuum polarisation insertions in the photon propagator, the correct choice of scale to minimise higher-order corrections is the photon virtuality.

It can be seen that the relation

$$\frac{\mathrm{d}t}{t} = \frac{\mathrm{dk_T^2}}{\mathrm{k_T^2}} = \frac{\mathrm{d}\bar{q}^2}{\bar{q}^2} \tag{4.2.14}$$

holds, therefore both transverse momentum and virtuality are possible choices of evolution variable and no Jacobian is needed to translate between them.

Using these definitions, there are three well-motivated choices for the global evolution variable.

1. As in most QCD parton showers, $t = \mathrm{k_T^2}$ is a viable choice. In analogy to QCD, ordering photon emissions by transverse momentum results in the inclusion of charge coherence effects [178], but there is no particular motivation to use $t = \mathrm{k_T^2}$ as the evolution variable for photon splittings into charged-particle pairs.

2. Choosing $t = \bar{q}^2$ is an equally valid option. Due to the s-channel nature of photon splittings, the photon virtuality is expected to be a good ordering variable here, as outlined in the BLM approach to determining scales. In addition, the gluon virtuality is commonly used in QCD parton showers to describe the $g \to q\bar{q}$ splitting, as described in the PYTHIA manual [159]. But since it does not implement angular ordering natively, it is not expected to yield the best description of soft-photon emissions.

3. Following eq. (4.2.14), we are free to interpret the evolution variable differently in different splitting processes as long as $\mathrm{d}t/t$ is invariant. As our default, we

thus choose to interpret the evolution variable t as k_T^2 in photon emissions and as $\bar{q}^2$ in photon splittings. We will refer to this the "mixed scheme" in later sections.

All three choices are implemented, *see* appendix A, and some of their respective consequences will be explored in sec. 4.2.3.

Generation of splitting variables. While the evolution variable t is generated as usual in the veto algorithm, the light-cone momentum fraction z has to be generated within its allowed range $[z_-, z_+]$. The integration limits $z_\pm$ are defined in eq. (4.2.4), but in order to generate a Sudakov factor we work with the evolution variable t. We generate a trial emission using the integral of the overestimate of the splitting function, for which the z limits are necessary, but we do not yet know the value of the kinematic variable y (eq. (4.2.3)). Using a change of variables to replace y with the evolution parameter yields usable z ranges at this stage. Hence in the k_T ordered scheme, the z limits are [44]

$$z_{\pm,\mathrm{k}_\mathrm{T}} = \min/\max\left[\frac{1}{2}\left(1 \pm \sqrt{1 - \frac{4t_c}{Q^2}}\right),\, z_\pm\right]. \tag{4.2.15}$$

Note that the $z_\pm$ are not yet known, but can be overestimated by 0 and 1, respectively. The above expression thus gives an overestimate of the true phase space available. The number of splittings rejected as a result is very small, however, and does not have a large impact on the efficiency of the algorithm.

On the other hand, in the virtuality ordered scheme $\bar{q}^2$ has no z dependence. This means that y can be determined independently of the light-cone momentum fraction z as well, $y(t, z) = y(t)$, by solving eq. (4.2.8) for y. This implies that the z limits can be written as

$$z_{\pm,\bar{q}} = \min/\max\left[\frac{q^2 + m_i^2 - m_j^2}{2q^2}\right.$$

$$\times \left(1 \pm \sqrt{1 - \frac{4m_i^2 q^2}{\left(q^2 + m_i^2 - m_j^2\right)^2}} \sqrt{1 + \frac{4m_k^2 q^2}{\left(Q^2 - q^2 - m_k^2\right)^2}} \right), \; z_\pm \Bigg] \tag{4.2.16}$$

where $q^2 = \bar{q}^2 + m_{\widetilde{ij}}^2$. Again, however, it is only a small price in efficiency to use larger and simpler limits at the trial emission stage. In the results that follow, $z_{-,\bar{q}^2} = 0$ and $z_{+,\bar{q}^2} = 1$ have been used.

Kinematics. With the above definitions of the dipole variables y and z or, alternatively, with the evolution variable t and the splitting variable z, and the uniformly distributed azimuthal splitting angle ϕ, we can now build the kinematics of the splitting products i and j and the spectator k after the emission process. The new momenta are given by an inversion of the momentum maps of ref. [39], and in their construction we follow ref. [44]. In particular, for the final-final dipoles discussed here, they are given in sec. 3.1.1 eq. (49)–(58) of ref. [44]. Note that this redistribution of momenta is IR safe and does not spoil the LL accuracy of the YFS resummation, since it introduces non-logarithmic corrections only.

Starting conditions. Having defined the evolution and splitting variables as well as the splitting functions and kinematic mappings above, we now need to specify the initial conditions to fully define the algorithm. As the photon emissions are already generated by the YFS soft-photon resummation, the existing distribution has to be reinterpreted as if it was generated by our shower algorithm. Then, the missing photon-splitting corrections can be embedded into the existing calculation. By not allowing further photon-radiation off the primary charged-particle ensemble, double counting is avoided.

To determine the scale at which each existing photon has been produced, we calculate the emission probabilities according to the splitting functions $S_{f_{\widetilde{ij}}(\tilde{k}) \to f_i \gamma_j(k)}$ and $S_{s_{\widetilde{ij}}(\tilde{k}) \to s_i \gamma_j(k)}$, respectively, for every existing soft-photon γ_j. Therein, every primary charged particle (all existing charged particles of the process at the this stage) can act

as possible emitter $\widetilde{ij}$ or spectator $\tilde{k}$. One of those possible splitting functions is then selected either according to its probability $S_{\widetilde{ij}\tilde{k}\to ijk}/\sum_{\widetilde{ij}\tilde{k}} S$ (default), or by selecting the one with the largest splitting probability (*see* appendix A). Its reconstructed evolution variable t is then set as the starting scale $t_{\text{start},j}$ of the further evolution for photon γ_j. The above parton shower algorithm is then started at the largest of all photons' starting scale, $t_{\text{start}} = \max[t_{\text{start},j}]$, but each individual photon's evolution is only active for $t \leq t_{j,\text{start}}$.

4.2.3 Properties of the photon-splitting algorithm

Having the algorithm to calculate photon splitting probabilities at hand, we can now examine its properties and assess the consequences of the specific algorithmic choices discussed above. To be precise, we use the example of an on-shell Z boson decaying to an e^+e^- pair (maximising the number of radiated photons). Hence, as we are not in a collider environment, we use a spherical coordinate system to measure relative radial distances $\Delta\Theta$ in the following.

We begin by presenting a detailed look into the conditions under which the photons generated through the YFS soft-photon resummation split. As discussed, in a first step, the existing distribution of photons and primary emitters must be clustered in order to assign individual starting scales to the evolution of each photon. This assignment is of course dependent on the choice of evolution variable for photon emissions off charged particles as well as the choice of spectator scheme.

Fig. 4.1 shows the distribution of starting scales when the photon emissions are reconstructed with the inverse emission kernels. In the left plot, the ordering variable is interpreted as either a relative transverse momentum, $t = \mathrm{k}_\mathrm{T}^2$ (red) or a virtuality, $t = \bar{q}^2$ (blue). In the transverse momentum ordering scheme we observe an approximately logarithmic rise in the abundance of starting scales, starting at the kinematic limit of $\mathrm{k}_\mathrm{T}^2 \simeq \frac{1}{4} m_Z^2$. This reflects the photon spectrum produced by the soft-photon resummation. This logarithmic rise levels out at $\mathrm{k}_\mathrm{T}^2 \approx m_e^2$, formed

by the reconstructed k_T^2 of ultra-soft photons of the event. This plateau ends at the soft-photon cutoff $\omega^2_{IR,YFS}$ used in the soft-photon resummation. In contrast, in the virtuality ordering scheme we see that the majority of events have starting scales above 10^{-6} GeV. In both cases the characteristic scale at $t = m_e^2$ is induced by both the splitter and the spectator masses of the primary decay. The effect of the IR cutoff is straightforward in the $t = k_T^2$ case, as shown by the labelled black dashed line. In the $t = \bar{q}^2$ case the cutoff does not dictate the turning point of the frequency plot, but, indirectly, the point at which the frequency falls to zero. Due to normalisation this has the effect of increasing the frequency above the electron mass. This appears as a flattening off of the plot just above the electron mass squared, before the frequency falls towards zero at m_Z^2 independent of the IR cutoff. We note that in the mixed ordering scheme, which we choose as our default ordering variable scheme, $t_{start} = k^2_{T,start}$.

On its right-hand side, fig. 4.1 shows the distribution of starting scales $t_{start} = k_T^2$ when the reconstructed emission of a YFS photon from one of the final-state charged particles is chosen either probabilistically according to the relative sizes of the splitting functions (red, our default) or by simply choosing the more likely emitter (yellow, dashed). There is no significant difference between the two schemes. A very small difference occurs at the high t_{start} end. In the winner-takes-all scheme, large starting scales are less likely because the emitter with the largest splitting function is always chosen; the chosen emitter is the particle which results in a smaller starting scale, due to the soft divergence and collinear enhancement of the splitting functions.

Having established the starting conditions of the photons' evolution we can now examine their splitting process into pairs of charged particles, and the interplay of the choice of interpretation of the evolution variable in either splitting process. Therefore, fig. 4.2 depicts the correlation of the starting scale $t_{start,j}$ of a photon and the collinearity, or opening angle $\Delta\Theta_{pair}$, of its splitting products (mainly e^+e^- pairs), for all three different choices of interpretation of the evolution variable t: $\bar{q}^2$, k_T^2, or mixed. In the virtuality-ordered scheme where $t = \bar{q}^2$, photons can

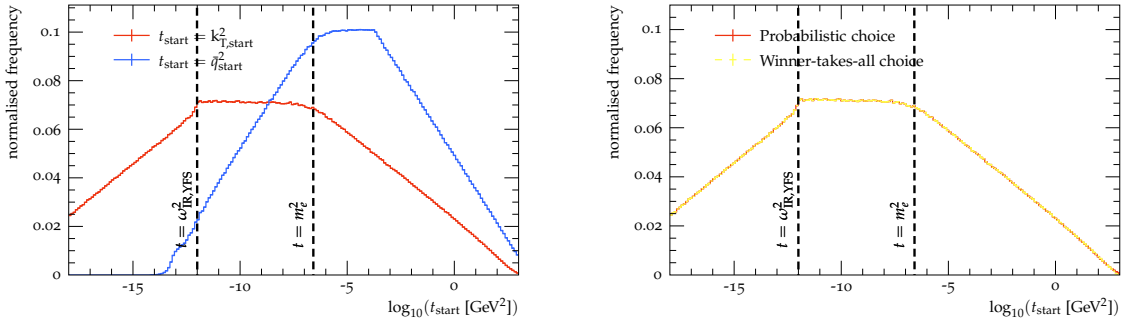

Figure 4.1: A comparison of the algorithmic choices made in reconstructing the initial $e^{\pm} \to e^{\pm}\gamma$ splitting generated by PHOTONS. **Left:** A comparison of the frequency of the reconstructed starting scales t_{start} using two choices for the evolution variable t, k_T^2 or $\bar{q}^2$, in the reconstructed initial $e^{\pm} \to e^{\pm}\gamma$ splitting. **Right:** A comparison of the frequency of the reconstructed starting scales $t_{\text{start}} = k^2_{T,\text{start}}$ using either a probabilistic determination of the emitter lepton or a winner-takes-all in the reconstructed initial $e^{\pm} \to e^{\pm}\gamma$ splitting. The threshold for photons splitting into charged particle pairs is $t > 4m_e^2$, and $\omega^2_{\text{IR,YFS}}$ is the IR cutoff of the YFS-style algorithm which generates the photons.

only split if t exceeds the pair-creation threshold of the lightest charged species, $t \geq 4\,m_e^2 \approx 10^{-6}\,\text{GeV}^2$. Furthermore, there is also a strong correlation between the starting scale of the evolution and the eventual splitting angle, which is mainly a consequence of the identification of the starting scale t_{start} for each photon. As already anticipated in section 4.2.2 above, the evolution scale in the k_T-ordered case is only constrained to be above the IR cutoff t_c, which is also chosen to be $t_c = 4\,m_e^2$ here. This constrains the opening angle of the pair of splitting products to be $\Delta\Theta_{\text{pair}} \gtrsim 10^{-4}$. The mixed scheme, in interpreting $t = k_T^2$ in reconstructing the photon emission to define t_{start} and $t = \bar{q}^2$ in photon splittings, combines aspects of these two schemes, producing a smooth distribution in the whole $(t_{\text{start}}, \Delta\Theta_{\text{pair}})$ space independent of t_c, as long as $t_c \leq 4\,m_e^2$. The opening angle becomes relevant when studying the recombination properties of the splitting product into a dressed primary charged particle, *see* sec. 4.3.1.

To further investigate the effects of our results on specific algorithmic choices, fig. 4.3

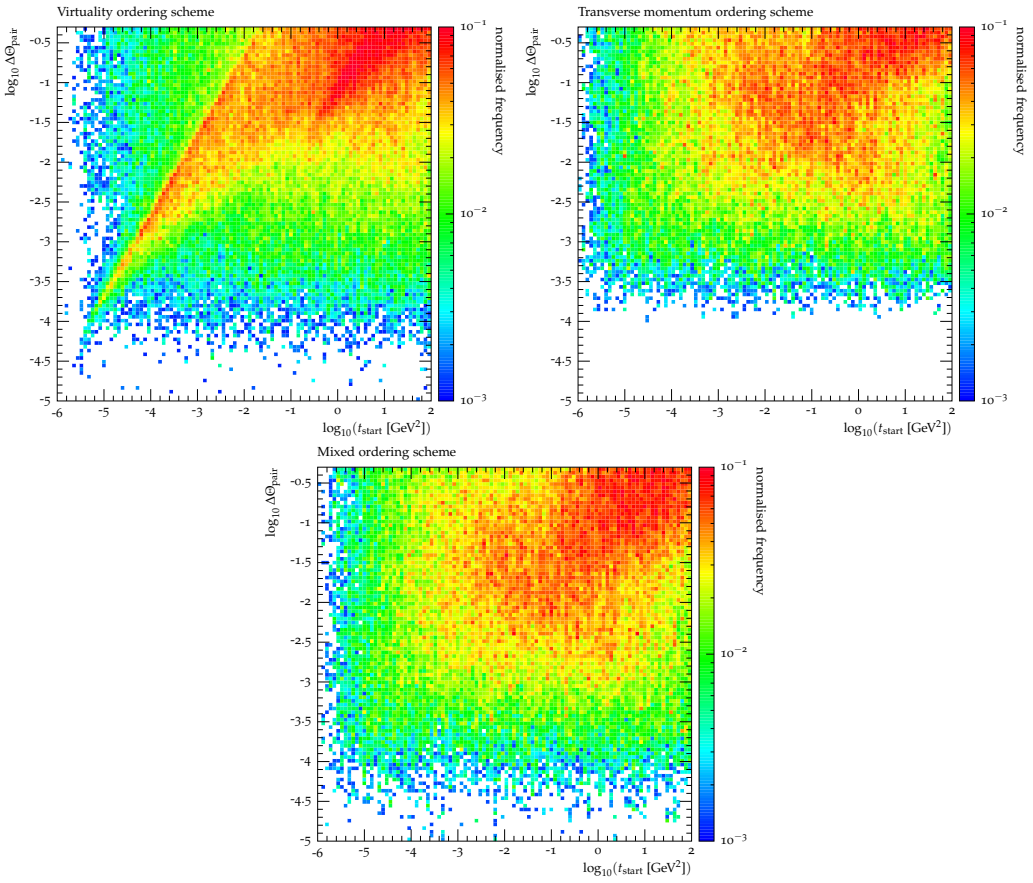

Figure 4.2: The interdependence of the starting scale t_{start} of a photon and the angular separation between the particles produced in its splitting, $\Delta\Theta_{\text{pair}}$, in the in the $\bar{q}$-ordered scheme (left), the k_T-ordered scheme (centre), and the mixed ordering scheme (right).

focuses on the same observable familiar from the previous figure: the interdependence of the starting scale t_{start} and the opening angle $\Delta\Theta_{\text{pair}}$. As in fig. 4.1, we see here that the effect of a winner-takes-all choice of starting scale as opposed to our default probabilistic starting scale definition is not significant. The winner-takes-all choice results in the distribution of starting scales being skewed to slightly smaller values, as discussed above, which correlates loosely with a more collinear splitting. This results in a slight extension of the high-frequency (red) region of the plot towards the small-t_{start} small-angle corner in the lower two plots of fig. 4.3 compared to the upper two plots. We also show the spectator scheme dependence in the photon splitting, i.e. whether we allow both primary leptons to be spectators, or only the lepton that the photon was reconstructed to have been emitted from. Since in photon splittings the spectator's only role is to absorb recoil to guarantee momentum conservation, it is physically well motivated for the splitting photon's progenitor to be the sole particle to absorb its gained virtuality necessary for the splitting process. Note that this choice does not affect the value of t_{start}, only the energy available in the splitting, which affects the overall splitting probability and the allowed opening angle of the splitting products. Fig. 4.3 shows that this choice has negligible effect on the distribution of splitting events in the $(t_{\text{start}}, \Delta\Theta_{\text{pair}})$ plane.

To conclude this section, fig. 4.4 shows the relative frequency of photons splitting into different species of charged lepton and hadron. As the driving factor is the produced particle species' mass, electron-positron pairs are most commonly produced, around an order of magnitude more commonly the products of photon splittings than muons or charged pions. The probability of producing a second pair of a given species roughly follows the naïve expectation of being the square of the probability of producing one pair. In a more detailed consideration one finds a factor of $\alpha^2 \log(m_Z/E_\gamma) \log(t_{\text{start}}/m^2)$ associated with each secondary pair production. Therein, E_γ is the energy of the bremsstrahlungs photon that subsequently splits into the pair of particles of mass m, and t_{start} is its reconstructed starting scale. Hence, we observe a single-logarithmic suppression of heavier flavours, modulo

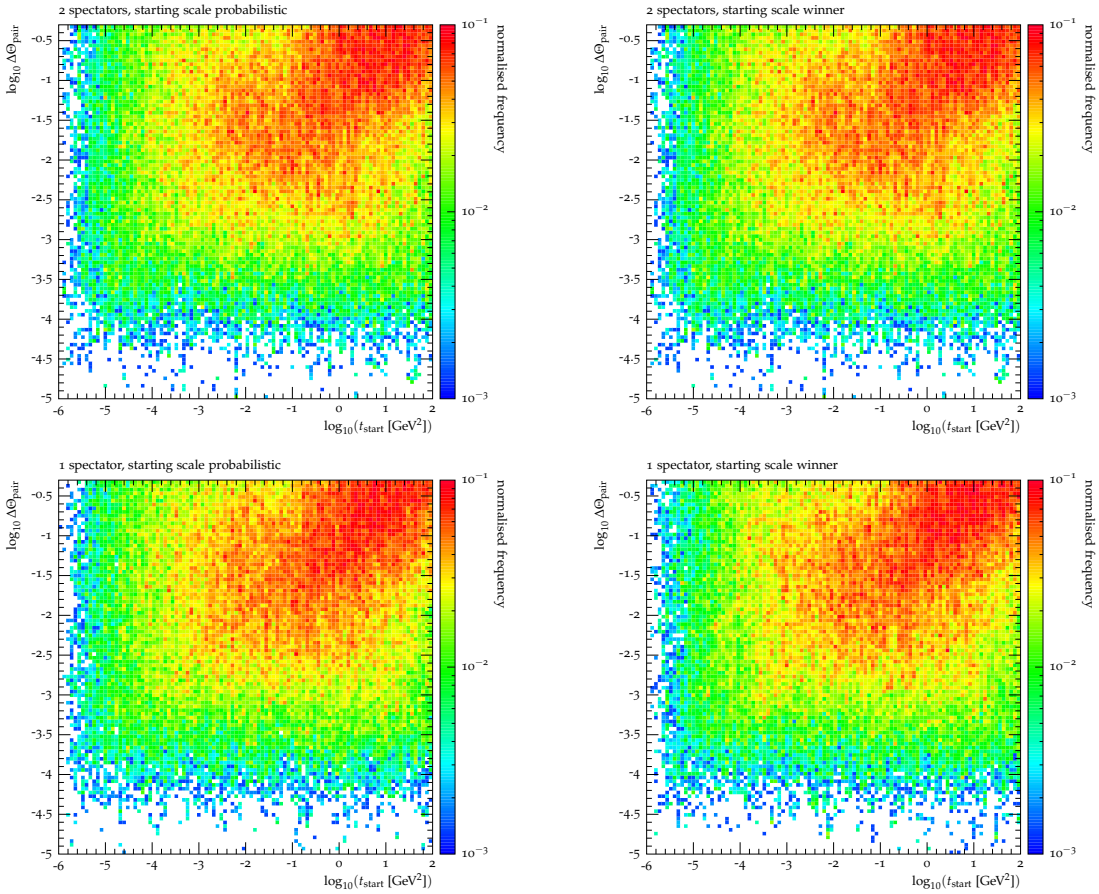

Figure 4.3: The interdependence of the starting scale t_{start} of a photon and the angular separation between the particles produced in its splitting, $\Delta\Theta_{\text{pair}}$, in the mixed ordering scheme with different choices of kinematic spectators of the photon splitting: both charged primary leptons (top row) or only the primary lepton the splitting photon was reconstructed to have been emitted from (bottom row). We also show the dependence on the way in which the starting scale of the evolution is chosen: probabilistically (left column) or by always choosing the winning dipole (right column).

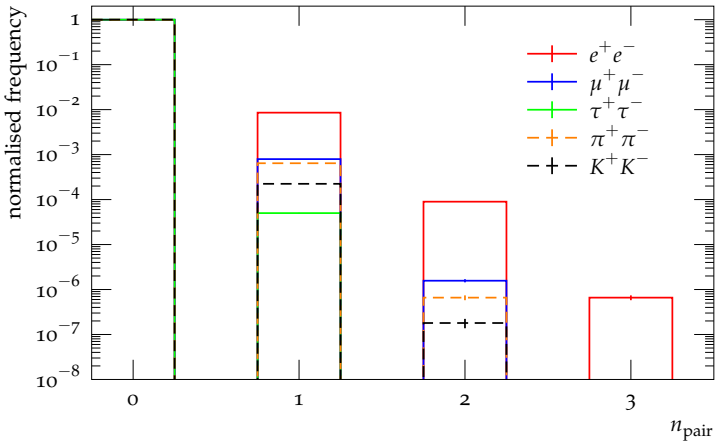

Figure 4.4: The relative abundance of secondary pairs of each species of charged particle produced in photon splittings in the mixed ordering scheme.

possible minor differences in the splitting function itself. This is well-reproduced by our algorithm. In fact, in the current example, the drop in frequency of producing an additional pair of particles of the same flavour is between 2.5 and 4.5 orders of magnitude.

4.3 Lepton dressing beyond photons

In this section we analyse the final states produced by our algorithm, and in particular the consequences of further resolving the photons produced by the standard soft-photon resummation into charged-particle pairs. We will continue to use the decay of an on-shell Z boson into an e^+e^- pair as a testbed for our algorithm. We will analyse the corrections induced by photon splittings on a number of physical properties that are related to the charged particle content of the radiation cloud surrounding the primary decay products.

We continue to use a spherical coordinate system to measure relative radial distances $\Delta\Theta$. Further, please note that for this study we turn off kaon and τ decays for the greatest accuracy in identifying primary final-state particles. By default, however, kaon and τ lepton decays would be handled as normal in SHERPA [161], including

various state-of-the-art parametrisations of all known decay channels and including their own respective QED corrections.

4.3.1 Dressing strategies in the presence of photon splittings

Lepton dressing is commonly used to define IR-safe observables through recombining a primary bare lepton with its surrounding radiation cloud, in analogy with the jet clustering of QCD. While lepton dressing is essential when massless leptons are used in a calculation due to the presence of collinear singularities, the inclusion of a lepton mass renders both dressed and bare lepton definitions physical. Nonetheless, bare leptons suffer from large corrections that are logarithmic in the lepton's mass, making them particularly relevant for electrons. Hence, a dressed lepton definition is also advantageous in calculations with massive, but light, leptons.

In practice there are two common methods for lepton dressing, analogous to jet definitions in QCD: cone dressing and sequential recombination dressing. While a sequential recombination algorithm typically uses either the anti-k_t or Cambridge-Aachen algorithm [179], the cone-based dressing uses the bare lepton to define the cone axis and, at variance with historical QCD cone algorithms, keeps the cone itself stable throughout the recombination procedure, rendering it collinear safe with respect to photon emissions. In either case, unlike in QCD, the algorithm is not completely blind to particle flavour since (at least) the primary bare lepton is used as the dressing initiator and defines the flavour of the resulting dressed lepton. As long as only photon radiation is considered as a higher-order correction to lepton production, which is the current standard in both YFS based soft-photon resummations [16, 17] and PHOTOS [24, 26], both algorithms work very straightforwardly by subsequently combining the primary lepton with the surrounding photon cloud using the respective distance measure.

When photon splittings are included in the QED corrections to lepton produc-

tion as well, the radiation cloud surrounding the primary lepton becomes flavour-diverse. Considering the underlying physical process, these photon-splitting corrections are simply resolving the structure of the photons constituting the above photon cloud. While these corrections are IR-finite when all lepton masses are considered, large logarithmic effects can be expected in particular when branching into the lightest species, electrons, occurs. Further, the splitting into electrons is the most probable branching for a photon emitter. Thus, while continuing to dress the primary leptons with photons only is IR-safe, it is natural to demand that the resulting dressed lepton definition does not strongly depend on whether or not we include further photon splittings. We will thus investigate the following choices for the flavour set $\mathrm{f}_{\mathrm{dress}}$ which is used to dress the primary lepton:

$\{\gamma\}$ We continue to use only photons to dress the primary charged lepton.

$\{\gamma, e\}$ In addition to the mandatory dressing with the surrounding photons, we also include the lightest charged particle, the electron, in the dressing procedure of the primary lepton. This is not only motivated by the fact that splittings into e^+e^- pairs give the largest corrections, but also that experimentally both electrons and photons are measured similarly in the calorimeter. Of course, the presence of a magnetic field between the interaction and the calorimeter does in principle decorrelate the direction of their respective momentum vectors.

$\{\gamma, e, \pi, K\}$ We also include the lightest hadronic splitting products in the dressed lepton definition. Such a definition is a compromise between theoretical inclusivity and experimental feasability.

$\{\gamma, e, \pi, K, \mu, \tau\}$ We include all species produced in our photon-splitting implementation in order to be completely inclusive. It has to be noted though, that in realistic experimental environments muons are well distinguishable even at low muon energies, and τ leptons of course decay further before detection rendering their inclusion in any realistic dressing algorithm highly non-trivial.

A schematic of how both the cone and sequential recombination dressing algorithms in the presence of photon splittings proceed is given in fig. 4.5. In the case of cone dressing, the primary leptons should be identified and dressed with all QED radiation that surrounds them, including other leptons and hadrons. In particular, the flavour of the dressed lepton does not change even if flavours other than a photon are included in it as it is determined entirely by the primary lepton. Thus, in consequence, the cone-dressed lepton may have a net charge that is different from that of its assigned flavour when not all photon-splitting products are recombined into the same dressed lepton. We will use this algorithm for the remainder of this study.

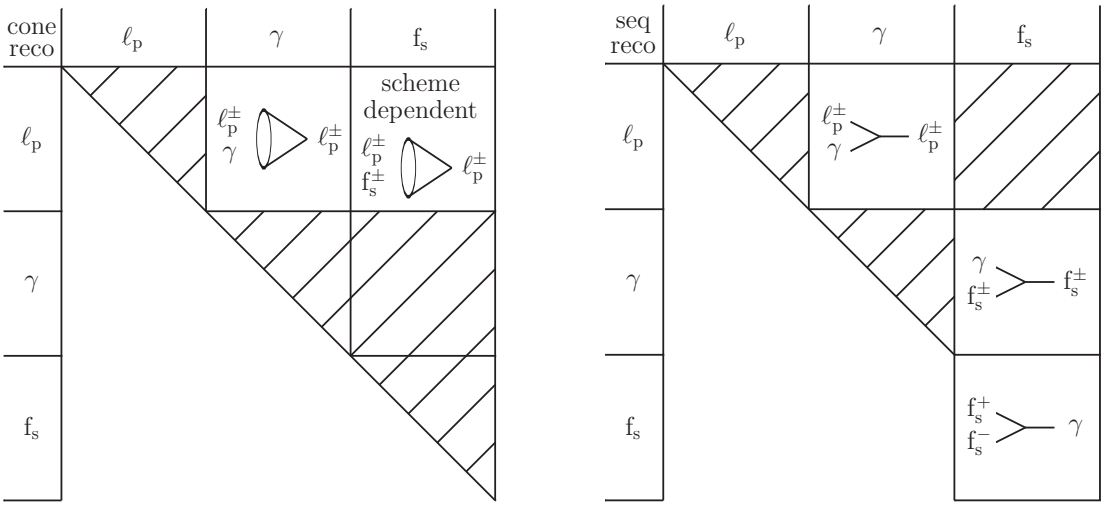

Figure 4.5: Recombination matrices of lepton dressing strategies beyond photon radiation. While γ labels the photon, ℓ_p and f_s denote the primary leptons and secondary flavours, respectively.

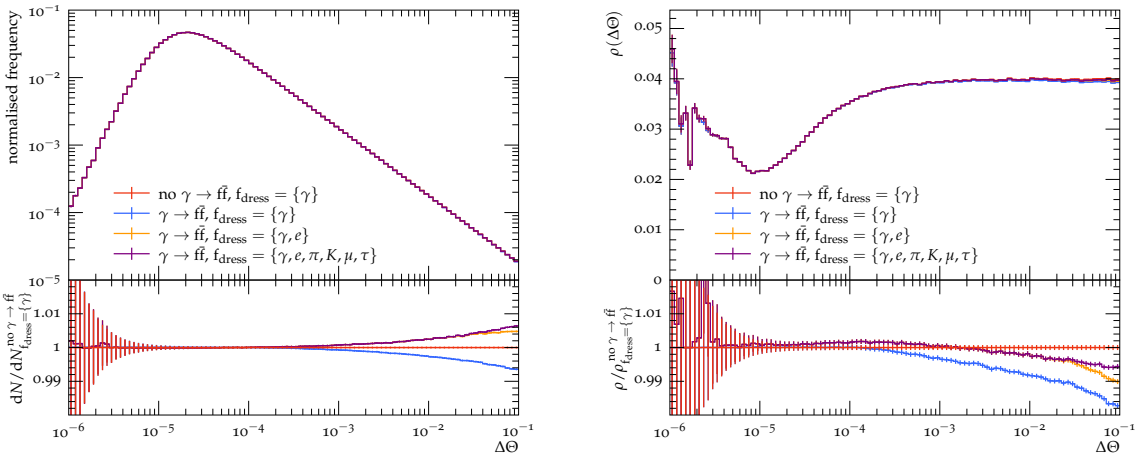

Figure 4.6: **Left:** The differential distribution of the dressed lepton constituents, including radiated photons having $E_\gamma > 0.1\,\mathrm{MeV}$, dependent on the angular distance $\Delta\Theta$ from the primary lepton. **Right:** The energy density ρ within the dressed lepton as a function of the angular distance $\Delta\Theta$ from the primary lepton. Shown are the predictions without accounting for photon splittings (red), compared to the predictions allowing photons to split: dressed with photons only (blue), photons and electrons (orange) or all particles (violet).

Nonetheless, a diagram of a flavour recombination matrix for sequential recombination dressing is shown on the right-hand side of fig. 4.5. Here it is possible to recombine a secondary (and hence soft/collinear) lepton-antilepton pair into a photon, while allowing for even softer or more collinear surrounding photons to be combined with these charged leptons first. On the level of primary leptons, then, they are only dressed with photons, either from the final state or from previous secondary-lepton clusterings. This has the obvious advantage that the charge and flavour of the primary lepton matches that of the dressed lepton. However, it is schematically more intricate and does not always yield circular dressed leptons, which are favoured experimentally. The investigation of sequential recombination dressing is left to a future study.

The first observables we examine offer closer looks into the substructure of the cone-dressed leptons produced by different dressing strategies. We introduce the legend notation: either photon splittings to charged flavours f are present ($\gamma \to f\bar{f}$) or they

are not (no $\gamma \to f\bar{f}$); the dressing algorithm is specified by the set of particle flavours f_{dress} which are included in the dressing.

The left-hand side plot of fig. 4.6 displays the angular distance $\Delta\Theta$ of the cone-dressed lepton constituent from the primary lepton. To ensure IR safety, only photons with $E_\gamma > 0.1\,\mathrm{MeV}$ are included. A cutoff just below the electron mass has been selected to ensure that all electrons are included in the analysis. Besides observing the primary lepton's dead cone for $\Delta\Theta \lesssim 2 \times 10^{-5}$, we find that for $\Delta\Theta \lesssim 10^{-4}$ the constituent multiplicity when including photon splittings, irrespective of the dressing scheme used, coincides with the multiplicity when omitting such splitting. This corroborates our earlier expectation that collinear photons largely lack the necessary virtuality to split into a charged-particle pair. At larger angles, where the required virtuality can be more easily gained, a photon's probability to split increases. In consequence, when including photon-splitting effects in the calculation, but not accounting for the splitting products in the dressing, a drop in multiplicity can be observed. Including electrons as well as photons in the dressing reincorporates most splitting products into the dressed lepton definition (*see* fig. 4.4). We find an increase above the reference of approximately the same number of constituents that are lost in the $\gamma \to f\bar{f}$, $f_{dress} = \{\gamma\}$ case. The completely flavour-inclusive dressing definition then shows the same effects scaled to the production of heavier secondary species: larger virtualities, and thus larger $\Delta\Theta$, are needed for a non-zero splitting probability, so fewer photons actually split into these heavier flavours. This leads to a much smaller effect of these splittings, concentrated at the outside of the cone. We expect out-of-cone effects to be small, since the frequency spectrum falls steeply towards the edge of the cone. More generally, it appears that the splitting products are close to collinear with the progenitor photon, at least on average.

On the other hand, the right-hand side plot of fig. 4.6 shows the distribution of energy within the dressed lepton as a fraction of the energy of the entire dressed lepton. Resolving photons into other species, *i.e.* pairs of charged particles, but continuing to dress the primary lepton with photons only naturally decreases the

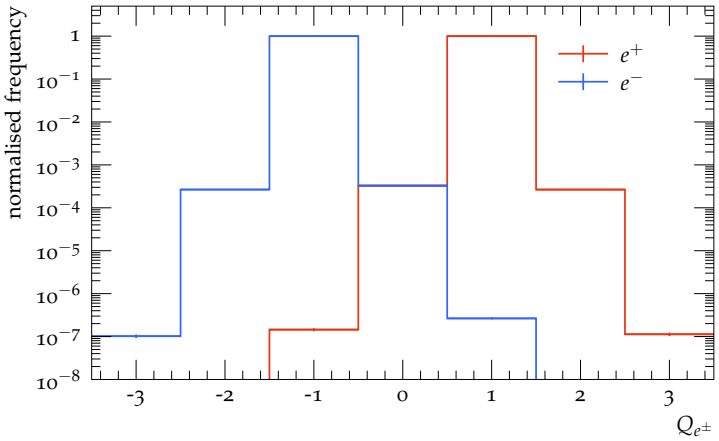

Figure 4.7: The total charge of the cone-dressed electron and positron with $\Delta\Theta_{\text{dress}} = 0.1$ and including all secondary flavours, *i.e.* $\text{f}_{\text{dress}} = \{\gamma, e, \pi, K, \mu, \tau\}$.

energy radial density of the dressed lepton. The fact that this energy density loss is not constant but rather increases with the radial distance to the primary lepton is again a result of the increasing possible off-shellness at larger $\Delta\Theta$, and therefore the increased splitting probability. Even when the photon splitting products are part of the dressing procedure (either secondary electrons only or the set $\{e, \pi, K, \mu, \tau\}$) the energy density ρ falls below the reference at some distance from the primary lepton, showing that a non-negligible number of more energetic splitting products end up outside the dressing cone radius.

As mentioned above, it is possible for the charge of the dressed lepton to be different from the charge of its primary constituent. This is shown in fig. 4.7 for the case of cone dressing with $\Delta\Theta_{\text{dress}} = 0.1$. Fewer than a thousandth of the dressed leptons are neutral or doubly charged, while a fraction of 10^{-7} of them are either triply charged or appear to be their own antiparticle (a dressed electron having a charge of $+1$ or a dressed positron having a charge of -1). Again, this is a consequence of only partially capturing the photon splitting products.

In the next section we will look at the separate and combined effects of photon splittings and flavour-aware lepton dressing on physical observables in the decay of an on-shell Z boson.

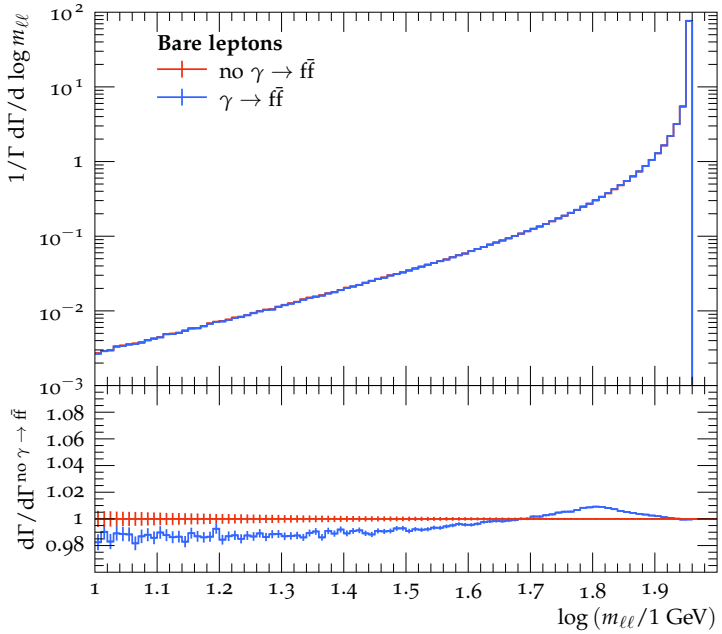

Figure 4.8: The bare dilepton invariant mass $m_{\ell\ell}$ in on-shell Z decay as described by the YFS soft-photon resummation only (red) or additionally resolving the photons further into pairs of charged particles (blue), in the mixed ordering scheme.

4.3.2 Case study: Z boson decay

Next, we look at the decay of an on-shell Z boson into an e^+e^- pair and investigate the impact of the photon splitting corrections introduced in this chapter on physical observables. To be precise, we present the effects of including $\gamma \to f\bar{f}$ splittings and the consequences of (not) using flavour-aware dressing algorithms on the decay rate, differential with respect to the invariant mass $m_{\ell\ell}$ of the primary electron-positron pair.

We begin by examining the bare differential decay rate, *i.e.* the invariant mass of the primary lepton pair that is not dressed with the radiation around it, in order to quantify the kinematic effect of photon splittings on the primary leptons themselves without confusing this effect with the intricacies of the dressing algorithm. We note that bare leptons are theoretically well-defined as all lepton masses are fully accounted for. To this end, fig. 4.8 isolates the effect of allowing YFS photons to split by presenting the bare invariant mass of the two most energetic leptons

of opposite charge, one electron and one positron. In the overwhelming majority of cases these are expected to be the primary electron-positron pair generated in the on-shell Z decay. The largest deviation from the pure YFS prediction without photon splittings, which is taken as the reference, is about 1% in the region of most interest. It occurs just below the Z mass, at about $60 - 70\,\text{GeV}$. It is driven by extracting additional momentum from the primary leptons to accommodate the necessary virtuality for photon splittings to occur. Although barely visible, this is fueled by a minute reduction of the much larger differential decay rate closer to the nominal Z mass itself. Although of less interest due to the smaller absolute decay rate, the opposite effect is seen at very small invariant masses, below 50 GeV. In this regime, through the same mechanism, the decay rate is diminished by about $1 - 2\%$ as the slope of the distribution is shallower but the momentum extraction is similar in magnitude to that at larger invariant masses.

Finally, a change of the precise definition of the ordering variable, both for the reconstructed starting scale of the evolution and the splitting scale of the eventual photon splitting, generally increases the size of the corrections for this observable. While using $t = \text{k}_\text{T}^2$ for all splittings only increases the observed corrections slightly, due to the increased photon splitting probability as $\text{k}_\text{T} < \bar{q}$ throughout, using $t = \bar{q}^2$ almost doubles the size of the corrections as now the starting scales of each photon's evolution reconstruct to much larger values, *see* fig. 4.1. This is a consequence of the different properties of these ordering variables as discussed in section 4.2.2, although *a priori* all choices have the same formal accuracy.

Having assessed the basic kinematic effects on the bare primary leptons, we now turn to dressed leptons. We will investigate the impact the different dressing strategies discussed in sec. 4.3.1 have, once the radiation cloud around the primary leptons is not comprised of only photons but is resolved further into various different flavours of secondary charged particles. To this end, fig. 4.9 contrasts the pure YFS soft-photon resummation without further photon splittings with a range of dressing strategies when photon splittings are included. Four different cone sizes are considered, from a

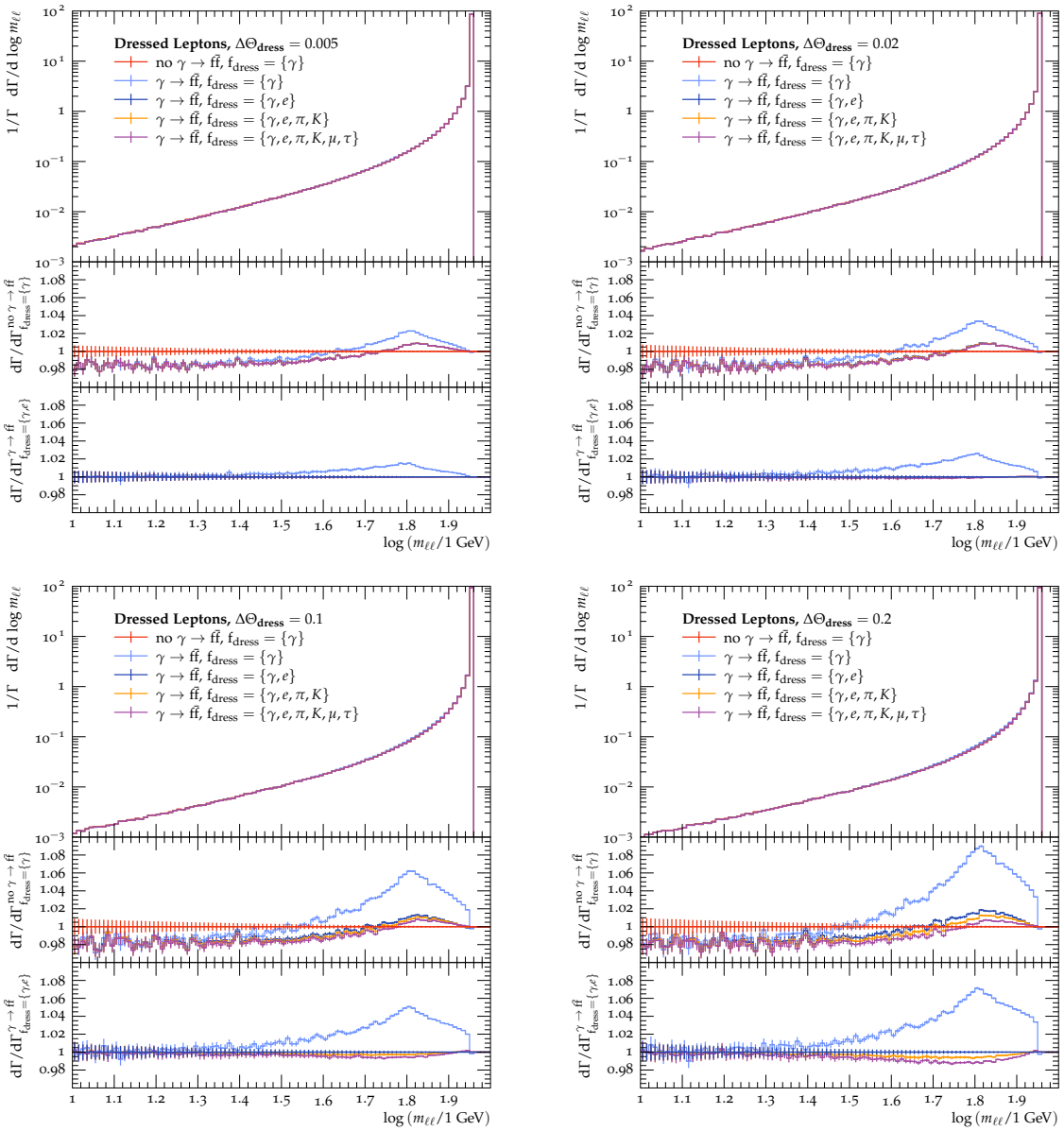

Figure 4.9: The dressed dilepton invariant mass $m_{\ell\ell}$ in on-shell Z decay as described by the YFS soft-photon resummation only (red) or additionally resolving the photons further into pairs of charged particles for four different dressing cone sizes, $\Delta\Theta_{\text{dress}} = 0.005$ (top left), 0.02 (top right), 0.1 (bottom left), and 0.2 (bottom right), in the mixed ordering scheme. We differentiate various different dressing strategies, recombining photons only (light blue), photons and electrons (dark blue), photons, electrons and charged hadrons (orange), and all charged particles (violet) within the dressing cone with the primary charged lepton. Two ratios are presented, either with reference to the soft-photon resummation without photon splittings (upper), or the soft-photon resummation including photon splittings and dressing the primary leptons with photons as well as secondary electrons (lower).

minimum $\Delta\Theta_{\text{dress}} = 0.005$ to a maximum $\Delta\Theta_{\text{dress}} = 0.2$. The upper ratio illustrates the deviation of each prediction from the pure YFS case, due to both the presence of photon splittings and the details of the dressing algorithm. The lower ratio isolates the effect of the dressing strategy by showing the deviation with respect to the photon-only-dressed events. In particular, this shows which secondary flavours are recombined with the primary lepton into the dressed lepton. We observe that when the photon radiation off the primary electrons is further resolved into charged-particle pairs but the primary electrons are still only dressed with only the photons of their surrounding radiation cloud, large effects are manifest. They range from slightly over 2% for $\Delta\Theta_{\text{dress}} = 0.005$ to 6% for the commonly used $\Delta\Theta_{\text{dress}} = 0.1$, and up to 9% for the more inclusive cone radius of $\Delta\Theta_{\text{dress}} = 0.2$. This difference originates in the fact that as long as only photons are included in the dressing, every photon lost by resolving it into a charged-particle pair cannot be recombined into the dressed lepton, which then ends up with less energy simply because higher-order corrections have been included. The observation that our algorithm reconstructs higher starting scales for hard wide-angle photons than either soft or collinear ones, and thus these are more likely to possess the necessary virtuality to split into charged-particle pairs, explains the dressing-cone-size dependence. However, when more inclusive dressing algorithms are considered, the effect of photon splittings on the differential decay rate is reduced, as is the $\Delta\Theta_{\text{dress}}$ dependence. As photons predominantly resolve into e^+e^- pairs, their inclusion in the dressed lepton definition already captures the bulk of the effect, in particular at smaller dressing cone radii. Along the lines of the above argument, photons need to be sufficiently separated from the primary lepton in order to gain enough virtuality to split into the heavier particle species. Thus, the inclusion of further secondary flavours in the dressing algorithm only plays a role at larger dressing cones, with effects ranging from 1% at $\Delta\Theta_{\text{dress}} = 0.1$ to 2% at $\Delta\Theta_{\text{dress}} = 0.2$. The effect of changing the ordering scheme for the photon splitting algorithm on fig. 4.9 is very similar to the effect on fig. 4.8. Again, using the transverse momentum or virtuality ordered schemes increases the size of the

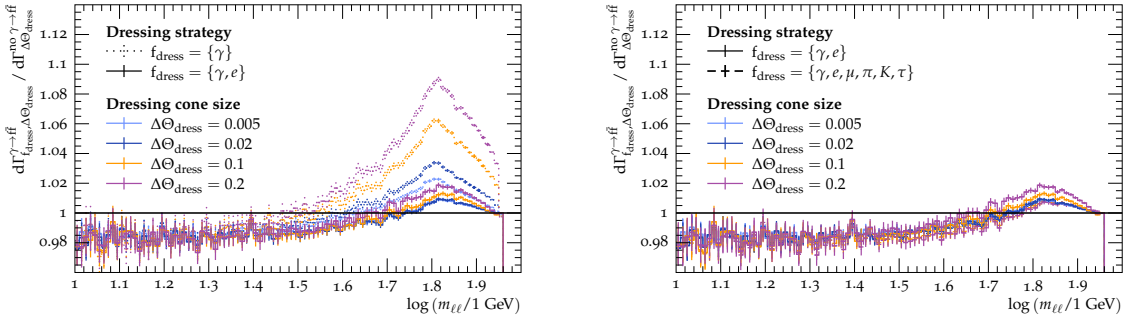

Figure 4.10: The cone size dependence of different dressing strategies in on-shell Z decay. The differential decay rate $\mathrm{d}\Gamma^{\gamma\to f\bar{f}}_{f_{dress},\Delta\Theta_{dress}}/\mathrm{d}\log m_{\ell\ell}$ has been divided by the corresponding $\mathrm{d}\Gamma^{\mathrm{no}\,\gamma\to f\bar{f}}_{\Delta\Theta_{dress}}/\mathrm{d}\log m_{\ell\ell}$, in dependence of both the flavour set f_{dress} included in the dressing and the dressing cone of size $\Delta\Theta_{dress}$. The **left** plot shows the difference case where only photons are used in the dressing (dotted) and using both photons and secondary electrons (solid), whereas the **right** plot shows the difference between a dressing strategy using only photons and electrons (solid) and all secondary flavours (dashed).

corrections induced by photon splittings in a very similar way as before. It is still the case that reincorporating splitting products in the dressing recovers the bare-lepton level deviation from the pure YFS prediction. As above, it needs to be noted that such a change in the ordering variable results in a suboptimal description of the physical process, and is thus not recommended to be used as an estimator of the intrinsic uncertainty.

In fig. 4.10 we show more clearly the recovery of the pure soft-photon prediction using the two most relevant charged-particle-inclusive dressing strategies. The figure shows the ratio of the differential cross section including photon splittings to that without photon splittings for different dressing choices. We find that including charged particles in the cone dressing limits the effect of photons splitting corrections to the 1% level, irrespective of cone size. Including electrons in the dressing similarly limits the corrections to 2% even for the largest cone sizes considered here.

4.3.3 Results: Drell-Yan production at hadron colliders

In this section we present results for the phenomenologically relevant case of Drell-Yan at proton-proton colliders. We focus on the process $pp \to e^+e^-$ at a centre-of-mass energy of 13 TeV. We use SHERPA's AHADIC for hadronisation and the PDF set PDF4LHC21 from the LHAPDF library [83]. These results were produced with a pre-release version of SHERPA 3.0. SHERPA's default parton shower, CSSHOWER, was used for the initial-state QCD shower [44]. COMIX was used for ME generation [96].

As before, the effect of photon splittings is seen most clearly in the dilepton invariant mass for a range of dressing strategies. In the hadron collider environment, it is clear that dressing leptons with light hadrons is not appropriate due to the large number of hadrons produced by unrelated QCD processes, such as initial-state radiation, multiple interactions and pile-up. As a result, in this section we focus on the modified cone dressing where secondary electrons are included in addition to photons.

Fig. 4.11 shows the dielectron invariant mass for bare electrons identified, as before, as the highest-energy opposite-flavour pair. Whilst for the case of on-shell Z decay the $m_{e^+e^-}$ spectrum was an LO observable in the QED radiative correction, in Drell-Yan production the spectrum is given at LO by the x distribution of the initial partons. The QED radiative corrections are large, however: they are around 50%. Hence we expect the photon splitting corrections to this observable to be much smaller than in the previous case study, but still non-negligible. This can be seen in the plot, where there is only a small region in which photon splitting corrections contribute a statistically significant correction. Below the Z peak, at an invariant mass of around 60 GeV, there is a positive correction of 0.5% to the cross section. While statistically significant on an event-generation level, the correction to this observable is not significant physically since scale-variation uncertainties in the spectrum are much larger than the MC statistical errors shown here. However, as before, these corrections are dependent on the lepton definition used in the observable.

To see this, we also investigate the effect of photon splitting corrections on dressed

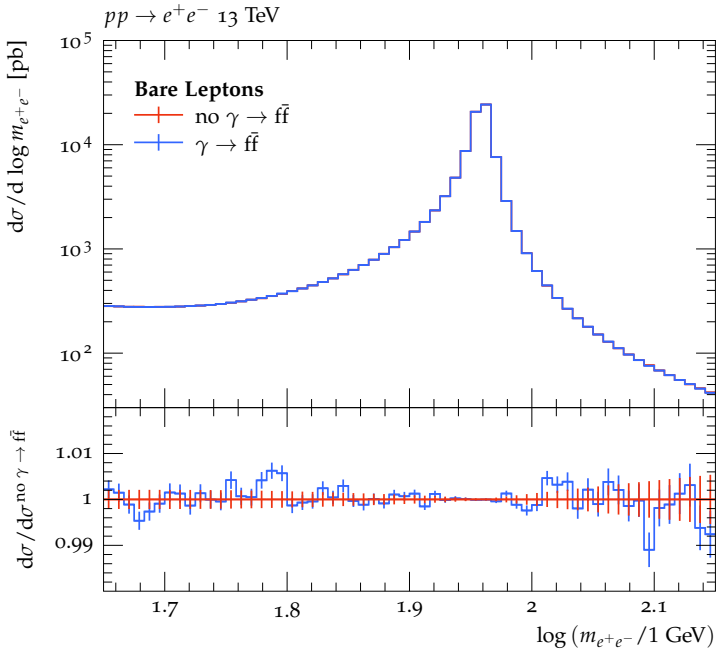

Figure 4.11: The bare dilepton invariant mass $m_{e^+e^-}$ in Drell-Yan production as described by the YFS soft-photon resummation only (red) or additionally resolving the photons further into pairs of charged particles (blue), in the mixed ordering scheme.

leptons. fig. 4.12 shows the dressed-electron invariant mass for a dressing cone size of $\Delta R_{\text{dress}} = 0.1$. We compare the usual photon-dressed electrons with those where secondary electrons have also been included in the dressing. The upper ratio plot shows the deviation with respect to the case where no photon splittings have been included. There is a clear 1% correction in a large kinematical region below the Z peak introduced by including $\gamma \to f\bar{f}$. However, as in the previous section, we see that this deviation is almost eliminated when secondary electrons are recombined into primary electrons in dressing cones. The lower ratio plot shows more clearly the effect of changing the dressing algorithm. These results echo the findings from the Z decay case study in a realistic collider environment.

In this section we have demonstrated the effectiveness of the proposed photon-splitting algorithm in modelling higher-order QED radiation in Z decays, including in neutral-current Drell-Yan processes. Before concluding this chapter, we briefly discuss the modifications to the algorithm in order to model corrections to W decays.

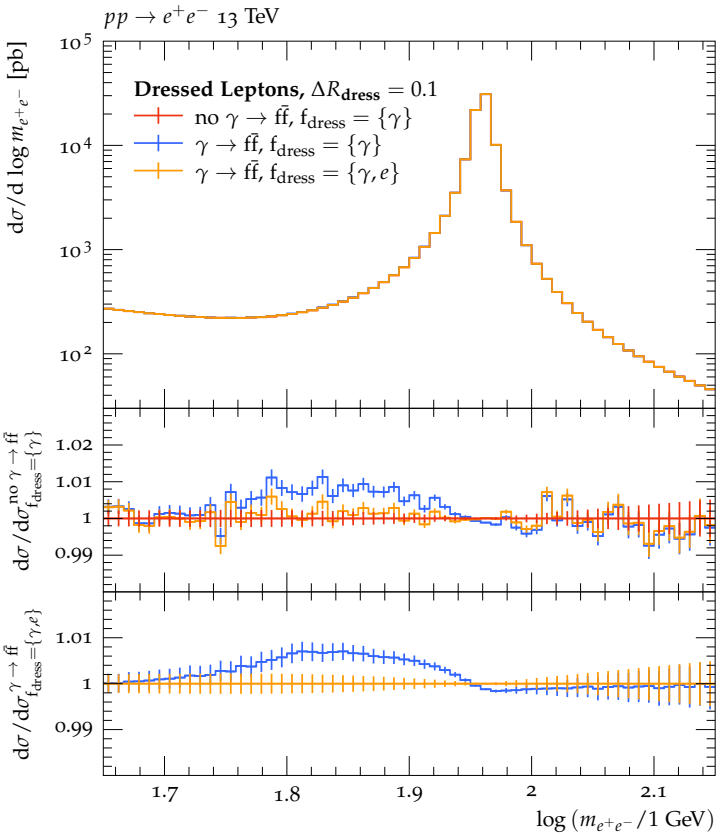

Figure 4.12: The dressed dilepton invariant mass $m_{e^+e^-}$ in Drell-Yan production as described by the YFS soft-photon resummation only (red) or additionally resolving the photons further into pairs of charged particles for a dressing cone size of $\Delta R_{\text{dress}} = 0.1$ in the mixed ordering scheme. We differentiate a dressing strategy recombining photons only (blue), and recombining photons and electrons (orange) within the dressing cone with the primary charged lepton. Two ratios are presented, either taking the soft-photon resummation without photon splittings (upper ratio), or the soft-photon resummation including photon splittings and dressing the primary leptons with photons as well as secondary electrons (lower ratio), as the reference.

4.4 Charged resonances

In this section we give the definitions for final-initial dipoles needed for the description of photon splittings in the QED corrections of charged particle decays, such as $W \to \ell\nu$.

The notation used to describe these dipoles is for the most part consistent with the final-final dipoles described above. We consider a charged resonance $\tilde{a}$ (a) decaying to a charged particle $\widetilde{ij}$ (i) and a recoiling system $\{\tilde{n}\}$ ($\{n\}$): $\tilde{a} \to \widetilde{ij}\,\{\tilde{n}\}$ before and $a \to i\,j\,\{n\}$ after the emission of a photon j, respectively. Ordinarily the recoil from the splitting would be absorbed locally by either the spectator a when i is the emitter, or vice versa. Since a is the decaying particle, however, we have chosen to keep its momentum unchanged and redistribute the recoil effectively to the particle(s) $\{n\}$. This allows us to use a single momentum map for both situations and to combine both emitter-spectator designations into a single dipole splitting function. This not only simplifies its description, but also removes problems with the positivity of the partial-fractioned CS splitting functions in situations where the mass correction is larger than the (quasi-)collinear emission term. Hence, we follow the treatment in refs. [65, 180] to construct the splitting functions and kinematic variables.

As described in sec. 4.2, the first step in the photon splitting algorithm is to determine the starting scale of each photon by reconstructing its emission history. In principle, emission of a photon can occur from the decaying particle $\tilde{a}$ or from its charged decay product $\widetilde{ij}$. However, since the former splitting is suppressed by the decaying particle's mass, it is much more likely to act as spectator. Therefore, as discussed above, we employ a single splitting function which contains the initial-state emission term in addition to the final-state emission. As a consequence, in the soft limit the full eikonal is recovered and the dipole radiates coherently, but splitting from the initial-state particle is never kinematically considered when building the required single-emitter history in the collinear interpretation of our parton shower.

After calculating the starting scale, the photons' evolution begins and photon split-

tings are considered. Since a photon is never considered to be emitted from the initial-state charged particle, and the decaying particle has a restricted phase space for absorbing recoil in any case, the spectator in all photon splittings is chosen to be the final-state particle i. For this reason, we do not need the kinematic mappings for a final-initial dipole. The splitting function and evolution variable definitions are detailed below.

Splitting functions. The dipole invariant mass Q^2 is defined as

$$Q^2 = (\tilde{p}_{\widetilde{ij}} - \tilde{p}_{\tilde{a}})^2 = (p_i + p_j - p_a)^2 \tag{4.4.1}$$

for the case of a dipole with final-state emitter i and initial-state spectator a.

For convenience, we define the quantity

$$\bar{Q}^2 = m_a^2 - m_i^2 - m_j^2 - Q^2. \tag{4.4.2}$$

The kinematic variables z and y are defined differently from the final-final case; they are given by

$$y = \frac{p_i p_j}{p_a p_i + p_a p_j - p_i p_j - 2m_i^2 - 2m_j^2}, \quad z = \frac{p_i p_a - p_i p_j - m_i^2}{p_i p_a + p_j p_a - 2p_i p_j - m_i^2 - m_j^2}. \tag{4.4.3}$$

In terms of these variables the splitting functions are given by

$$\begin{aligned} S_{f_{\widetilde{ij}}(\tilde{a})\to f_i\gamma_j(a)} \;=\; S_{\bar{f}_{\widetilde{ij}}(\tilde{a})\to \bar{f}_i\gamma_j(a)} \;=\; -\,\mathbf{Q}^2_{\widetilde{ij}\tilde{a}}\,\alpha\,\Bigg[&\frac{2}{1-z(1-y)}\left(1+\frac{2m_i^2}{\bar{Q}^2}\right) - (1+z) \\ &- \frac{m_i^2}{p_i p_j} - \frac{(p_i p_j)}{\bar{Q}^2}\,\frac{m_a^2}{\bar{Q}^2}\,\frac{4}{[1-z(1-y)]^2}\Bigg], \\ S_{s_{\widetilde{ij}}(\tilde{a})\to s_i\gamma_j(a)} \;=\; S_{\bar{s}_{\widetilde{ij}}(\tilde{a})\to \bar{s}_i\gamma_j(a)} \;=\; -\,\mathbf{Q}^2_{\widetilde{ij}\tilde{a}}\,\alpha\,\Bigg[&\frac{2}{1-z(1-y)}\left(1+\frac{2m_i^2}{\bar{Q}^2}\right) - 2 - \frac{m_i^2}{p_i p_j} \\ &- \frac{(p_i p_j)}{\bar{Q}^2}\,\frac{m_a^2}{\bar{Q}^2}\,\frac{4}{[1-z(1-y)]^2}\Bigg]. \end{aligned} \tag{4.4.4}$$

The additional factor $(1 + 2m_i^2/\bar{Q}^2)$ is needed to recover the soft eikonal limit by cancelling some of the mass dependence of the variables z and y. Note that $m_j = 0$

needs to be taken for the soft limit, so it is not present in this additional factor.

Evolution variable. As before, we consider two choices of evolution variable, virtuality and transverse momentum. The form of these variables in terms of the dipole invariant mass Q^2 and the masses of the particles in the process are very similar to those for final-final dipoles.

The virtuality is given by

$$\tilde{q}^2 = (m_a^2 - m_i^2 - m_j^2 - Q^2)\, y + m_i^2 + m_j^2 - m_{\widetilde{ij}}^2, \tag{4.4.5}$$

while the transverse momentum can be written

$$\mathrm{k}_\mathrm{T}^2 = (m_a^2 - m_i^2 - m_j^2 - Q^2)\, y\, z(1-z) - m_i^2\,(1-z)^2 - m_j^2\, z^2. \tag{4.4.6}$$

As before, the default scheme for the evolution variable is the mixed scheme, where the transverse momentum is computed as the starting scale for photon evolution but is interpreted as a virtuality thereafter. The pure transverse momentum and virtuality schemes are implemented as well.

Having discussed the details of our photon splitting algorithm for the case of W decays, we conclude this chapter.

4.5 Conclusions

In this chapter we detailed an extension to the soft-photon resummation in the Yennie-Frautschi-Suura framework, which incorporates higher QED corrections originating from photon splittings into charged-particle pairs. These photon-splitting corrections, which resolve the substructure of the newly produced photons, are larger than suggested by their fixed-order accuracy. In particular, they can be logarithmically enhanced with the ratio of the lightest charged particle, the electron, to the possible virtuality of the splitting photon.

Using the decay $Z \to e^+e^-$, we found that that the limit on the virtuality of the photon bremsstrahlung off a primary lepton is strongly correlated with the angular distance to this primary lepton, and thus also to the probability of that photon to split. We also investigated the systematics of our photon-splitting algorithm and found that algorithmic choices do not have a large impact on results. We found that the frequency of occurrence of different species agreed with theoretical expectations, showing a logarithmic dependence on the mass of the produced particles.

As a consequence of our extension, the MC prediction for the cloud of QED radiation surrounding the primary leptons of a hard decay contains an array of particle flavours, not solely photons. Hence, the standard dressing algorithms to define IR-safe dressed leptons were found to develop a strong sensitivity to further resolving the initial soft-photon cloud, in particular for larger dressing-cone radii. We therefore developed a novel set of flavour-aware strategies for dressing charged leptons and investigated their respective properties. We found that including secondary electrons as a minimal addition in the dressing procedure already substantially reduces this dependence on photon resolution, while an inclusion of all possible secondary flavours minimises it.

Using the example of the $Z \to e^+e^-$ decay rate, we investigated the dilepton invariant mass in detail. We found corrections of around 1% from photon splittings, with respect to the previous standard of not further resolving the initial photon radiation on the bare electrons. In the more relevant case of leptons cone-dressed with photons only, these could become much larger, namely up to 9% for large dressing cone radii of $\Delta\Theta_{\text{dress}} = 0.1$ or 0.2. Introducing a flavour-aware dressing algorithm restored the bare result to a large degree, however. The photon-splitting corrections were reduced to $1 - 2\%$, and their cone-size dependence was removed.

We then studied how the above effects translate to the general off-shell production of a Drell-Yan electron-positron pair at a hadron collider. We found very small corrections to bare leptons, as expected, while the corrections to photon-dressed leptons were up to 1% for a cone size of $\Delta R_{\text{dress}} = 0.1$. Including secondary electrons in the dressing removes these corrections. Unlike the academic case of on-shell Z

decay, it is not appropriate to include hadrons in lepton dressing in a hadron collider environment due to the abundance of their production from QCD processes. These findings reinforce the need for consistent treatment of higher-order QED corrections and lepton definitions in theory, event generators and experiment.

The photon splitting corrections were implemented in the SHERPA Monte-Carlo event generator and are incorporated in the SHERPA 3.0.0 release. All analyses and dressing strategies were implemented using RIVET's analysis tools [92, 93].

Chapter 5

Conclusions

In modern particle phenomenology, the precise prediction of SM processes is of great importance, both for background subtraction in the search for new physics, and for correct fitting of non-perturbative models to data. Since the inception of QCD 50 years ago, QCD calculations have undergone a huge reduction in uncertainty, allowing for accurate predictions of exclusive final states and differential distributions. The EW sector, despite being the source of many precision observables at hadron colliders, is often considered only to LO, due to the small size of α compared to α_s. In recent years, however, that has begun to change. In addition to the ever-increasing precision of experimental measurements at the LHC and its upcoming high-luminosity upgrade, there are other factors to motivate higher precision in the EW sector. First, the extraction of the W boson mass from legacy Tevatron data is in tension with previous measurements and with measurements of other EW parameters. Second, the anomalous magnetic moment of the muon has been measured to be in conflict with the current SM prediction. Finally, there are multiple proposals for future e^+e^- colliders, for which theoretical research and development must start imminently.

In this thesis, we presented three novel methods which increase the precision of QED radiative corrections in an automated, process-independent way.

We took inspiration from QCD in chapters 2 and 3, developing an NLO-matched

parton shower. This resums the leading logarithms associated both with the emission of a collinear or soft photon, and with the splitting of a photon into a collinear fermion pair. We demonstrated how the shower can be interleaved with a QCD parton shower, respecting the hadronisation scale of QCD while allowing pure QED radiation to continue to lower scales. We validated the shower, and its matched MC@NLO method, for the test case of a neutrino collider, then presented results for the phenomenologically relevant case of Higgs production via gluon fusion and its subsequent leptonic decay. We showed that the shower and MC@NLO are in excellent agreement with the YFS approach. We showed that a dipole identification helps to improve efficiency by eliminating negative QED shower weights in many processes.

We also discussed the implementation of a QED parton shower (and hence an MC@NLO implementation) for electron-positron colliders. Although this work is ongoing, we discussed properties of the LL electron structure function, numerical techniques to tackle its integrable singularity, and other considerations when implementing a parton shower for e^+e^- initial states.

In chapter 4, we took a different approach, building on the hugely successful YFS soft-photon resummation. We used the techniques developed in chapter 2 to extend the formalism to resum the leading logarithms from charged particle pair production. We found effects of a few percent on invariant mass distributions of resonance decay products, corresponding to around a 1% correction to the Drell-Yan process at the LHC. We studied the dependence of these observables on the flavour composition of the QED radiation surrounding final-state leptons, and found situations in which the usual method of cone dressing with photons introduces unphysical effects. One example is the strong cone size dependence of the higher-order corrections. We suggested alternative lepton dressing strategies to mitigate these effects, namely cone dressing using secondary electrons and positrons in addition to photons, and flavour-aware recombination dressing.

We implemented all methods described in this thesis in public MC code and analysis frameworks. The extension to the YFS formalism was released as part of SHERPA

3.0, while the QED parton shower and MC@NLO will be included in a future SHERPA 3 release. The lepton collider developments, once these are finalised and validated against predictions made using the YFS approach and other parton shower codes, will also be released as part of SHERPA. All analyses used to produce plots in this thesis were implemented in RIVET and can be obtained from the author on request, along with the SHERPA runcards. Public distribution of automated methods and new results is vital to the collaboration of the particle physics community and the continued progress in the development of our description of our universe.

Appendix A

Usage and settings

In this appendix we list the available keywords and settings which steer the calculation of the effects described in this thesis. All are correct at the time of publication, however, these are subject to change between versions of SHERPA, so the reader is encouraged to consult the appropriate version of the manual.

For the QED parton shower, under the scoped setting `SHOWER`, the following settings can be changed:

`EW_MODE` This setting turns on splitting functions for the QED parton shower.

- `0` no QED splittings (default),
- `1` all QED splittings,
- `2` photon emissions off fermions only.

`WED_FS_PT2MIN` The infrared cutoff in t, the parton shower ordering variable, for the QED final-state evolution. Default is $10^{-8}\,\mathrm{GeV}^2$.

`QED_IS_PT2MIN` The infrared cutoff in t, the parton shower ordering variable, for the QED initial-state evolution. Default is $2.5 \times 10^{-7}\,\mathrm{GeV}^2$.

`QED_SPECTATOR_SCHEME` This setting controls which charged particles may act as spectators for the emission of a photon off a fermion.

`One` only the nearest OSSF particle considered (default),

`All` all charged external legs in the event considered.

The nearest particle is selected by taking the minimum invariant mass. All charged particles are always considered as spectators for photon splittings and are given equal weight, unlike in the YFS module described above. For an s-channel process, this should generally be left at the default value. For a t-channel process it is recommended that the `All` setting is used.

`QED_ALLOW_FI` This setting controls whether to allow initial-final interference in the QED shower. Note that if switched on, `QED_SPECTATOR_SCHEME` must be set to `All`.

`false` no initial-final interference (default),

`true` initial-final and final-initial dipoles included.

`QED_ALLOW_II` This setting controls whether to allow initial-state particles to participate in the QED parton shower.

`false` no initial-state QED radiation,

`true` initial-initial dipoles included (default).

This setting is included to facilitate comparisons with the YFS final-state QED radiation, or for efficiency improvements for quark initial states.

To turn on the QED MC@NLO, the `NLO_Order` parameter in the `Process` section of the runcard must be set appropriately. In addition, the subtraction must be set as follows:

`NLO_SUBTRACTION_MODE` This setting controls which IR divergences are subtracted.

`QCD` only QCD subtraction (default),

`QED` only QED subtraction,

`QCD+QED` all SM IR divergences will be subtracted.

The MC@NLO is turned on in the usual way, using `NLO_MODE: MC@NLO` and the associated settings. All of the QED shower and MC@NLO settings will be available in a future release of SHERPA 3, however, the exact settings and default values are subject to change. Any changes will be detailed in the relevant user manual.

For the modifications to the YFS resummation, under the scoped setting `YFS`, the available settings are:

`PHOTON_SPLITTER_MODE` This setting governs which secondary flavours will be considered.

- `0` photons do not split,
- `1` photons split into electron-positron pairs,
- `2` muons,
- `4` tau leptons,
- `8` and/or light hadrons (up to `YFS_PHOTON_SPLITTER_MAX_HADMASS`).

The settings are additive; the default is `15`.

`PHOTON_SPLITTER_MAX_HADMASS` This setting sets the mass of the heaviest hadron which can be produced in photon splittings. Note that vector splitting functions are not currently implemented. Default is 0.5 GeV.

`PHOTON_SPLITTER_ORDERING_SCHEME` This setting defines the ordering scheme used.

- `0` transverse momentum ordering,
- `1` virtuality ordering,
- `2` mixed scheme (default).

`PHOTON_SPLITTER_SPECTATOR_SCHEME` This setting defines the allowed spectators for the photon splitting process.

`0` all primary emitters may act as spectator (default),

`1` only the photon's reconstructed emitter is eligible as a spectator.

`PHOTON_SPLITTER_STARTING_SCALE_SCHEME` This setting governs the determination of the starting scale.

`0` starting scale is chosed probabilistically (default),

`1` the starting scale is chosen using a winner-takes-all strategy.

These are available from the SHERPA 3.0 release onwards.

Bibliography

[1] L. Flower and M. Schoenherr, *Photon splitting corrections to soft-photon resummation*, *JHEP* **03** (2023) 238, [2210.07007].

[2] Muon g-2 collaboration, G. W. Bennett et al., *Final Report of the Muon E821 Anomalous Magnetic Moment Measurement at BNL*, *Phys. Rev. D* **73** (2006) 072003, [hep-ex/0602035].

[3] Muon g-2 collaboration, D. P. Aguillard et al., *Measurement of the Positive Muon Anomalous Magnetic Moment to 0.20 ppm*, *Phys. Rev. Lett.* **131** (2023) 161802, [2308.06230].

[4] T. Aoyama et al., *The anomalous magnetic moment of the muon in the Standard Model*, *Phys. Rept.* **887** (2020) 1–166, [2006.04822].

[5] K. G. Wilson, *Confinement of Quarks*, *Phys. Rev. D* **10** (1974) 2445–2459.

[6] D. J. Gross and F. Wilczek, *Ultraviolet Behavior of Nonabelian Gauge Theories*, *Phys. Rev. Lett.* **30** (1973) 1343–1346.

[7] H. D. Politzer, *Reliable Perturbative Results for Strong Interactions?*, *Phys. Rev. Lett.* **30** (1973) 1346–1349.

[8] Particle Data Group collaboration, M. Tanabashi et al., *Review of Particle Physics*, *Phys. Rev. D* **98** (2018) 030001.

[9] B. Andersson, G. Gustafson, G. Ingelman and T. Sjostrand, *Parton Fragmentation and String Dynamics*, *Phys. Rept.* **97** (1983) 31–145.

[10] J.-C. Winter, F. Krauss and G. Soff, *A Modified cluster hadronization model*, *Eur. Phys. J. C* **36** (2004) 381–395, [hep-ph/0311085].

[11] T. Kinoshita, *Mass singularities of Feynman amplitudes*, *J. Math. Phys.* **3** (1962) 650–677.

[12] T. D. Lee and M. Nauenberg, *Degenerate Systems and Mass Singularities*, *Phys. Rev.* **133** (1964) B1549–B1562.

[13] D. R. Yennie, S. C. Frautschi and H. Suura, *The infrared divergence phenomena and high-energy processes*, *Annals Phys.* **13** (1961) 379–452.

[14] S. Jadach and B. F. L. Ward, *Yfs2: The Second Order Monte Carlo for Fermion Pair Production at LEP / SLC With the Initial State Radiation of Two Hard and Multiple Soft Photons*, *Comput. Phys. Commun.* **56** (1990) 351–384.

[15] S. Jadach, B. F. L. Ward and Z. Was, *The Precision Monte Carlo event generator K K for two fermion final states in e+ e- collisions*, *Comput. Phys. Commun.* **130** (2000) 260–325, [hep-ph/9912214].

[16] K. Hamilton and P. Richardson, *Simulation of QED radiation in particle decays using the YFS formalism*, *JHEP* **07** (2006) 010, [hep-ph/0603034].

[17] M. Schönherr and F. Krauss, *Soft Photon Radiation in Particle Decays in SHERPA*, *JHEP* **12** (2008) 018, [0810.5071].

[18] F. Krauss, J. M. Lindert, R. Linten and M. Schönherr, *Accurate simulation of W, Z and Higgs boson decays in Sherpa*, *Eur. Phys. J. C* **79** (2019) 143, [1809.10650].

[19] S. Jadach, E. Richter-Was, B. F. L. Ward and Z. Was, *Monte Carlo program BHLUMI-2.01 for Bhabha scattering at low angles with Yennie-Frautschi-Suura exponentiation*, *Comput. Phys. Commun.* **70** (1992) 305–344.

[20] S. Jadach, W. Placzek and B. F. L. Ward, *BHWIDE 1.00: O(alpha) YFS exponentiated Monte Carlo for Bhabha scattering at wide angles for LEP-1 / SLC and LEP-2*, *Phys. Lett. B* **390** (1997) 298–308, [hep-ph/9608412].

[21] W. Placzek and S. Jadach, *Multiphoton radiation in leptonic W boson decays*, *Eur. Phys. J. C* **29** (2003) 325–339, [hep-ph/0302065].

[22] S. Jadach, W. Placzek, M. Skrzypek, B. F. L. Ward and Z. Was, *The Monte Carlo program KoralW version 1.51 and the concurrent Monte Carlo KoralW and YFSWW3 with all background graphs and first order corrections to W pair production*, *Comput. Phys. Commun.* **140** (2001) 475–512, [hep-ph/0104049].

[23] E. Barberio, B. van Eijk and Z. Was, *PHOTOS: A Universal Monte Carlo for QED radiative corrections in decays*, *Comput. Phys. Commun.* **66** (1991) 115–128.

[24] E. Barberio and Z. Was, *PHOTOS: A Universal Monte Carlo for QED radiative corrections. Version 2.0*, *Comput. Phys. Commun.* **79** (1994) 291–308.

[25] P. Golonka and Z. Was, *PHOTOS Monte Carlo: A Precision tool for QED corrections in Z and W decays*, *Eur. Phys. J. C* **45** (2006) 97–107, [hep-ph/0506026].

[26] N. Davidson, T. Przedzinski and Z. Was, *PHOTOS interface in C++: Technical and Physics Documentation*, *Comput. Phys. Commun.* **199** (2016) 86–101, [1011.0937].

[27] S. Höche, *Introduction to parton-shower event generators*, in *Theoretical Advanced Study Institute in Elementary Particle Physics: Journeys Through the Precision Frontier: Amplitudes for Colliders*, pp. 235–295, 2015, 1411.4085, DOI.

[28] T. Sjostrand, *Monte Carlo Tools*, in *65th Scottish Universities Summer School in Physics: LHC Physics*, pp. 309–339, 11, 2009, 0911.5286, DOI.

[29] J. M. Campbell et al., *Event Generators for High-Energy Physics Experiments*, in *Snowmass 2021*, 3, 2022, 2203.11110.

[30] G. T. Bodwin, *Factorization of the Drell-Yan Cross-Section in Perturbation Theory*, *Phys. Rev. D* **31** (1985) 2616.

[31] J. C. Collins, D. E. Soper and G. F. Sterman, *Factorization for Short Distance Hadron - Hadron Scattering*, *Nucl. Phys. B* **261** (1985) 104–142.

[32] T. Gleisberg, S. Höche, F. Krauss, M. Schönherr, S. Schumann, F. Siegert et al., *Event generation with SHERPA 1.1*, *JHEP* **02** (2009) 007, [0811.4622].

[33] V. N. Gribov and L. N. Lipatov, *Deep inelastic e p scattering in perturbation theory*, *Sov. J. Nucl. Phys.* **15** (1972) 438–450.

[34] L. N. Lipatov, *The parton model and perturbation theory*, *Yad. Fiz.* **20** (1974) 181–198.

[35] Y. L. Dokshitzer, *Calculation of the Structure Functions for Deep Inelastic Scattering and e+ e- Annihilation by Perturbation Theory in Quantum Chromodynamics.*, *Sov. Phys. JETP* **46** (1977) 641–653.

[36] G. Altarelli and G. Parisi, *Asymptotic Freedom in Parton Language*, *Nucl. Phys. B* **126** (1977) 298–318.

[37] S. Höche, F. Krauss, M. Schönherr and F. Siegert, *Automating the POWHEG method in Sherpa*, *JHEP* **04** (2011) 024, [1008.5399].

[38] S. Catani and M. H. Seymour, *A General algorithm for calculating jet cross-sections in NLO QCD*, *Nucl. Phys.* **B485** (1997) 291–419, [hep-ph/9605323].

[39] S. Catani, S. Dittmaier, M. H. Seymour and Z. Trocsanyi, *The Dipole formalism for next-to-leading order QCD calculations with massive partons*, *Nucl. Phys.* **B627** (2002) 189–265, [hep-ph/0201036].

[40] P. Nason, *A New method for combining NLO QCD with shower Monte Carlo algorithms*, *JHEP* **11** (2004) 040, [hep-ph/0409146].

[41] S. Frixione, P. Nason and C. Oleari, *Matching NLO QCD computations with Parton Shower simulations: the POWHEG method*, *JHEP* **11** (2007) 070, [0709.2092].

[42] S. Frixione and B. R. Webber, *Matching NLO QCD computations and parton shower simulations*, *JHEP* **06** (2002) 029, [hep-ph/0204244].

[43] S. Jadach, W. Płaczek, S. Sapeta, A. Siódmok and M. Skrzypek, *Matching NLO QCD with parton shower in Monte Carlo scheme — the KrkNLO method*, *JHEP* **10** (2015) 052, [1503.06849].

[44] S. Schumann and F. Krauss, *A Parton shower algorithm based on Catani-Seymour dipole factorisation*, *JHEP* **03** (2008) 038, [0709.1027].

[45] S. Höche, F. Krauss, M. Schönherr and F. Siegert, *A critical appraisal of NLO+PS matching methods*, *JHEP* **09** (2012) 049, [1111.1220].

[46] G. C. Fox and S. Wolfram, *A Model for Parton Showers in QCD*, *Nucl. Phys. B* **168** (1980) 285–295.

[47] R. Odorico, *Exclusive Calculations for QCD Jets in a Monte Carlo Approach*, *Nucl. Phys. B* **172** (1980) 157–200.

[48] K. Kajantie and E. Pietarinen, *Improved Evolution Equations for QCD*, *Phys. Lett. B* **93** (1980) 269–273.

[49] T. D. Gottschalk, *A Realistic Model for e+ e- Annihilation Including Parton Bremsstrahlung Effects*, *Nucl. Phys. B* **214** (1983) 201–222.

[50] G. Marchesini and B. R. Webber, *Simulation of QCD Jets Including Soft Gluon Interference*, *Nucl. Phys. B* **238** (1984) 1–29.

[51] B. R. Webber, *A QCD Model for Jet Fragmentation Including Soft Gluon Interference*, *Nucl. Phys. B* **238** (1984) 492–528.

[52] G. Marchesini, B. R. Webber, G. Abbiendi, I. G. Knowles, M. H. Seymour and L. Stanco, *HERWIG: A Monte Carlo event generator for simulating hadron emission reactions with interfering gluons. Version 5.1 - April 1991*, *Comput. Phys. Commun.* **67** (1992) 465–508.

[53] T. Sjostrand, *A Model for Initial State Parton Showers*, *Phys. Lett. B* **157** (1985) 321–325.

[54] T. Sjostrand, S. Mrenna and P. Z. Skands, *PYTHIA 6.4 Physics and Manual*, *JHEP* **05** (2006) 026, [hep-ph/0603175].

[55] S. Catani, F. Krauss, R. Kuhn and B. R. Webber, *QCD matrix elements + parton showers*, *JHEP* **11** (2001) 063, [hep-ph/0109231].

[56] L. Lonnblad, *Correcting the color dipole cascade model with fixed order matrix elements*, *JHEP* **05** (2002) 046, [hep-ph/0112284].

[57] T. Gleisberg, S. Hoeche, F. Krauss, A. Schalicke, S. Schumann and J.-C. Winter, *SHERPA 1. alpha: A Proof of concept version*, *JHEP* **02** (2004) 056, [hep-ph/0311263].

[58] M. R. Masouminia and P. Richardson, *Implementation of angularly ordered electroweak parton shower in Herwig 7*, *JHEP* **04** (2022) 112, [2108.10817].

[59] S. Höche, S. Schumann and F. Siegert, *Hard photon production and matrix-element parton-shower merging*, *Phys. Rev. D* **81** (2010) 034026, [0912.3501].

[60] G. Balossini, C. M. Carloni Calame, G. Montagna, O. Nicrosini and F. Piccinini, *Matching perturbative and parton shower corrections to Bhabha process at flavour factories*, *Nucl. Phys. B* **758** (2006) 227–253, [hep-ph/0607181].

[61] G. Balossini, C. Bignamini, C. M. C. Calame, G. Montagna, O. Nicrosini and F. Piccinini, *Photon pair production at flavour factories with per mille accuracy*, *Phys. Lett. B* **663** (2008) 209–213, [0801.3360].

[62] C. Carloni Calame, C. Lunardini, G. Montagna, O. Nicrosini and F. Piccinini, *Large angle Bhabha scattering and luminosity at flavor factories*, *Nucl. Phys. B* **584** (2000) 459–479, [hep-ph/0003268].

[63] C. M. Carloni Calame, *An Improved parton shower algorithm in QED*, *Phys. Lett. B* **520** (2001) 16–24, [hep-ph/0103117].

[64] C. M. Carloni Calame, G. Montagna, O. Nicrosini and F. Piccinini, *The BABAYAGA event generator*, *Nucl. Phys. B Proc. Suppl.* **131** (2004) 48–55, [hep-ph/0312014].

[65] S. Dittmaier, *A general approach to photon radiation off fermions*, *Nucl. Phys.* **B565** (2000) 69–122, [hep-ph/9904440].

[66] S. Dittmaier, A. Kabelschacht and T. Kasprzik, *Polarized QED splittings of massive fermions and dipole subtraction for non-collinear-safe observables*, *Nucl. Phys.* **B800** (2008) 146–189, [0802.1405].

[67] S. Kallweit, J. M. Lindert, S. Pozzorini and M. Schönherr, *NLO QCD+EW predictions for $2\ell 2\nu$ diboson signatures at the LHC*, *JHEP* **11** (2017) 120, [1705.00598].

[68] M. Schönherr, *An automated subtraction of NLO EW infrared divergences*, *Eur. Phys. J.* **C78** (2018) 119, [1712.07975].

[69] M. Schönherr, *Next-to-leading order electroweak corrections to off-shell WWW production at the LHC*, *JHEP* **07** (2018) 076, [1806.00307].

[70] S. Platzer and M. Sjodahl, *Subleading N_c improved Parton Showers*, *JHEP* **07** (2012) 042, [1201.0260].

[71] K. Hamilton, R. Medves, G. P. Salam, L. Scyboz and G. Soyez, *Colour and logarithmic accuracy in final-state parton showers*, *JHEP* **03** (2021) 041, [2011.10054].

[72] J. R. Forshaw, J. Holguin and S. Plätzer, *Rings and strings: a basis for understanding subleading colour and QCD coherence beyond the two-jet limit*, *JHEP* **05** (2022) 190, [2112.13124].

[73] L. Scyboz, *Subleading colour effects and spin correlations in the PanScales showers*, *PoS* **EPS-HEP2021** (2022) 416.

[74] M. Bengtsson and T. Sjostrand, *A Comparative Study of Coherent and Noncoherent Parton Shower Evolution*, *Nucl. Phys. B* **289** (1987) 810–846.

[75] M. H. Seymour, *Matrix element corrections to parton shower algorithms*, *Comput. Phys. Commun.* **90** (1995) 95–101, [hep-ph/9410414].

[76] S. Platzer and M. Sjodahl, *The Sudakov Veto Algorithm Reloaded*, *Eur. Phys. J. Plus* **127** (2012) 26, [1108.6180].

[77] L. Lönnblad, *Fooling Around with the Sudakov Veto Algorithm*, *Eur. Phys. J. C* **73** (2013) 2350, [1211.7204].

[78] A. Denner and S. Dittmaier, *Electroweak Radiative Corrections for Collider Physics*, *Phys. Rept.* **864** (2020) 1–163, [1912.06823].

[79] A. Freitas et al., *Theoretical uncertainties for electroweak and Higgs-boson precision measurements at FCC-ee*, 1906.05379.

[80] F. Krauss, R. Kuhn and G. Soff, *AMEGIC++ 1.0: A Matrix element generator in C++*, *JHEP* **02** (2002) 044, [hep-ph/0109036].

[81] S. Catani, Y. L. Dokshitzer, M. H. Seymour and B. R. Webber, *Longitudinally invariant K_t clustering algorithms for hadron hadron collisions*, *Nucl. Phys. B* **406** (1993) 187–224.

[82] S. D. Ellis and D. E. Soper, *Successive combination jet algorithm for hadron collisions*, *Phys. Rev. D* **48** (1993) 3160–3166, [hep-ph/9305266].

[83] A. Buckley, J. Ferrando, S. Lloyd, K. Nordström, B. Page, M. Rüfenacht et al., *LHAPDF6: parton density access in the LHC precision era*, *Eur. Phys. J.* **C75** (2015) 132, [1412.7420].

[84] T. Carli, T. Gehrmann and S. Hoeche, *Hadronic final states in deep-inelastic scattering with Sherpa*, *Eur. Phys. J. C* **67** (2010) 73–97, [0912.3715].

[85] S. Hoeche, F. Krauss and M. Schonherr, *Uncertainties in MEPS@NLO calculations of h+jets*, *Phys. Rev. D* **90** (2014) 014012, [1401.7971].

[86] F. Krauss, A. Price and M. Schönherr, *YFS Resummation for Future Lepton-Lepton Colliders in SHERPA*, *SciPost Phys.* **13** (2022) 026, [2203.10948].

[87] G. Montagna, O. Nicrosini, G. Passarino and F. Piccinini, *Semianalytical and Monte Carlo results for the production of four fermions in e+ e- collisions*, *Phys. Lett. B* **348** (1995) 178–184, [hep-ph/9411332].

[88] S. Frixione, *On factorisation schemes for the electron parton distribution functions in QED*, *JHEP* **07** (2021) 180, [2105.06688].

[89] V. Bertone, M. Cacciari, S. Frixione and G. Stagnitto, *The partonic structure of the electron at the next-to-leading logarithmic accuracy in QED*, *JHEP* **03** (2020) 135, [1911.12040].

[90] S. Frixione, *Initial conditions for electron and photon structure and fragmentation functions*, *JHEP* **11** (2019) 158, [1909.03886].

[91] J. Alwall, R. Frederix, S. Frixione, V. Hirschi, F. Maltoni, O. Mattelaer et al., *The automated computation of tree-level and next-to-leading order differential cross sections, and their matching to parton shower simulations*, *JHEP* **07** (2014) 079, [1405.0301].

[92] A. Buckley et al., *Rivet user manual*, *Comput. Phys. Commun.* **184** (2013) 2803–2819, [1003.0694].

[93] C. Bierlich et al., *Robust Independent Validation of Experiment and Theory: Rivet version 3*, *SciPost Phys.* **8** (2020) 026, [1912.05451].

[94] K. Danziger, S. Höche and F. Siegert, *Reducing negative weights in Monte Carlo event generation with Sherpa*, 2110.15211.

[95] Z. Nagy, *Next-to-leading order calculation of three jet observables in hadron hadron collision*, *Phys. Rev.* **D68** (2003) 094002, [hep-ph/0307268].

[96] T. Gleisberg and S. Höche, *Comix, a new matrix element generator*, *JHEP* **12** (2008) 039, [0808.3674].

[97] F. Buccioni, J.-N. Lang, J. M. Lindert, P. Maierhöfer, S. Pozzorini, H. Zhang et al., *OpenLoops 2*, *Eur. Phys. J. C* **79** (2019) 866, [1907.13071].

[98] A. Denner, S. Dittmaier and L. Hofer, *Collier: a fortran-based Complex One-Loop LIbrary in Extended Regularizations*, *Comput. Phys. Commun.* **212** (2017) 220–238, [1604.06792].

[99] G. Ossola, C. G. Papadopoulos and R. Pittau, *CutTools: A Program implementing the OPP reduction method to compute one-loop amplitudes*, *JHEP* **03** (2008) 042, [0711.3596].

[100] A. van Hameren, *OneLOop: For the evaluation of one-loop scalar functions*, *Comput. Phys. Commun.* **182** (2011) 2427–2438, [1007.4716].

[101] M. Chiesa, C. Oleari and E. Re, *NLO QCD+NLO EW corrections to diboson production matched to parton shower*, 2005.12146.

[102] E. Bothmann and D. Napoletano, *Automated evaluation of electroweak Sudakov logarithms in Sherpa*, 2006.14635.

[103] D. Pagani and M. Zaro, *One-loop electroweak Sudakov logarithms: a revisitation and automation*, *JHEP* **02** (2022) 161, [2110.03714].

[104] D. Pagani, T. Vitos and M. Zaro, *Improving NLO QCD event generators with high-energy EW corrections*, *Eur. Phys. J. C* **84** (2024) 514, [2309.00452].

[105] J. M. Lindert and L. Mai, *Logarithmic EW corrections at one-loop*, 2312.07927.

[106] CDF collaboration, T. Aaltonen et al., *High-precision measurement of the W boson mass with the CDF II detector*, *Science* **376** (2022) 170–176.

[107] Particle Data Group collaboration, R. L. Workman et al., *Review of Particle Physics*, *PTEP* **2022** (2022) 083C01.

[108] LHCb collaboration, R. Aaij et al., *Measurement of the W boson mass*, *JHEP* **01** (2022) 036, [2109.01113].

[109] ATLAS collaboration, M. Aaboud et al., *Measurement of the W-boson mass in pp collisions at $\sqrt{s} = 7$ TeV with the ATLAS detector*, *Eur. Phys. J. C* **78** (2018) 110, [1701.07240].

[110] CDF, D0 collaboration, T. A. Aaltonen et al., *Combination of CDF and D0 W-Boson Mass Measurements*, *Phys. Rev. D* **88** (2013) 052018, [1307.7627].

[111] CDF collaboration, T. A. Aaltonen et al., *Precise Measurement of the W -Boson Mass with the Collider Detector at Fermilab*, *Phys. Rev. D* **89** (2014) 072003, [1311.0894].

[112] D0 collaboration, V. M. Abazov et al., *Measurement of the W Boson Mass with the D0 Detector*, *Phys. Rev. Lett.* **108** (2012) 151804, [1203.0293].

[113] CDF collaboration, T. Aaltonen et al., *Precise measurement of the W-boson mass with the CDF II detector*, *Phys. Rev. Lett.* **108** (2012) 151803, [1203.0275].

[114] D0 collaboration, V. M. Abazov et al., *Measurement of the W boson mass*, *Phys. Rev. Lett.* **103** (2009) 141801, [0908.0766].

[115] CDF collaboration, T. Aaltonen et al., *First Run II Measurement of the W Boson Mass*, *Phys. Rev. D* **77** (2008) 112001, [0708.3642].

[116] CDF collaboration, T. Aaltonen et al., *First measurement of the W boson mass in Run II of the Tevatron*, *Phys. Rev. Lett.* **99** (2007) 151801, [0707.0085].

[117] CDF, D0 collaboration, V. M. Abazov et al., *Combination of CDF and D0 Results on W Boson Mass and Width*, *Phys. Rev. D* **70** (2004) 092008, [hep-ex/0311039].

[118] CDF collaboration, T. Affolder et al., *Measurement of the W boson mass with the Collider Detector at Fermilab*, *Phys. Rev. D* **64** (2001) 052001, [hep-ex/0007044].

[119] D0 collaboration, V. M. Abazov et al., *Improved W Boson Mass Measurement with the D0 Detector*, *Phys. Rev. D* **66** (2002) 012001, [hep-ex/0204014].

[120] D0 collaboration, B. Abbott et al., *A measurement of the W boson mass using electrons at large rapidities*, *Phys. Rev. Lett.* **84** (2000) 222–227, [hep-ex/9909030].

[121] D0 collaboration, B. Abbott et al., *A measurement of the W boson mass using large rapidity electrons*, *Phys. Rev. D* **62** (2000) 092006, [hep-ex/9908057].

[122] DELPHI collaboration, J. Abdallah et al., *Measurement of the Mass and Width of the W Boson in e^+e^- Collisions at $\sqrt{s}$ = 161-GeV - 209-GeV*, *Eur. Phys. J. C* **55** (2008) 1–38, [0803.2534].

[123] ALEPH collaboration, S. Schael et al., *Measurement of the W boson mass and width in e^+e^- collisions at LEP*, *Eur. Phys. J. C* **47** (2006) 309–335, [hep-ex/0605011].

[124] L3 collaboration, P. Achard et al., *Measurement of the mass and the width of the W boson at LEP*, *Eur. Phys. J. C* **45** (2006) 569–587, [hep-ex/0511049].

[125] OPAL collaboration, G. Abbiendi et al., *Measurement of the mass and width of the W boson*, *Eur. Phys. J. C* **45** (2006) 307–335, [hep-ex/0508060].

[126] ATLAS collaboration, G. Aad et al., *Measurement of the angular coefficients in Z-boson events using electron and muon pairs from data taken at $\sqrt{s} = 8$ TeV with the ATLAS detector*, *JHEP* **08** (2016) 159, [1606.00689].

[127] ATLAS collaboration, G. Aad et al., *Measurement of angular correlations in Drell-Yan lepton pairs to probe Z/gamma* boson transverse momentum at sqrt(s)=7 TeV with the ATLAS detector*, *Phys. Lett. B* **720** (2013) 32–51, [1211.6899].

[128] CMS collaboration, V. Khachatryan et al., *Angular coefficients of Z bosons produced in pp collisions at $\sqrt{s}$ = 8 TeV and decaying to $\mu^+\mu^-$ as a function of transverse momentum and rapidity*, *Phys. Lett. B* **750** (2015) 154–175, [1504.03512].

[129] LHCb collaboration, R. Aaij et al., *First Measurement of the $Z \to \mu^+\mu^-$ Angular Coefficients in the Forward Region of pp Collisions at $\sqrt{s} = 13$ GeV*, *Phys. Rev. Lett.* **129** (2022) 091801, [2203.01602].

[130] CDF collaboration, T. Aaltonen et al., *First Measurement of the Angular Coefficients of Drell-Yan e^+e^- pairs in the Z Mass Region from $p\bar{p}$ Collisions at $\sqrt{s}$ = 1.96 TeV*, *Phys. Rev. Lett.* **106** (2011) 241801, [1103.5699].

[131] CDF collaboration, T. Aaltonen et al., *Indirect Measurement of* $\sin^2\theta_W$ (M_W) *Using e^+e^- Pairs in the Z-Boson Region with $p\bar{p}$ Collisions at a Center-of-Momentum Energy of 1.96 TeV*, *Phys. Rev. D* **88** (2013) 072002, [1307.0770].

[132] ALEPH, DELPHI, L3, OPAL, SLD, LEP Electroweak Working Group, SLD Electroweak Group, SLD Heavy Flavour Group collaboration, S. Schael et al., *Precision electroweak measurements on the Z resonance*, *Phys. Rept.* **427** (2006) 257–454, [hep-ex/0509008].

[133] CDF collaboration, D. Acosta et al., *Measurement of the azimuthal angle distribution of leptons from W boson decays as a function of the W transverse momentum in $p\bar{p}$ collisions at $\sqrt{s} = 1.8$ TeV*, *Phys. Rev. D* **73** (2006) 052002, [hep-ex/0504020].

[134] ATLAS collaboration, G. Aad et al., *Measurement of the polarisation of W bosons produced with large transverse momentum in pp collisions at $\sqrt{s} = 7$ TeV with the ATLAS experiment*, *Eur. Phys. J. C* **72** (2012) 2001, [1203.2165].

[135] CMS collaboration, S. Chatrchyan et al., *Measurement of the Polarization of W Bosons with Large Transverse Momenta in W+Jets Events at the LHC*, *Phys. Rev. Lett.* **107** (2011) 021802, [1104.3829].

[136] D. Wackeroth and W. Hollik, *Electroweak radiative corrections to resonant charged gauge boson production*, *Phys. Rev. D* **55** (1997) 6788–6818, [hep-ph/9606398].

[137] U. Baur, S. Keller and W. K. Sakumoto, *QED radiative corrections to Z boson production and the forward backward asymmetry at hadron colliders*, *Phys. Rev. D* **57** (1998) 199–215, [hep-ph/9707301].

[138] U. Baur, S. Keller and D. Wackeroth, *Electroweak radiative corrections to W boson production in hadronic collisions*, *Phys. Rev. D* **59** (1999) 013002, [hep-ph/9807417].

[139] U. Baur, O. Brein, W. Hollik, C. Schappacher and D. Wackeroth, *Electroweak radiative corrections to neutral current Drell-Yan processes at hadron colliders*, *Phys. Rev. D* **65** (2002) 033007, [hep-ph/0108274].

[140] U. Baur and D. Wackeroth, *Electroweak radiative corrections to $p\bar{p} \to W^{\pm} \to \ell^{\pm}\nu$ beyond the pole approximation*, *Phys. Rev. D* **70** (2004) 073015, [hep-ph/0405191].

[141] A. Andonov, A. Arbuzov, D. Bardin, S. Bondarenko, P. Christova, L. Kalinovskaya et al., *SANCscope - v.1.00*, *Comput. Phys. Commun.* **174** (2006) 481–517, [hep-ph/0411186].

[142] S. Dittmaier and M. Krämer, *Electroweak radiative corrections to W boson production at hadron colliders*, *Phys. Rev. D* **65** (2002) 073007, [hep-ph/0109062].

[143] S. Dittmaier and M. Huber, *Radiative corrections to the neutral-current Drell-Yan process in the Standard Model and its minimal supersymmetric extension*, *JHEP* **01** (2010) 060, [0911.2329].

[144] Y. Li and F. Petriello, *Combining QCD and electroweak corrections to dilepton production in FEWZ*, *Phys. Rev. D* **86** (2012) 094034, [1208.5967].

[145] S. Alioli et al., *Precision studies of observables in $pp \to W \to l\nu_l$ and $pp \to \gamma, Z \to l^+l^-$ processes at the LHC*, *Eur. Phys. J.* **C77** (2017) 280, [1606.02330].

[146] R. Bonciani, L. Buonocore, M. Grazzini, S. Kallweit, N. Rana, F. Tramontano et al., *Mixed Strong-Electroweak Corrections to the Drell-Yan Process*, *Phys. Rev. Lett.* **128** (2022) 012002, [2106.11953].

[147] L. Buonocore, M. Grazzini, S. Kallweit, C. Savoini and F. Tramontano, *Mixed QCD-EW corrections to $\boldsymbol{pp \to \ell\nu_\ell + X}$ at the LHC*, *Phys. Rev. D* **103** (2021) 114012, [2102.12539].

[148] T. Armadillo, R. Bonciani, S. Devoto, N. Rana and A. Vicini, *Two-loop mixed QCD-EW corrections to neutral current Drell-Yan*, *JHEP* **05** (2022) 072, [2201.01754].

[149] M. Delto, M. Jaquier, K. Melnikov and R. Röntsch, *Mixed QCD$\otimes$QED corrections to on-shell Z boson production at the LHC*, *JHEP* **01** (2020) 043, [1909.08428].

[150] F. Buccioni, F. Caola, M. Delto, M. Jaquier, K. Melnikov and R. Röntsch, *Mixed QCD-electroweak corrections to on-shell Z production at the LHC*, *Phys. Lett. B* **811** (2020) 135969, [2005.10221].

[151] R. Bonciani, F. Buccioni, N. Rana and A. Vicini, *Next-to-Next-to-Leading Order Mixed QCD-Electroweak Corrections to on-Shell Z Production*, *Phys. Rev. Lett.* **125** (2020) 232004, [2007.06518].

[152] R. Bonciani, F. Buccioni, N. Rana and A. Vicini, *On-shell Z boson production at hadron colliders through $\mathcal{O}(\alpha\alpha_s)$*, *JHEP* **02** (2022) 095, [2111.12694].

[153] A. Behring, F. Buccioni, F. Caola, M. Delto, M. Jaquier, K. Melnikov et al., *Mixed QCD-electroweak corrections to W-boson production in hadron collisions*, *Phys. Rev. D* **103** (2021) 013008, [2009.10386].

[154] S. Dittmaier, A. Huss and C. Schwinn, *Mixed QCD-electroweak $\mathcal{O}(\alpha_s\alpha)$ corrections to Drell-Yan processes in the resonance region: pole approximation and non-factorizable corrections*, *Nucl. Phys. B* **885** (2014) 318–372, [1403.3216].

[155] S. Dittmaier, A. Huss and C. Schwinn, *Dominant mixed QCD-electroweak $O(\alpha_s\alpha)$ corrections to Drell–Yan processes in the resonance region*, *Nucl. Phys. B* **904** (2016) 216–252, [1511.08016].

[156] M. H. Seymour, *Photon radiation in final state parton showering*, *Z. Phys. C* **56** (1992) 161–170.

[157] J. Bellm et al., *Herwig 7.2 release note*, *Eur. Phys. J. C* **80** (2020) 452, [1912.06509].

[158] J. Bellm et al., *Herwig 7.0/Herwig++ 3.0 release note*, *Eur. Phys. J. C* **76** (2016) 196, [1512.01178].

[159] C. Bierlich et al., *A comprehensive guide to the physics and usage of PYTHIA 8.3*, 2203.11601.

[160] T. Sjöstrand, S. Ask, J. R. Christiansen, R. Corke, N. Desai, P. Ilten et al., *An introduction to PYTHIA 8.2*, *Comput. Phys. Commun.* **191** (2015) 159–177, [1410.3012].

[161] E. Bothmann et al., *Event Generation with SHERPA 2.2*, 2019.

[162] C. Carloni Calame, G. Montagna, O. Nicrosini and M. Treccani, *Higher order QED corrections to W boson mass determination at hadron colliders*, *Phys. Rev. D* **69** (2004) 037301, [hep-ph/0303102].

[163] C. M. Carloni Calame, G. Montagna, O. Nicrosini and M. Treccani, *Multiple photon corrections to the neutral-current Drell-Yan process*, *JHEP* **05** (2005) 019, [hep-ph/0502218].

[164] C. Carloni Calame, G. Montagna, O. Nicrosini and A. Vicini, *Precision electroweak calculation of the charged current Drell-Yan process*, *JHEP* **12** (2006) 016, [hep-ph/0609170].

[165] C. M. Carloni Calame, G. Montagna, O. Nicrosini and A. Vicini, *Precision electroweak calculation of the production of a high transverse-momentum lepton pair at hadron colliders*, *JHEP* **10** (2007) 109, [0710.1722].

[166] C. M. Carloni Calame, M. Chiesa, H. Martinez, G. Montagna, O. Nicrosini, F. Piccinini et al., *Precision Measurement of the W-Boson Mass: Theoretical Contributions and Uncertainties*, *Phys. Rev. D* **96** (2017) 093005, [1612.02841].

[167] C. Bernaciak and D. Wackeroth, *Combining NLO QCD and Electroweak Radiative Corrections to W boson Production at Hadron Colliders in the POWHEG Framework*, *Phys. Rev. D* **85** (2012) 093003, [1201.4804].

[168] L. Barze, G. Montagna, P. Nason, O. Nicrosini and F. Piccinini, *Implementation of electroweak corrections in the POWHEG BOX: single W production*, *JHEP* **04** (2012) 037, [1202.0465].

[169] A. Mück and L. Oymanns, *Resonace-improved parton-shower matching for the Drell-Yan process including electroweak corrections*, *JHEP* **05** (2017) 090, [1612.04292].

[170] L. Barze, G. Montagna, P. Nason, O. Nicrosini, F. Piccinini and A. Vicini, *Neutral current Drell-Yan with combined QCD and electroweak corrections in the POWHEG BOX*, *Eur. Phys. J. C* **73** (2013) 2474, [1302.4606].

[171] C. Gütschow and M. Schönherr, *Four lepton production and the accuracy of QED FSR*, *Eur. Phys. J. C* **81** (2021) 48, [2007.15360].

[172] A. V. Kotwal and B. Jayatilaka, *Comparison of HORACE and PHOTOS Algorithms for Multiphoton Emission in the Context of W Boson Mass Measurement*, *Adv. High Energy Phys.* **2016** (2016) 1615081, [1510.02458].

[173] C. M. Carloni Calame, S. Jadach, G. Montagna, O. Nicrosini and W. Placzek, *Comparisons of the Monte Carlo programs HORACE and WINHAC for single W boson production at hadron colliders*, *Acta Phys. Polon. B* **35** (2004) 1643–1674, [hep-ph/0402235].

[174] A. Arbuzov, R. Sadykov and Z. Was, *QED Bremsstrahlung in decays of electroweak bosons*, *Eur. Phys. J. C* **73** (2013) 2625, [1212.6783].

[175] S. Antropov, A. Arbuzov, R. Sadykov and Z. Was, *Extra lepton pair emission corrections to Drell-Yan processes in PHOTOS and SANC*, *Acta Phys. Polon. B* **48** (2017) 1469, [1706.05571].

[176] S. Höche, S. Kuttimalai, S. Schumann and F. Siegert, *Beyond Standard Model calculations with Sherpa*, *Eur. Phys. J. C* **75** (2015) 135, [1412.6478].

[177] S. J. Brodsky, G. P. Lepage and P. B. Mackenzie, *On the Elimination of Scale Ambiguities in Perturbative Quantum Chromodynamics*, *Phys. Rev. D* **28** (1983) 228.

[178] D. Amati, A. Bassetto, M. Ciafaloni, G. Marchesini and G. Veneziano, *A Treatment of Hard Processes Sensitive to the Infrared Structure of QCD*, *Nucl. Phys. B* **173** (1980) 429–455.

[179] M. Cacciari, G. P. Salam and G. Soyez, *The Anti-k(t) jet clustering algorithm*, *JHEP* **04** (2008) 063, [0802.1189].

[180] L. Basso, S. Dittmaier, A. Huss and L. Oggero, *Techniques for the treatment of IR divergences in decay processes at NLO and application to the top-quark decay*, *Eur. Phys. J.* **C76** (2016) 56, [1507.04676].